Karlsruher Institut für Technologie
Università degli Studi di Firenze

Nanophotonic circuits for single photon emitters

For obtaining the academic degree
of
DOCTOR OF ENGINEERING

Department of
Electrical Engineering and Information Technology
Karlsruhe Institute of Technology (KIT)
Karlsruhe, Germany

Approved

DISSERTATION
by

Anna P. Ovvyan

Date of Oral Examination:	14.12.2018
Supervisor:	Prof. Dr. rer. nat. Uli Lemmer
Co-supervisor:	Prof. Dr. Wolfram Pernice
Co-supervisor:	Prof. Dr. Francesco Cataliotti

Karlsruher Institut für Technologie
Università degli Studi di Firenze

Nanophotonic circuits for single photon emitters

Zur Erlangung des akademischen Grades eines

DOKTOR-INGENIEURS

von der KIT- Fakultät für
Elektrotechnik und Informationstechnik
des Karlsruher Instituts für Technologie (KIT)
Karlsruhe, Deutschland

genehmigte

DISSERTATION
von

Anna P. Ovvyan

Tag der mündlichen Prüfung:	14.12.2018
Referent:	Prof. Dr. rer. nat. Uli Lemmer
Korreferent:	Prof. Dr. Wolfram Pernice
Korreferent:	Prof. Dr. Francesco Cataliotti

Abstract

The work demonstrated in this thesis is dedicated to the engineering, simulation, fabrication and investigation of the essential element base to develop *hybrid* fully integrated nanophotonic circuit with coupled single photon emitter on chip. Combining several individually optimized stages of photonic devices, interconnected by nanoscale waveguides on chip with evanescently coupled single photon emitter, is a key step to the realization of such a scheme. The main requirements which should be satisfied for building such a *hybrid* system on-chip, and are thus the subject of this Thesis, are, namely: integration of single photon photostable source with high Quantum Yield (QY) on chip, efficient coupling of the emitted light to nanophotonic circuits, and efficient filtering of the excitation light.

Silicon nitride-on-insulator was used in all the projects described in this Thesis as the platform for the realization of photonic circuits. It provides low-loss broadband optical transparency covering the entire visible range up to the near infrared spectrum. Furthermore, sufficiently high refractive index contrast of Si_3N_4 on SiO_2 enables tight confinement of the mode in the waveguide structure and the realization of photonic circuits with small footprint.

A drastic increase of the coupling efficiency of the emitted light into the waveguide mode can be achieved by placing single-photon emitter on photonic crystal cavity because of its high Quality factor and small mode volume enabling a high Purcell enhancement.

To this end, a *novel cross-bar* 1D freestanding photonic crystal (PhC) cavity was developed for evanescent integration of single photon emitter, in particular Nanodiamonds (NDs), onto the region of the cavity. The novelty of this photonic structure is that collection of emitted light is provided via waveguide, which consists of PhC, whereas direct optical excitation is obtained through a crossed waveguide in the orthogonal direction of the in-plane cavity.

Optimization of the PhC cavity architecture was performed via rounds of simulations and verified by experimental measurements of fabricated devices on chip, which were found in excellent agreement.

The next round of simulations was performed to define an optimal position of the source in the cavity region to achieve maximum Purcell enhancement, which was realized via Local Density of States (LDOS) computation. Thus, placing a single photon emitter into a determined position on the cavity region of the developed cross-bar 1D freestanding PhC enables an increase in the transmission coupling efficiency into cavity up to $\beta = 71\%$ in comparison with computed 41% in the case of coupling into waveguide mode of cross-bar structure without PhC.

To block the pump light and at the same time transmit the fluorescent emitted light, compact and low-loss cascaded Mach–Zehnder interferometers (MZIs) tunable filters in the

visible region embedded within nanophotonic circuit, were realized. Tunability was provided via thermo-optic effect. The design of this device, namely geometry and shape of the microheater, was optimized via thermo-optic measurements, to achieve low electrical power consumption (switching power of 12.2 mW for the case of a spiral-shape microheater), high filtration depth and low optical insertion loss. The *novel* design with double microheaters on top of both arms of single and cascaded MZIs allows doubling the range of the shifting amplitude of the interference fringes. The demonstrated architecture of tunable filter is multifunctional, namely allowing transmission and filtering of the desired wavelengths in a wide wavelength range.
In particular, filtration depth beyond 36.5 dB of light with 532 nm wavelength and simultaneous transmission of light with 738 nm wavelength, which correspond respectively to excitation and emission wavelength of the silicon-vacancy color center in diamond, was demonstrated.

The results were published in *Ovvyan, A. P.; Gruhler, N.; Ferrari, S.; Pernice, W. H. P.* ***Cascaded Mach-Zehnder interferometer tunable filters****. Journal of Optics 2016, 18, 064011.*

Another filter with non-repetitive stopband with bandwidth of several nanometers was developed in this thesis. A non-uniform Bragg grating filter with *novel* double Gaussian apodization was proposed, whose fabrication required a single lithography step. This optimized Bragg filter provides a 21 dB filtration depth with a 3-dB bandwidth of 5.6 nm, insuring negligible insertion loss in the best case, while averaged insertion loss in reflected signal is 4.1dB (including loss in splitter).

One of the first *Hybrid* organic molecule Dibenzoterrylene (DBT) coupled on chip to a nanophotonic circuit was demonstrated in this thesis. DBT is a photostable single photon source in the near infrared spectrum at room and at cryogenic temperature, with almost unitary quantum yield. In order to protect the molecule against oxidization DBT was embedded in a host matrix – thin Anthracene crystal (DBT:Ac), which increases photostability.
Mirror enhanced grating couplers were employed as convenient output ports for ridge Si_3N_4 waveguide to detect single photons emitted from integrated Dibenzoterrylene (DBT) molecules at room temperature. The coupling ports were designed for waveguide structures on transparent silica substrates for light extraction from the chip backside. These grating ports were employed to read out optical signal from waveguides designed for single-mode operation at λ=785 nm.
DBT molecule was coupled evanescently to the waveguide, and upon excitation of isolated single molecule, emitted single photon signal was carried inside the waveguide to the outcoupling regions. Using a Hanbury Brown and Twiss setup pronounced antibunching dip was read out from a single molecule via the grating couplers, which confirms the quantum nature of the outcoupled fluorescent light. Simulated and measured transmission coupling efficiency of single photon emission into the waveguide mode equals $\beta = 42\%$.

The results were published in P. Lombardi*, A. P. Ovvyan*, S. Pazzagli, G. Mazzamuto, G. Kewes, O. Neitzke, N. Gruhler, O. Benson, W. H. P. Pernice, F. S. Cataliotti, and C. Toninelli. ***Photostable Molecules on Chip: Integrated Sources of Nonclassical Light***. ACS Photonics 2018, 5, 126−132, DOI: 10.1021/acsphotonics.7b00521.

* *P. Lombardi and A. P. Ovvyan contributed equally to this work.*

Engineered nanophotonic elements integrated in optical circuits with coupled single photon emitter on chip allow simultaneously to enhance the emitted light by coupling it into resonant PhC cavity modes, to spatially separate the excitation light from the enhanced single photon emission and to filter out pump light. Enhancement of the emission rate leads to a significant increase of the coupling efficiency into cavity. Beforehand performed simulations were an essential step in order to design, build and optimize the architecture of the nanophotonic devices. Local Density of States enhancement computation was especially necessary to precisely determine optimized position of the source on PhC cavity region to obtain maximum enhancement of the emission rate. To evaluate transmission coupling efficiency of emitted light into the cavity (β-factor), an extra round of simulations was performed.

The integrated photonic elements investigated and optimized in this Thesis, will be further employed for the realization of *hybrid* photonic circuits with integrated single photon sources: silicon-vacancy, nitrogen-vacancy centers in diamond as well as single organic molecule and semiconducting single-walled carbon nanotubes.

Zusammenfassung

Ziel dieser Arbeit war es grundlegende Elemente vollständig integrierter nanophotonischer Schaltkreise zu entwickeln, zu simulieren und herzustellen und Einzelphotonenquellen an diese zu koppeln. Ein solcher Aufbau wird ermöglicht durch individuell optimierte passive photonische Bauteile, verbunden durch Nanowellenleiter auf dem Chip und evaneszent gekoppelte Photonenquellen. Die Hauptanforderungen an diese Hybridsysteme aus passiver Photonik und aktiven Emittern sind die folgenden: effiziente Einkopplung des emittierten Lichts in den Wellenleiter, Herausfiltern des Pumplichts zur Anregung der Quelle und die Einbindung der photostabilen Einzelphotonenquelle auf dem Chip mit hoher Quantenausbeute.

Die verwendete Materialplattform in dieser Arbeit für die photonischen Schaltkreise war Siliziumnitrid, welche geringe Verluste und ein breites optisches Transmissionsspektrum vom sichtbaren Licht bis ins nahe Infrarot bietet. Der hohe Brechungsindexunterschied zwischen Siliziumnitrid und Siliziumdioxid ermöglicht zudem ein geringes Modenvolumen.

Durch Einbetten des Emitters in einen photonischen Kristall kann die Kopplungseffizienz auf Grund des hohen Qualitätsfaktors und dem kleinen Modenvolumen durch den Purcell-Effekt drastisch erhöht werden.

Daher wurden neuartige freistehende 1D photonische Kristallkavitäten (PhC Kavitäten) entwickelt, die eine Wellenleiterkreuzung beinhalten. Diese werden benutzt um Einzelphotonenquellen, wie insbesondere Nanodiamanten (NDs), evaneszent an die Kavität zu koppeln. Neu ist hierbei, dass das abgestrahlte Licht über den Wellenleiter, der die PhC Kavität enthält, eingesammelt wird, während der kreuzende Wellenleiter für die optische Anregung verwendet wird.
Die PhC Kavitäten wurden auf zwei Arten optimiert: durch mehrere Zyklen numerischer Simulationen der Geometire, sowie durch die experimentelle Evaluation der hergestellten Strukturen. Beide Vorgehensweisen zeigten eine gute Übereinstimmung, was sich in den Qualitätsfaktoren der Kavität zeigt.
Weitere Simulationen zielten darauf ab die optimale Position der Quelle innerhalb der Kavität zu finden, um eine größtmögliche Purcell-Verstärkung zu erreichen. Die wurde durch die Berechnung der lokalen Zustandsdichte (LDOS) realisiert. Durch die Platzierung eines Einzelphotonenemitters an der entsprechend optimierten Position konnte eine Verbesserung der Einkoppeleffizienz β erreicht werden. Diese beträgt $\beta = 71\%$ im Vergleich zu einer Effizienz von 41% für den Fall, dass keine PhC Kavität in der Kreuzungsstruktur verwendet wird.

Um das Anregungssignal zu blockieren und gleichzeitig das abgestrahlte Fluoreszenzsignal zu transmittieren, wurden integrierte, durchstimmbare Filter für den sichtbaren Spektralbereich entwickelt, die auf hintereinandergeschalteten Mach-Zehnder Interferometern (MZIs) basieren. Die Regelung der Filter beruht hierbei auf dem thermo-optischen Effekt. Die Konstruktion, d.h. die Geometrie und Form der Bauteile wurde mithilfe von thermo-optischen Messungen optimiert, um einen geringen Energieverbrauch (12.2 mW Schaltleistung im Falle von spiralförmigen Mikroheizern), eine große Filtertiefe sowie geringe optische Verluste zu erreichen. Das neuartige Design mit doppelten Mikroheizern auf beiden Armen der MZIs (sowohl bei einzelnen MZIs, als auch bei hintereinandergeschalteten MZIs) ermöglicht eine Verdopplung der Verschiebung der Interferenzstreifen. Die vorgeführte Bauteilarchitektur ist multifunktional, da sie sowohl die Blockierung als auch die Transmission von gewünschten Wellenlängen in einem großen Spektralbereich ermöglicht. Insbesondere wurde eine Filtertiefe von 36.5 dB bei einer Wellenlänge von 532 nm erreicht bei gleichzeitiger Transmission von Licht bei einer Wellenlänge von 738 nm. Diese zwei Wellenlängen entsprechen der Anregungs- und der Emissionswellenlänge von Silizium-Fehlstellen-Farbzentren in Diamant.

Die Ergebnisse wurden veröffentlicht in *Ovvyan, A. P.; Gruhler, N.; Ferrari, S.; Pernice, W. H. P.* ***Cascaded Mach-Zehnder interferometer tunable filters****. Journal of Optics 2016, 18, 064011.*

Ein weiterer Filter mit sich nicht wiederholendem Stopband und einigen Nanometern Bandbreite wurde ebenfalls innerhalb dieser Arbeit realisiert. Dazu wurde ein nicht gleichförmiges Bragg-Gitter mit neuartiger doppelt Gaußscher Apodisation entwickelt, das in einem einzelnen Lithographieschritt hergestellt werden kann. Der so optimierte Bragg-Filter ermöglicht ein Unterdrückungsverhältnis von 21 dB und eine 3-dB Bandbreite von 5.6 nm bei vernachlässigbarer Einfügedämpfung.

Eines der ersten hybriden Systeme zur Kopplung organischer Dibenzoterrylene (DBT) Moleküle an nanophotonische Schaltkreise wurde in dieser Arbeit präsentiert. DBT ist eine lichtbeständige Einzelphotonenquelle im nahinfraroten Spektralbereich sowohl bei Raumtemperatur als auch bei extrem tiefen Temperaturen mit einer nahezu unitären Quantenausbeute. Um das Molekül vor Oxidation zu schützen, wurde DBT in eine Gastmatrix eingebettet, die aus einem dünnen Anthracen-Kristall besteht und wodurch die Lichtbeständigkeit verbessert wurde.
Es wurden Gitterkoppler, die um einen Spiegel ergänzt wurden, als Schnittstelle am Ende der Si_3N_4 Wellenleiter verwendet. Damit wurden einzelne Photonen detektiert, die bei Raumtemperatur vom DBT Molekül in die geführten Moden des Wellenleiters gekoppelt wurden. Die Schnittstellen wurden für Wellenleiterstrukturen auf einem transparenten Glassubstrat entwickelt, um Licht durch die Rückseite des Chips auszukoppeln. Die Gitterkoppler wurden verwendet, um das optische Signal der Monomoden-Wellenleiter bei einer Wellenlänge von λ=785 nm auszulesen. Die DBT Moleküle wurden evaneszent an die

Wellenleiter gekoppelt, wodurch die einzelnen ausgesandten Photonen (bei optischer Anregung der Moleküle) zu den Gitterkopplern geführt wurden. Mithilfe eins Hanbury Brown und Twiss-Aufbaus wurde ein ausgeprägter Antibunching-Effekt gemessen, welches die Quantennatur des ausgekoppelten Fluoreszenzlichts bestätigt. Dies bestätigt die Quantennatur des abgestrahlten Fluoreszenzsignals. Sowohl die simulierte, als auch die gemessene Kopplungseffizienz der einzelnen Photonen in die Wellenleitermode betrug $\beta = 42\%$.

Die Resultate wurden veröffentlicht in P. Lombardi*, A. P. Ovvyan*, S. Pazzagli, G. Mazzamuto, G. Kewes, O. Neitzke, N. Gruhler, O. Benson, W. H. P. Pernice, F. S. Cataliotti, and C. Toninelli. ***Photostable Molecules on Chip: Integrated Sources of Nonclassical Light***. ACS Photonics 2018, 5, 126−132, DOI: 10.1021/acsphotonics.7b00521.

* *P. Lombardi und A. P. Ovvyan trugen in gleicher Weise zu dieser Arbeit bei.*

Die entwickelten nanophotonischen Bauteile integriert in optische Schaltkreise gekoppelt mit Einzelphotonenemittern auf dem Chip erlauben es gleichzeitig sowohl das emittierte Licht durch Kopplung in die resonante PhC Mode zu verstärken, um das Anregungslicht räumlich von der Einzelphotonenemission zu trennen, als auch das Pumplicht herauszufiltern. Die Verstärkung der Emissionsrate führt zu einem signifikanten Anstieg der Kopplungseffizient in die Kavität. Vorher durchgeführte numerische Simulationen waren ein essentieller Schritt für das Designen, Herstellen und Optimieren der Architektur der nanophotonischen Bauteile. Besonders wichtig für die exakte Positionierung der Quelle in der Kavität waren Berechnungen der lokalen Zustandsdichte, um eine maximale Verstärkung der Emissionsrate zu erreichen. Zur Auswertung der Transmissions-Kopplungs-Effizienz des emittierten Lichts in die Kavität (β - Faktor) wurde ein zusätzlicher Simulationslauf durchgeführt.

Die integrierten photonischen Elemente, die in dieser Arbeit untersucht und optimiert wurden, werden ferner zur Realisierung von hybriden photonischen Schaltkreisen mit integrierten Einzelphotonenquellen angewandt: SiV, NV-Zentren in Diamant sowie einzelne organische Moleküle und halbleitende einwandige Kohlenstoffnanoröhren.

Content

List of Abbreviations

1D	One dimensional
Au	Gold
Ac	Anthracene crystal
CW	Continuos wave
Cr	Chromium
DOS	Density of States
DBT	Dibenzoterrylene
DBT:Ac	Dibenzoterrylene molecule embedded in Anthracene crystal
EBL	Electron-beam lithography
ER	Extinction ratio
FSR	Free spectral range
FWHM	Full width maximum
HBT	Hanbury Brown and Twiss
HF	Hydrofluoric acid
HSQ	Hydrogen silesquioxane
IPA	Isopropanol
LDOS	Local Density of States
MIBK	Methyl-isobutyl keton
MZI	Mach-Zehnder Interferometer
ND	Nanodiamond
NV	Nitrogen-vacancy
PhC	Photonic crystal
PMMA	Polymethyl methacrylate
RIE	Reactive ion etching
SEM	Scanning electron microscope
SOI	Silicon-on-insulator
Si_3N_4	Silicon Nitride
SiO_2	Silicone dioxide
Si	Silicon
SiV	Silicon-vacancy
TE	Transverse electric
TM	Transverse magnetic
QY	Quantum Yuild
ZPL	Zero Phonon Line
WG	Waveguide

1. Introduction

1.1 Toward the integration of single photon emitter in nanophotonic circuit on chip

Fiber-optic communication system that transfers information over long distances such as trans-atlantic, is leading technology nowadays because of much higher bandwidth, which is provided by sending information on different wavelength (visible to IR range), whereas carrier signals are independent and do not interfere. Furthermore, very low optical loss (from 0.22 dB/km), almost no crosstalk, and protection against outside electromagnetic waves nowadays support effective speed of data transmission up to 11 Tbit/s or faster [2].

Analogous, the on-chip communication between photonic devices is provided by optical waveguides connection. Current state-of-art integrated photonic circuits on chip include variation of elements such as filters[3][4][5], modulators [6], detectors [7][8] which joined into complex systems by interconnecting via low-loss optical waveguides. Active single-photon emitter can be integrated into the photonic circuit via evanescent-field coupling in waveguide, or directly positioning inside groove/trench in the waveguide. Although, there is tremendous progress made in *hybrid integrated photonic circuits* [9][10][11][12][13][14], whereas the insuring scalability and reproducibility of positioning integrated single-photon emitters on chip still remains challenging. Bright, reliable, with high Quantum Yield and negligible dephasing single photon sources are required for development *hybrid integrated photonic circuits.* Here it is reviewed single photon-sources, where, in particular single molecules were employed in the experiments examined in this Thesis.

Single photon sources

NV-center

A nitrogen-vacancy (NV) color center is point defect in diamond formed by a substitutional nitrogen atom and a vacancy pair in the lattice position [15]. Ensemble of Negatively charged center (NV^-) was firstly observed in Gruber *et al* at room temperature [16]. It is distinguished negative charged NV^- (ZPL 637 nm) and neutral NV^0 (ZPL 575 nm) centers with corresponding vibronic bands (600-800 nm) at room temperature for excitation by 532 nm. Therefore, individual NV center are not time-limited, hence not indistinguishable at room temperature.
However, it should be noted that at low temperature ZPL structure for NV centers highly depends on electric, magnetic fields and strain [17].
Individual NV centers can be employed as photostable with no evidence of photobleaching [18] single photon emitters. By performing Hanbury-Brown-Twiss experiment antibunching dip with second-order correlation function below 0.5 at zero delay at room temperature was

demonstrated [18]. There are several disadvantages of NV-center: low probability of emitting photons into ZPL ≈ 3 % even at low temperature [19], large inhomogeneous broadening (several THz) typically seen in nanodiamonds, in contrast with bulk diamond, due to electric and strain fields [19], which influence on energy levels, and high lifetime (order of 10-20 ns), which limits pump and emission count rate.

SiV-center

SiV formed by silicon impurity (atom) placed between two adjacent vacancies in the diamond lattice, which ensures doublet structure of the ground and the excited states, however all four possible transitions result into sharp zero-phonon line (ZPL) at around 738 nm (1.68 eV) [20]. In contrast with NV-center SiV has suppressed phononic sideband obtaining time-limited line-width at cryogentic temperature with probability of emission into ZPL - 70% [21]. Furthermore, SiV are photostable without evidence of blinking with extremely low spectral diffusion (± 4 MHz) at cryogenic temperature [21]. Thus, SiV can be employed as single emitter producing indistinguishable photons, which was demonstrated in HOM experiment from separate SiV centers [22].

Low lifetime (order of 1-3 ns) allows obtaining higher emission rate. Pronounced antibunching dip lower than 0.12 was demonstrated [18].

Molecules

Single molecule can be utilized as single photon emitter, since it can emit only one photon at a time. In case of continuous-wave (CW) pumping single molecule, emitted photons will be separated by random distance determined by lifetime of excited state and excitation rate, whereas measured antibunching dip is a manifestation of single photon emission [23]. Under pulsed excitation, emitted photons will be deterministic, *i.e.* periodic in time. It was first demonstrated at cryogenic temperature [24], and at room temperature with high probability of emitting single photon (83%), determined by Lounis e*t al.* [23]. In the last case a non-resonant excitation was used, and this method has an advantage of spectral separation pump and emitted light.

Molecules experience dephasing at room temperature, due to phonon coupling, since they terminate on different vibrational levels of ground state. In contrast, at cryogenic temperature, dephasing is suppressed, since vibrational levels are vanished, resulting in lifetime-limited Zero Phonon Line (ZPL). In this case, single determined indistinguishable photons will be emitted by triggering photon emission.

Further advantages of single molecule are almost unitary Quantum Yield (QY) [25]; weak bottleneck (*i.e.* low intersystem crossing yield 10^{-7} [26]; low lifetime of excited state (several nanoseconds) that results in high emission rate at fluorescence wavelength, which is in the 700-800 nm wavelength range, where Si photodetectors have higher efficiency.

In order to prevent Photobleaching of molecule as a consequence of oxidization, molecules are usually embedded in host matrix, yielding in emitting around 10^{12} photons before bleaching [27]. Such shield has further advantages:

- it protects molecule against thermal overheating damage under laser pump light.
- Polarization of molecules embedded in one crystal is fixed, therefore probing the molecule within one crystal (host matrix) is easier due to fixed angle of collection.
- System *molecule:matrix* can be integrated in nanophotonic structure via evanescent coupling by means of spincoating the solution [10][27].

Carbon Nanotubes

Single-walled carbon nanotube (CNT) [28] is a good candidate as a single photon source to be integrated in the hybrid photonic circuit [11][12][29] due to its unique properties.
Optical properties of CNT depends on chilarity (the angle at which graphene is rolled up)[30], in particular bandgap of semiconducting CNTs (SCNT) [30]. SCNT can be optically and electrically driven with an optical response - emission Photoluminescence (PL) [31][32][33][34] or Electroluminescence (EL) [34] [35], respectively. Although the pump mechanism can be different, PL and EL emission is the result of recombination of electron and hole in CNT [35]. However Quantum Yield of PL is higher than EL, absorption cross-section in case of PL is much smaller (≈ 1%) [37], making PL and EL overall effectiveness compatible.
It should be noted, that Metallic CNTs (MCNT) do not have a bandgap and can be utilized as low-ohmic interconnects. Both MCNts and SCNTs can be utilized as broadband thermal emitters, *i.e.* incandescent light source, due heating of CNT as a results of current flow through CNT [12][39] [38]. For CNTs placed on the substrate this effect occurs at higher voltages in comparison with suspended CNTs due to possible heat diffusion/dissipation into substrate.
Antibunched EL or PL was mainly achieved at cryogenic temperatures, since potential dip to trap excitation, induced by natural defect, is very low (few meV) [40]. The first demonstration of single photon emission from SCNT coupled into in waveguide mode under electric excitation and simultaneous detection on chip was performed by S. Khasminskaya *et al*. [9].
Recently, by [41] it was demonstrated that oxygen doping SCNT allows to make deeper localization, this trapping of exciton results prevents quenching, *i.e.* non-radiative transition, and results in the single-photon emission at room-temperature from SCNT. Moreover, certain doping of SCNT allows to shift central emission wavelength and operate at telecommunication wavelength range. Another advantage of employing SCNT is its polarization, which strictly aligned along the tube, which allows to maximize transmission coupling efficiency into waveguide mode by placing CNT orthogonal (perpendicular) to the waveguide. In fact, controllable and scalable positioning of CNTs on the chip is provided by well-established method – Dielectrophoresis [42].

There are two main challenges to integrate single photon emitter in the nanophotonic circuit on chip:

- positioning of the emitter in the required place on the photonic structure, for instance in the cavity region.
  Whereas, in case of single molecules one of the working methods is spincoating the solution of molecules embedded in host matrix on chip, which in fact favorably stick to the edges of the waveguide [10].
- Efficient optical filtration of pump light, preferably on chip.
  In this thesis it was made a step forward in this way, namely integrated tunable cascaded MZI filter on chip, which transmits desired wavelength range (potential fluorescence light) and at the same time block another desired wavelength range (potential excitation light), and also Bragg grating filters on-chip, were engineered. It should be noted, that insertion loss of filter or filter stages should be suppressed. Notably, that, in particular SCNTs can be electrically driven, thus filtration is not required in this regime.

1.2 Goal and content of the Thesis

The goal of the work was to engineer, simulate, fabricate and investigate in the experiments the essential element base of integrated nanophotonic circuit on chip. Single photon emitter can be integrated in the region of photonic crystal cavity in order to enhance spontaneous emission rate due to Purcell effect [1]. Furthermore, cascaded tunable filter based on Mach-Zehnder Interferometer (MZI) was designed, and it can be potentially integrated in the nanophotonic scheme to filter out pump light as well as Bragg grating filter. Moreover, one of the first demonstrations of integration of the single molecule in nanophotonic device on chip at room temperature was shown in this Thesis.

In the **Second Chapter**, the fundamental passive elements such as photonic planar nanoscale waveguides to interconnect devices on the chip, grating couplers to couple light in and out from photonic circuit, Mach-Zehnder Interferometer (MZI) as a basic spectral filter, 1D nanobeam photonic crystal cavity were studied. Also Dibenzoterrylene (DBT) molecule as a good candidate of single photon emitter was investigated.

Third Chapter presents a designed *Single* and improved – *Cascaded Mach-Zehnder interferometer (MZI) as a tunable filter*, which was fabricated on silicon nitride-on-insulator platform on chip. It is based on thermo-optic effect, which was provided by placing microheaters on top of both arms of MZI. Based on performed thermo-optic measurements, the design of the device was optimized to achieve low electrical power consumption, high filtration depth and low insertion loss.

Forth Chapter shows another realization of integrated filter on chip by means of Bragg grating. The Non-uniform single- and double-apodized *Bragg filters* on silicon nitride-on-insulator were investigated; the parameters were verified and optimized via measurements. Double Gaussian apodized Bragg filter obtains up to 21 dB filtration depth, while consisting far fewer periods in comparison with single-apodized Bragg filter.

Fifth Chapter shows realization of the *novel* 1D freestanding *cross-bar Photonic Crystal (PhC) cavity* for integration of single photon emitter in the region of the cavity, whereas direct excitation of the source provided through crossed waveguide on chip.
Part of the work was the design of PhC cavity, namely optimization its parameters via simulations. In particular, PhC was studied through building Band-diagram (*Paragraph 5.1.1*), which was further employed as photonic crystal mirrors and placed from both sides of the cavity region. Optimization was verified by showing resonance mode distribution in the cavity (*Paragraph 5.1.2*).

The change of the main characteristics of the cavity (namely, Quality factor and resonance wavelength of the localized modes) with tuning geometrical cavity parameters was verified during and experimental investigation via transmission measurements of fabricated freestanding nanobeam and cross-bar PhC cavities. It was shown that the both results are in par (*Paragraph 5.1.3*).
Paragraph 5.2 presents full and experimental characterization of fabricated optimized freestanding cross-bar PhC cavity, which in its own term can be utilized for coupling single photon emitter in the region of the cavity. The performed simulation of Local Density of States *(Paragraph 5.2.2)* showed favorable position of the emitter to achieve highest enhancement of spontaneous emission coupled to certain resonance mode. Beta-factor simulations *(Paragraph 5.2.3)* demonstrated achievable coupling efficiency into resonance mode and further into waveguide mode.

Sixth Chapter presents one of the first demonstration of integration of single DBT:Ac molecule in Si_3N_4 ridge waveguide on fabricated chip via evanescent coupling at room temperature. Apodized mirror-enhanced grating couplers were employed as output ports to read out single photon signal by performing Hanbury Brown and Twiss (HBT) experiment, where measured pronounced antibunching dip proved the quantum nature of outcoupled fluorescence light.
Coupling of single molecule into waveguide mode was determined via simulations and verified in experiment, resulting in 42% efficiency.

Seventh Chapter concludes the main achieved results demonstrated in this Thesis and gives outlook on the future scientific work.

Supplementary Information is dedicated to optimization of fabrication process of 1D freestanding PhC cavity.

2. Essential element base of integrated photonic circuit

2.1 On-chip integrated photonic passive elements

In this chapter it is considered working principle of main components of integrated photonic circuit, which were utilized in this thesis. In particular, Apodized grating couplers (Paragraph 2.1.2) were employed to read out single photon signal and analyzed in the Chapter 6. Mach-Zehnder interferometer (Paragraph 2.1.3) serves as a basis to built tunable MZI filters, explored in the Chapter 3. Photonic crystal cavity (PhC) theory (Paragraph 2.1.4) provides the background for engineering *novel cross-bar* PhC cavity investigated in the Chapter 5.

2.1.1 Single-mode planar optical waveguide

Planar optical waveguide is the key element of integrated photonic circuit; it confines and guides the light within photonic circuit, and ensures interconnection between photonic devices on the chip. Planar waveguide consists of thin film, which is the core with high refractive index, covered with thicker films called cladding, which has lower refractive index, thus enabling to confine light in its one longitudinal direction. In the work it was utilized half- , ¾-etched rib and ridge waveguides displayed in Fig 2.1 a), b), where thin layer Si_3N_4 (refractive index $n = 2$ for wavelength range $\lambda = 700 - 800$ nm) was a core and SiO_2 layer ($n = 1.45$ for wavelength range $\lambda = 700 - 800$ nm) was the bottom cladding layer, whereas top layer was either air or SiO_2 depends on the applicability of photonic device.

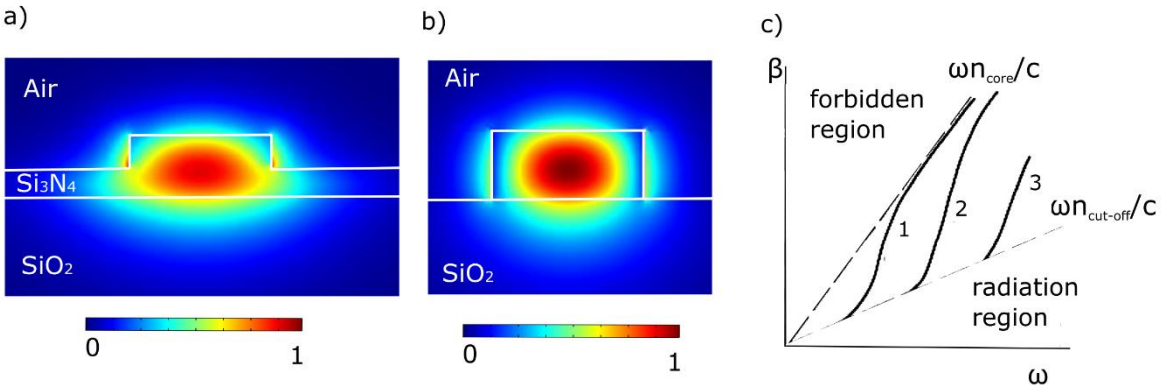

Figure 2.1. Simulated electric field profile of fundamental TE0 mode on $\lambda = 738$ nm in single mode **(a)** half-etched rib waveguide (width 450 nm, height of rib 100 nm) and **(b)** fully-etched ridge waveguide (width 450 nm, height 200 nm). **c)** $\beta - \omega$ dispersion diagram for dielectric planar waveguide.

Since the refractive index abruptly changes on the interface core-cladding such planar waveguides referred as *step-index* waveguide.

In the first approximation, guiding of the light in the multi-mode waveguide can be explained by the ray-optics, namely by total internal reflection, however full and precise characterization is given by Maxwell's equations [32] where the light propagates as electromagnetic wave. Guided modes in planar waveguide are solutions of Maxwell's equations expressed as moving planewaves [32]:

$$E_m = E_{0m}(y,z)e^{(i\omega t-\beta_m x)} \qquad (1)$$

$$H_m = H_{0m}(y,z)e^{(i\omega t-\beta_m x)} \qquad (2)$$

where $E_{0m}(y,z)$ and $H_{0m}(y,z)$ – profile of electric and magnetic fields, $\beta_m = \frac{2\pi}{\lambda}n_{eff,m}$ – propagation constant, m – index of the mode. Modes are trapped in the core of the waveguide, *i.e.* in finite volume; therefore number of modes is discrete.

The guided modes in planar waveguides can be classified as Transverse Electric TE-mode where the only non-vanishing fields are $E_y \neq 0,\ H_x \neq 0, H_z \neq 0$, or Transverse Magnetic TM-mode where $H_y \neq 0,\ E_x \neq 0,\ E_z \neq 0$, so it is clear that there is only one non-vanishing component in longitudinal direction in case of each mode in planar waveguide (H_x for TE-mode and E_x for TM mode). Transverse Electric Magnetic mode (TEM) ($H_x = 0\ and\ E_x = 0$) and Hybrid modes ($E_y \neq 0$ and $H_y \neq 0$) do not exist in planar waveguide [32].

Typical $\beta - \omega$ *dispersion diagram* shown in Fig. 2.1 c) for three discrete guided modes, where *radiation continuous modes* characterized by the case when most of the light of the mode propagates in the cladding, *i.e.* not guided modes. Thus, propagation constant and effective refractive index of the guided modes should satisfy the following inequalities:

$$\frac{\omega}{c}n_{cut-off} < \beta_m < \frac{\omega}{c}n_{core} \qquad (3)$$

$$n_{cut-off} < n_{eff\_mode} < n_{core} \qquad (4)$$

In the scope of the thesis it was employed only TE-like guided mode, furthermore the goal was to determine geometry of planar waveguide to ensure single mode propagation on target wavelength. Since the height of the waveguide was fixed by utilizing conventional silicon nitride-on-insulator wafers the one parameter which can be tuned is the width of the waveguide. Thereby, it was performed numerical finite element simulations (FEM) using COMSOL software [44] to determine dependence of effective refractive index of the first two modes on the width of waveguide, in particular it was performed simulations for half-etched rib waveguide which was employed to build Cascaded Mach-Zehnder tunable filter investigated in the Chapter 3. Results of the simulations are shown in Fig. 2.2.

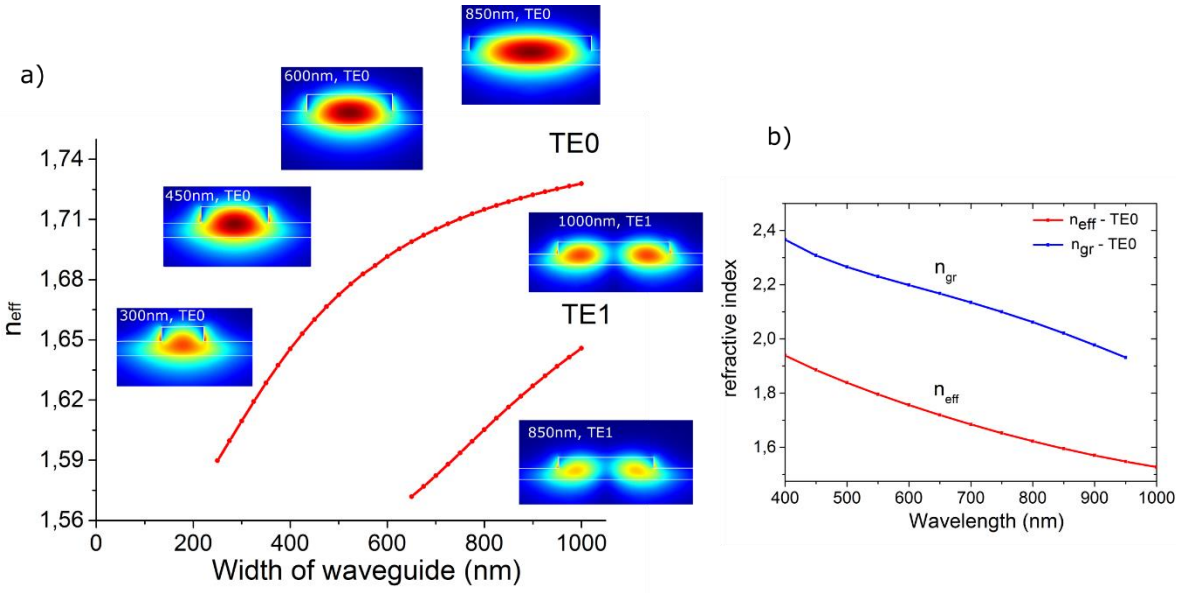

Figure 2.2. a) Simulated effective refractive index of the first two transverse modes (TE0 and TE1) guided in half-etched rib waveguide on $\lambda = 738$ nm as a function of width of the rib. Insets show cross-section of waveguide superimposed with electric field mode profile for different width. **b)** Simulated effective refractive index and group refractive index as a function of wavelength for TE0 guided mode for the same geometry waveguide: width=450 nm, height of rib 100 nm.

Cutoff mode index $n_{eff} = 1.5477$ characterizes effective refractive index of the mode below which the light cannot propagate in the waveguide. Second mode TE1 shows up when waveguide is wider 640 nm, therefore to ensure single mode propagation at $\lambda = 738$ nm in the waveguide width of rib was set 450 nm.

Effective refractive index defines phase speed of the mode, in other words growth of propagation constant β_m for this mode, whereas group refractive index determines the velocity of the envelope of the mode (group velocity), *i.e.* speed of transferring energy which differs from phase velocity due to waveguide dispersion. Group index is determined as

$$n_{gr}(\lambda) = n_{eff}(\lambda) - \lambda \frac{dn_{eff}(\lambda)}{d\lambda} \qquad (5) \ .$$

Simulated $n_{eff}(\lambda)$ and $n_{gr}(\lambda)$ are shown in Fig. 2.2 b).

2.1.2 Apodized Grating Coupler

Photonic elements can be integrated all on one chip by interconnection them with optical waveguides, where the mode is highly confined due to the refractive index contrast between core and cladding. To couple light in and out it to the photonic circuit it is needed to convert incident Gaussian-like free space mode or mode from optical fiber (diameter of the core of single mode

fiber on 1550 nm is 9 μm) into the waveguide mode (waveguide cross section ≈ 450 nm ×200 nm) and back in case of detection outcoupled light. Grating coupler is a good candidate to ensure it via reliable out-of-plane coupling, which requires just slight and repetitive alignment. Grating coupler (Fig. 2.3) is periodic structure, it ensures coupling out-of plane due to diffraction from every teeth of the coupler based on Bragg condition [45]:

$$sin(\theta_{in}) = \frac{n_{eff} - m\lambda/\Lambda}{n_{clad}}, \qquad (6)$$

where n_{eff} – effective refractive index of the mode in the grating, n_{clad} – refractive index of top cladding of the grating, m – diffraction number, Λ – period of the grating, λ – wavelength of the input light. *Fiber-array* measurement setup explained in Chapter 3 (Paragraph 3.3) was used to optically characterize photonic devices on chip by employing grating couplers, namely light was coupled from optical fiber fixed above the chip which was aligned under an angle 8° to the chip, so $\theta_{in} = 11.67°$ (in air) to the coupler, propagates through the photonic device and coupled out from the second grating coupler.

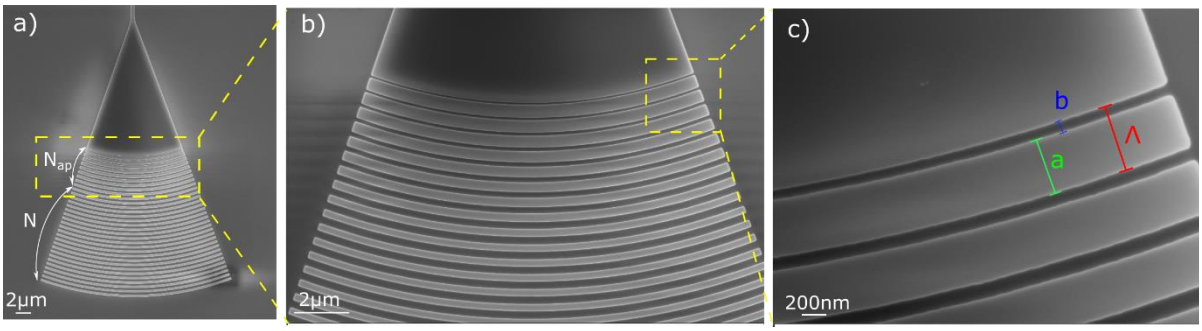

Figure 2.3. a) SEM image of apodized grating coupler with period Λ with zoom-in in **b)** and **c)**.

To improve coupling efficiency it was utilized apodization recipe of filling factor and optimized tapering length of grating coupler to match the output diffracted mode with a Gaussian-like free-space or fiber-coupled mode [48][46][47][48], where fill factor is defined as the ratio of a to the grating period $ff = a/\Lambda$. Apodization was provided by placing additional $N_a = 10$ grating periods with linear increase of ff up to 89-91% (depends on the period) closer to the taper region after $N = 22$ grating periods with constant $ff = 50\%$. It should be noted, that highest value of apodized ff_{ap} is limited by fabrication resolution of the groove, *i.e.* resolution of employed photoresist for electron-beam lithography, which is in the considered case is ≈ 50nm. Period is the main parameter to tune diffracted central wavelength. Measured transmission spectrum of basic photonic device consists of waveguide terminated by two apodized grating couplers shown in Fig. 2.4 a).

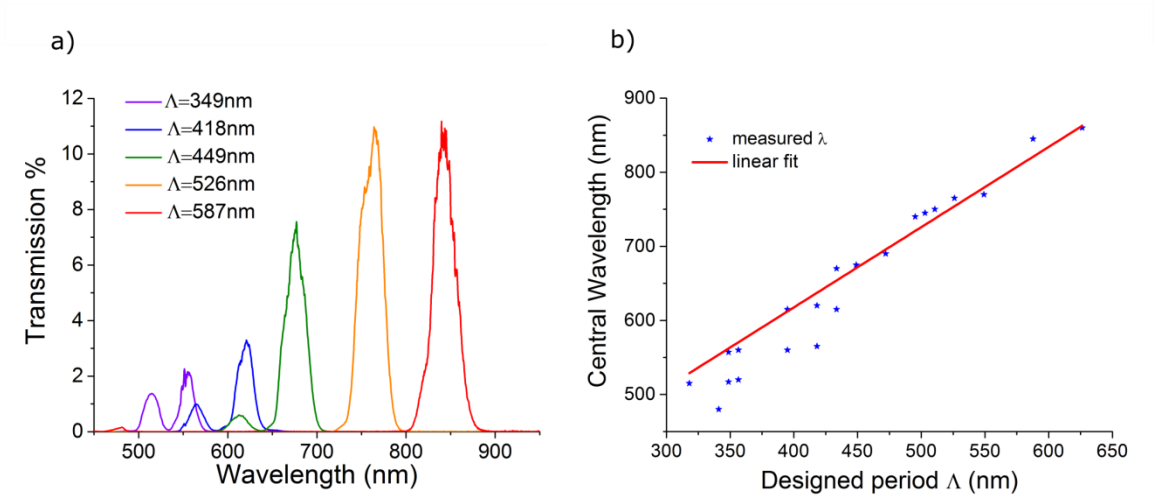

Figure 2.4. a) Measured Normalized Transmission spectrum of fabricated half-etched waveguide terminated by two grating couplers with variation of periods Λ. **b)** Measured central wavelength as a function of designed period Λ of coupler.

Grating coupler acts as spectral and polarizing filter, in the scope of the thesis it was employed apodized grating couplers, with typical bandwidth couple of tens nanometers, which act as TE-like polarizing filter.

To sum up, employing grating couplers is alignment-free approach to couple light in and out of the photonic circuit, which is ensured by converting incident Gaussian-like free space mode into guided mode. Transmission window (several tens of nanometers) of the coupler can be tuned by changing the period; typical coupling efficiency of one grating coupler is 26-31% with peak obtained value 34.3% in the wavelength range 600-900 nm. Last but not the least, grating couplers fabricated in the same electron-beam lithography step with other photonic devices on the chip, they ensure compact footprint and easy access to any circuit on the chip.

2.1.3 Mach-Zehnder Interferometer

In Mach-Zehnder interferometer on chip (Fig 2.5 a)) input light is equally splits by Y-splitter in two beams which carried in two waveguides-arms with certain length difference then recombined on the Y-combiner resulting in interference pattern shown in Fig 2.5 b). Pass difference Δl between arms introduces corresponding phase difference $\Delta\varphi(\lambda) = \frac{2\pi}{\lambda} * \Delta l * n_{eff}$, where n_{eff} is the effective refractive index of the waveguide mode, resulting in modulated intensity at the output port as

$$I_{1MZI}(\lambda) = \frac{1}{4} * I_0 * \left(e^{-i(\varphi_1+\Delta\varphi)} * e^{-\frac{\alpha}{2}(l+\Delta l)} + e^{-i\varphi_1} * e^{-\frac{\alpha}{2}l}\right) * \left(e^{i(\varphi_1+\Delta\varphi)} * e^{-\frac{\alpha}{2}(l+\Delta l)} + e^{i\varphi_1} * e^{-\frac{\alpha}{2}l}\right) = \frac{1}{4} * I_0 * \left(2 * cos(\Delta\varphi) * e^{-\alpha\left(l+\frac{\Delta l}{2}\right)} + e^{-\alpha l} + e^{-\alpha(l+\Delta l)}\right), \quad (7)$$

where φ_1 – phase of the mode in the shortest arm, Δl – length difference between arms, $e^{-\frac{\alpha}{2}(l+\Delta l)}$, $e^{-\frac{\alpha}{2}l}$ – account for propagation loss in long and short arms, respectively.

For simplicity in case of negligible loss, intensity at the output port can be found as

$$I_{1MZI}(\lambda) = \frac{1}{2} * \left(1 + cos\left(\Delta\varphi(\lambda)\right)\right). \quad (8)$$

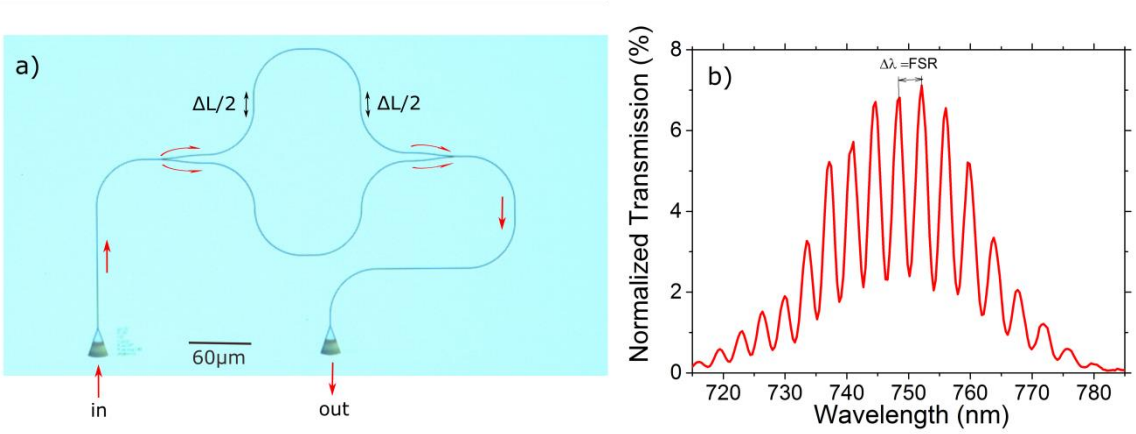

Figure 2.5. Mach-Zehnder interferometer on-chip. **a)** Optical micrograph of fabricated MZI on Si_3N_4 chip with pass difference ΔL. **b)** Normalized Transmission spectrum of MZI measured with supercontinuum white light source, where outcoupled light detected with spectrometer. Extinction ratio at $\lambda = 750\,nm$ equals $ER \approx 10 * (\log(0.07/0.02)) = 5.4\,dB$. It is low mostly due to not ideal 50/50 splitting ratio as a result of non-optimized splitter and combiner parameters, and because of low temporal coherence of supercontinuum light, *i.e.* short coherence length.

Outcoupled interference pattern depends on pass difference and Y-splitter ratio. The spacing between two close maximums, *i.e.* Free Spectral Range (FSR) determines as

$$\Delta\lambda = \frac{\lambda^2}{n_{gr} * \Delta l}, \qquad (9)$$

where n_{gr} – group refractive index of the waveguide mode.

Contrast of interference fringes, referred as extinction ratio strongly depends on optical loss in the arms and splitting ratio of Y-splitter (ideally 50/50), it can be determined from (7) as

$$ER = \frac{I_{max}}{I_{min}} = \left(\frac{1 + e^{-\frac{\alpha}{2}\Delta l}}{1 - e^{-\frac{\alpha}{2}\Delta l}}\right)^2 . \qquad (10)$$

Mach-Zehnder interferometers widely used as an on chip ultra-fast modulators [48] and bio-sensors [50]. In the scope of the thesis Mach-Zehnder interferometer was employed as a basic element to build integrated thermo-optic tunable filter on Si_3N_4 chip, where extra thermally induced phase difference resulted in the shift of interference fringes in the frequency space, while to enhance filtration depth it was implemented cascaded circuit of MZIs on chip, investigated in the Chapter 3.

2.1.4 Photonic Crystal Cavity

Band diagram

Lord Rayleigh in 1887 determined that periodic dielectric structure characterized by periodic dielectric permittivity introduces a bandgap [51][52], *i.e.* continuous range of frequencies within which there are no propagating solutions of Maxwell's equations for any wavevector. These modes exponentially decayed inside periodic structure along the way of propagation, the reason of it that light is partially reflected at each interface of dielectric layers, so these waves are destructively interfere along propagation way. Thus, such structure behaves as a *Bragg mirror*. Light in the wavelength range out of bandgap propagates through the crystal without scattering, since wavevector is conserved, as will be shown later in this chapter.

Bloch-Floquet theorem states that for periodic structure the solutions of Hermitian eigenproblem equation are Bloch states [52]. Bloch modes propagate through the crystal without defects without scattering, since wavevector is conserved quantity. Bloch state corresponds to planewave $e^{i(\vec{k}\vec{x}-\omega t)}$ with periodic envelope $\vec{u}(\vec{x})$, thus electric field is given by:

$$\vec{E}(\vec{x}) = \vec{u}(\vec{x}) * e^{i(\vec{k}\vec{x}-\omega t)}, \qquad (11)$$

where $\vec{u}(\vec{x})$ is periodic function of position $\vec{u}(\vec{x}+a) = \vec{u}(\vec{x})$, a - lattice constant, $\vec{k}$ - Bloch wavevector.

Since $\vec{u}(\vec{x})$ is periodic function, consideration the eigenproblem over an infinite domain is

equivalent to consideration the eigenproblem over a finite domain with length a, therefore eigenvalues (eigenfrequencies) $\omega_m(\vec{k})$ form discrete "*bands*" (for $m = 1,2,3$ ...), which are indicated on Band diagram.

In this thesis it is considered 1D PhC cavity, thus there is only one wavevector component along the direction of periodicity – $\vec{k}_x$. Eigenvalue solutions $\omega_m(\vec{k}_x)$ of Hermitiam eigenproblem are periodic functions of $\vec{k}_x$, hence it is sufficient to find a solution of eigneproblem for $\vec{k}_x$ in the finite region $\vec{k}_x = -\frac{\pi}{a} \dots \frac{\pi}{a}$ – *first Brillouin zone.* Taking into account time-reversal symmetry it is reasonable to find solutions in only *irreducible Brillouin zone* $\vec{k}_x = 0 \dots \frac{\pi}{a}$. Simulated Band diagram of one primitive cell of freestanding 1D PhC is shown in Fig. 2.6. Light line is given by $\omega = ck$. Frequency region $\omega < ck$ presents a band gap, where there are no allowed modes, and localized bands which are guided, while the region within the light cone $\omega > ck$ corresponds to continuum of radiation modes extended in the air. Dielectric and air bands (solid and dashed red curves in Fig. 2.6) frame photonic bandgap, namely a gap in frequencies within which there are no propagating modes. Low-frequency mode – dielectric band confines its optical energy in the material with the higher refractive index material, whereas higher-frequency mode - air band concentrates their energy in the material with lower refractive index material. Size of the bandgap is characterized by the dielectric contrast between waveguide material and surrounded air in case of freestanding PhC, namely higher the contrast larger the bandgap; bandgap opens up as soon as $n_1 \neq n_2$ for 1D PhC.

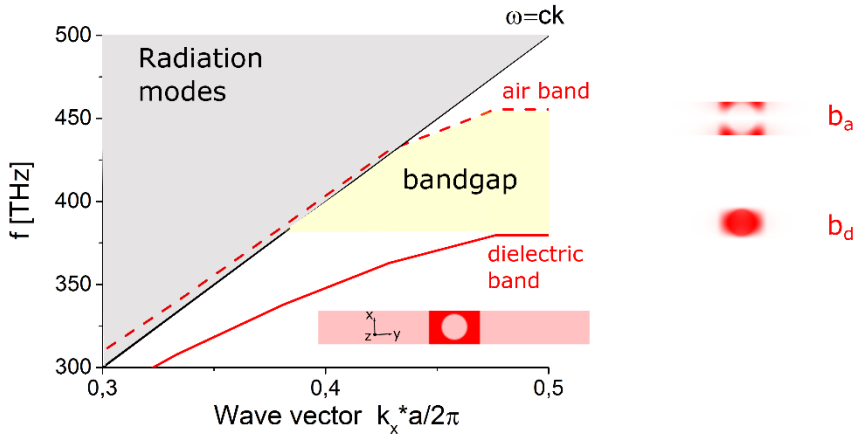

Figure 2.6. TE-like polarized Band diagram inside irreducible Brillion zone for freestanding uniform Bragg mirror, one segment of which is shown on the inset. Bandgap (yellow region) formed between dielectric and air bands, where cross-sections (z=0 plane) of time-averaged magnetic field energy density at the Brillouin-zone edge $k = \pi/a$ for each band edge shown on right panel as b_d and b_a, respectively.

Bloch modes which are above air band and below dielectric band in Fig. 2.6 propagate without scattering through photonic crystal since wavector k is conserved due to periodicity of PhC according to Bloch's theorem.

Modes within the bandgap, i.e. evanescent modes decay exponentially $e^{(-\vec{k}x)}$ into the photonic crystal since wavevector $\vec{k}$ is complex [52]. These evanescent modes are similar to guided Bloch modes (1) but with complex wavevector $\vec{k} = \vec{k}_o + i\vec{k}'$:

$$\vec{E}(\vec{x}) = \vec{u}(\vec{x}) * e^{i(\vec{k}_o\vec{x}-\omega t)} * e^{(-\vec{k}'x)}. \qquad (12)$$

R*adiated* or *extended in air modes*, *i.e.* modes within the light cone $\omega > ck$ exist for any frequency for 1D photonic crystal, therefore bandgap of 1D PhC is not complete, since only guided modes are out of the bandgap.

Origin of Resonance modes

By introducing a defect in 1D photonic crystal for instance spacing between two central holes, so that the structure represents two Bragg mirrors with a cavity in between, it can be excited *resonance (localized) modes* inside the bandgap, which are trapped (localized) in finite region, *i.e.* between two Bragg mirrors, therefore resonance modes are discrete. Resonance mode is confined by the badgap in the longitudinal direction and by index guiding (total internal reflection) − in the two transverse directions, thus state is localized only in one dimension in 1D PhC cavity.

Thus, in such PhC cavity with introduced cavity region extended state with exponential decay in crystal is trapped in between two mirrors, which is equivalent to combination of two plane waves moving in opposite directions, their superposition results in standing wave. It is considered TE-like standing cavity mode with E_y and H_z – major field components. Magnetic field distribution of standing wave can be found as

$$H_z = cos(\omega t - kx) + cos(\omega t + kx) = 2 * cos(\omega t) * cos(kx)\ , \qquad (13)$$

where a – period of photonic crystal, ω – frequency of resonance mode, $k = \frac{2\pi}{\lambda} n_{eff}$ – wavevector where taking into account Bragg's law [45] $\lambda = 2 * n_{eff} * a$, wavector $k = \frac{\pi}{a}$.

Electric and Magnetic components of standing wave are shifted on $\frac{\pi}{2}$ in space and time, therefore electric field distribution can be determined as:

$$E_y = cos\left(\omega t + \frac{\pi}{2} - \left(kx + \frac{\pi}{2}\right)\right) + cos\left(\omega t + \frac{\pi}{2} + \left(kx + \frac{\pi}{2}\right)\right) = 2 * sin(\omega t) * sin(kx). \quad (14)$$

Since planes of oscillations of H_z and E_y are orthogonal, Poynting vector can be determined as

$$S_x = E_y * H_z = sin(2\omega t) * sin(2kx)\ . \qquad (15)$$

As can be seen Poynting vector oscillates with double frequency in time and space compare with fields distribution of standing wave.

Quality factor

Introducing a defect breaks translational symmetry leading to not conserved wavevector $\vec{k}$ and, taking into account that bandgap is incomplete in 1D PhC, this results into coupling of resonance modes into light cone yielding in intrinsic radiation loss [52]. To evaluate the loss in the PhC cavity it is introduced Quality factor Q – characterizes number of optical loops of light inside the cavity while energy of resonance mode decays by $\exp(-2\pi)$, in another words it indicates lifetime of the localized mode inside the cavity [52]. 1/Q characterizes rate of decay, *i.e.* damping of the resonance mode in cavity. It can be allocated two main damping mechanisms of the resonance mode in 1D PhC cavity:

- coupling of resonance mode into radiative mode extended in the air (decay rate $\frac{1}{Q_{rad}}$)
- decay into dielectric waveguide (decay rate $\frac{1}{Q_{wg}}$).

Thus, Quality factor is determined by expression:

$$\frac{1}{Q} = \frac{1}{Q_{wg}} + \frac{1}{Q_{rad}}. \qquad (16)$$

Increasing number of holes in Bragg mirrors from both sides of cavity results into deeper penetration of the mode into the mirror yielding in exponential rise of Q_{wg}. Ideally Quality factor of 1D PhC cavity with two perfect mirrors, *i.e.* with infinite number of periods, saturates and is limited by only Q_{rad}. Thus, it is important to minimize radiation loss, *i.e.* minimize leakage of the resonance modes into surrounding cladding (air in considered case). To achieve that, spatial tails of Fourier harmonics of the resonance modes should be stayed out of the light cone, which can be provided by gentle tapering envelope function of electric field of resonance mode at the cavity edges [54]. This can be obtained by Gaussian attenuation [54] of the electric field inside PhC cavity, which is achieved either by tapering holes sizes which are drilled in the waveguide or tapering width of waveguide keeping other parameters constant [55][57][58][59]. It should be noted that *sinc*-function of electric field envelope allows complete illumination Fourier components from the light cone [60], another method to ensure smooth adiabatic transition between Bloch and guided modes is changing hole spacing, as was used in [61][62].

Attenuation profile

The Gaussian attenuated electric field and magnetic field of the first fundamental resonance mode, *i.e.* TE-like standing wave, inside PhC cavity for case when electric field has a node in the center of the cavity is described by:

$$E_y = \sin\left(\frac{\pi x}{a}\right) * \sin(\omega t) * \exp(-\sigma x^2)\exp(-\rho y^2), \qquad (17)$$

$$H_z = \cos\left(\frac{\pi x}{a}\right) * \cos(\omega t) * \exp(-\sigma x^2)\exp(-\rho y^2), \qquad (18)$$

where $1/\sqrt{\sigma} \gg 1/\sqrt{\rho}$ since field distribution along longitudinal direction (x-axis) is much longer than along y direction, a – period of photonic crystal, ω – resonance frequency, σ and ρ – attenuation coefficients along x and y directions, respectively.

It is introduced γ - attenuation constant, *i.e. mirror strength* which linearly increases with the distance from the center of cavity to the edges [55].

$$\gamma = \sigma x = \sqrt{\frac{(\omega_2 - \omega_1)^2}{(\omega_2 + \omega_1)^2} - \frac{(\omega_{res} - \omega_0)^2}{\omega_0^2}}, \qquad (19)$$

where ω_1 – dielectric band edge, ω_2 – air band edge, ω_0– midgap frequency.

As can be seen from (19) mirror strength achieved maximum value when resonance mode is in the middle of the gap in frequency region, *i.e.* $\omega_{res} = \omega_0$.

It is also introduced parameter *filling-fraction* of the segment to characterize single cell of PhC which includes three main parameters:

$$ff = \frac{\pi r^2}{width * a}, \qquad (20)$$

where $width$ − width of waveguide, r − radius of hole, a – periodicity length, *i.e.* lattice constant. These three main parameters determine band structure. Although variation of height of nanobeam also influences on band structure, it is pre-defined by the height of the corresponding layer in wafer.

Gaussian attenuation of electric field profile of resonance mode in PhC cavity can be obtained by quadratic tapering of the filling-fraction of the segment, whereas mirror strength should gradually increases from center to the end of Bragg mirror [55].

2.2 Local Density of States Enhancement in PhC

Spontaneous emission rate of localized emitter can be modified-affected by surrounding environment. Enhancement of spontaneous emission probability of source placed in the cavity was described by E.M. Purcell and called as *Purcell effect* [1]. Thus, photonic crystal cavity can enhance or inhibit spontaneous emission rate of the emitter positioned in the cavity region by tuning the cavity resonance wavelength coincide or not coincide with transition wavelength of the source which was proved experimentally by [63].
Spontaneous emission rate is proportional to density of final states (DOS) which is given by Fermi's Golden rule [64] where DOS is available number of states for a spontaneously emitted photon at a frequency $\omega^{(n)}$ to be occupied, DOS is defined by [65][66]:

$$DOS(\omega) = \sum_{n} \delta(\omega - \omega^{(n)}) \qquad (21)$$

DOS value can be enhanced in photonic crystal cavity in case, if spontaneous emission couples into resonance mode of the cavity, or suppressed in case, if there are no localized modes in the bandgap, or spontaneous emission wavelength is not coincided with resonance mode.

It is introduced *Local Density of States* $LDOS(x, \omega)$ to characterize $DOS(\omega)$ in a specific position x and in certain direction l, defined by [65][66]:

$$LDOS_l(x, \omega) = \sum_{n} \delta(\omega - \omega^{(n)}) * \varepsilon(x) * \left| E_l^{(n)}(x) \right|^2, \qquad (22)$$

where $\varepsilon(x)$ – dielectric permittivity of material, $E_l^{(n)}(x)$ – field component of the standing wave inside the cavity.

Thus, $DOS(\omega)$ can be determined as:

$$DOS(\omega) = \sum_{l=1}^{3} \int LDOS_l(x, \omega) * d^3 x. \qquad (23)$$

LDOS is proportional to the power of the radiated emission [67], where radiated power is proportional to overlap integral between electric field distribution of resonance mode localized in the cavity and electric field of the dipole-source, thus LDOS can be derived as [67]:

$$LDOS_l(x_0, \omega) = \frac{4}{\pi} \varepsilon(x_0) P_l(x_0, \omega), \qquad (24)$$

where $P_l(x_0, \omega)$ – power radiated by the linearly polarized source positioned at x_0.

Resonant mode localized in the cavity can be approximated by the mode with complex eigen-frequency $\omega = \omega_0 - i\alpha$, where $\alpha > 0$, which ensures exponential decay of the mode in photonic crystal mirror, thereby Quality factor of this mode can be expressed as $Q = {\omega_0}/{2\alpha}$ [52]. LDOS on resonance at $\omega^{(n)}$ is derived by [52] as:

$$LDOS_{res} \approx \frac{2}{\pi\omega^{(n)}} * \frac{Q^{(n)}}{V^{(n)}}, \qquad (25)$$

where $V^{(n)} = \frac{\int \varepsilon \left|E^{(n)}\right|^2}{\max \varepsilon \left|E^{(n)}\right|^2}$ - referred as Mode Volume [1][68], ${Q^{(n)}}/{V^{(n)}}$ referred as *Purcell factor* [1].

It should be noted that resonance (lossy) mode localized in cavity yields into Lorentzian peak in total power radiated by the source, thus as well in LDOS spectrum as shown in [22], enhancement factor of such mode is an average over LDOS over the emission linewidth. Lossless resonance mode leads to *delta*-function peak in the LDOS spectrum.

Purcell effect is also referred as enhancement in the LDOS at the resonant peak. Purcell enhancement factor $F_{Purcell}$ equals to the the ratio of spontaneous emission rate Γ of emitter coupled to the resonant mode of the cavity, which is matched with transition line, to the bulk case Γ_0 [1][69]:

$$F_{Purcell} = \frac{\Gamma}{\Gamma_0} = \frac{3}{4\pi^2} * \left(\lambda^{(n)}\right)^3 * \frac{Q^{(n)}}{V^{(n)}}, \qquad (26)$$

where $\lambda^{(n)} = {\lambda_{vac}^{(n)}}/{n_{mat}}$ – resonance wavelength of the mode within the material surrounding the emitter with refractive index n_{mat}.
It should be noted that (26) is valid, when the linewidth of the cavity mode is broader than transition linewidth of the emitter, and when the source is positioned in the antinode of electric field of resonance mode [69]. It was achieved a huge progress in the approaches to increase Purcell enhancement factor, which can be obtained either by increasing Quality factor [55][57][58] [70][71] or suppressing mode volume [29].

2.3 Non-classical light

It can be distinguished three classes of light according to the temporal distribution of emitted photons from the source and standard deviation of their photon number distribution: coherent light (random) with constant optical power, chaotic (bunched) and non-classical (quantum or antibunched). Classes of light are considered separately according to the statistics distribution and second-order correlation function.

Poissonian light describes coherent light which has constant optical power, frequency and phase but random time-intervals between emitted photons, namely probability of registration n photons is given by Poissonian statistics $P(n) = \frac{\bar{n}^n}{n!} exp(-\bar{n})$, where $n = 0,1,2, \ldots$, $\bar{n}$ – mean value around which current random number of photons fluctuates with standard deviation $\sqrt{\bar{n}}$ [73].

Super-Poissonian light characterizes electromagnetic radiation with fluctuated in time intensity, such as thermal light from black-body radiation and chaotic light (partially coherent) from single spectral line of a discharge lamp, for instance. The number of photons follows Bose-Einstein distribution of black-body radiation with standard deviation $\sqrt{\bar{n} + \bar{n}^2}$ [73], which is broader than for Poissonian distribution as a consequence of thermal fluctuations of number of photons n. In principle, the first term $\bar{n}$ can be related with discreet number of photons, while $\bar{n}^2$ linked to thermal fluctuations.

Sub-Poissonian light describes non-classical light where there is constant time interval between emitted photons. The probability of having 1 photon is unity, while standard deviation is less than $\sqrt{\bar{n}}$.

Quantum nature of emitted light can be proved by performing Hanbury Brown and Twiss (HBT) experiment [74] [75], where emitted light is directed on 50:50 beam splitter and impinged to two detectors, where coincidences between detection events are collected. Second-order correlation function between signals from both arms can be found as [73]:

$$g^{(2)}(\tau = 0) = \frac{<I(t) * I(t+\tau)>}{<I(t)> * <I(t+\tau)>}, \qquad (27)$$

where $I(t)$ in the experiment characterized by count rate detected by the first detector at time t, $I(t + \tau)$ is count rate detected by the second detector at time $t + \tau$.

Ideal single photon source emits one photon in a time, while the second photon will be emitted only after new pump-emission cycle, therefore top level of emission count rate is limited by the lifetime of the single-photon source. Obviously, for ideal single-photon emitter probability of emitting two photons simultaneously is zero, therefore, $g^{(2)}(\tau = 0) = 0$. Thus, it can be observed non-classical *antibunching* dip in the autocorrelation diagram [76].

However, photon statistics can be degraded, due to the optical loss on the all way of the light beams, in particular in the beam splitter (also not perfectly equal splitting ratio), inefficient collection and detection, and due to background photons resulting in not constant time intervals between detected photons. Consequence of all mentioned is measured $0 < g^{(2)}(0) < 0.5$ for single-photon emitter [76], while in the worst case when the loss are high, sub-Poissonian statistics can degrade to Poissonian case.

$g^{(2)}(0)$ intuitively characterizes probability of emission single photons towards multiphoton emission. Thus, for classical light $g^{(2)}(0) \geq 1$ and $g^{(2)}(0) \geq g^{(2)}(\tau)$, namely coherent (random) light described by Poissonian statistics which characterized by $g^{(2)}(0) = g^{(2)}(\tau) = 1$, while light described by Super-Poissonian statistics characterizes $g^{(2)}(0) > 1$ and $g^{(2)}(0) > g^{(2)}(\tau)$ [73].

2.4 DBT molecule as single photon source

Ideal single-photon source

An ideal single-photon source would have the following properties:

- 100% probability of emitting single photon, thereby $g^2\,(0) = 0$, probability of multiphoton emission is 0%,
- emission single photons on-demand, *i.e.* at intervals defined by periodic optical or electrical excitation,
- negligible intrinsic jitter (dephasing) to obtain constant time intervals between emitted photons as a response on excitation signal,
- indistinguishability of emitted photons.
- Top level of repetition rate of photon emission is limited by the lifetime of the emitter

However, real single photon source has parameters varied from ideal one where 'degree' of single photon emission is determined by $g^2\,(0)$ value measured in Hanbury-Brown Twiss experiment, which can be limited by jitter of the detector, collection efficiency and signal/noise ratio of optical setup. It is important to note, that triggered single photon source emits non-classical light, whereas attenuated laser emits photons according to Poissonian statistics.

Dibenzoterrylene (DBT) molecule

DBT is dye molecule [25]. Structure of energy level of the molecule determines physical properties and emitted spectrum. In general, in molecule can occur electronic, vibrational and rotational excitations which contribute into shaping of energy levels, where electronic transitions occur in visible range, vibrational and rotational – in IR and Microwave region. For molecule embedded in host matrix it should be considered only electronic and vibrational excitations, since rotational excitation can be neglected which is the case of considered DBT molecule which is commonly a guest in solid matrix [26].

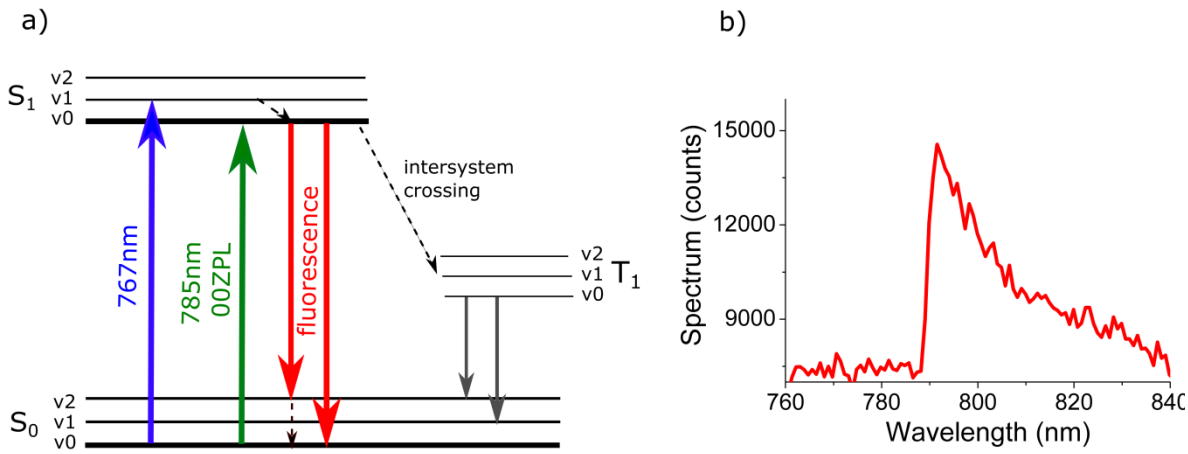

Figure 2.7: a) Jablonski diagram of DBT:Ac presenting molecular electronic levels S_0 , S_1 , triplet level T_1 with vibronic states $v0 - v2$ and transitions between them. Blue and green arrows indicate pump light in case on *non-resonant* and *resonant* excitation, respectively. Red arrow shows red-shifted emitted fluorescence. Dashed arrows label non-radiative decays. **b)** Fluorescence spectrum of DBT:Ac under 767 nm excitation measured at room temperature where the left part of the spectrum is cut by inserted long-pass filter to remove pump light.

As can be seen on diagram in Fig. 2.7 a) to excite DBT molecule strong singlet-singlet transition is pumped on 767 nm into one of vibrational levels of the first electronic excited state S_1 via absorption of a photon, follows by fast non-radiative transition, *i.e. vibrational relaxation* through exchanging energy with surrounding environment on the time-range of picoseconds, thus molecule decays to the ground level $v = 0$ of S_1 level. Lifetime of S_1 level is much longer (several nanoseconds). After that DBT spontaneously decays from ground level of first exciting state $S_{1,v=0}$ to the different vibrational levels of the S_0 ground state through fluorescence emission transition. Vibrationally excited states $S_{0,v\neq0}$ then relaxes to ground stated of $S_{0,v=0}$. Thus, originated *fluorescence* shown in Fig. 2.7 b) is red-shifted (usually in visible range) in respect to excitation, *i.e.* wavelength of fluorescence and excitation are different, such excitation called *non-resonant pumping*.
Transition from ground level $S_{1,v=0}$ to any vibrational state level of S_0 referred as Zero Phonon Lines (ZPL), whereas *00-ZPL* referred to purely electronic transition from ground vibrational level $S_{1,v=0}$ to ground state $S_{0,v=0}$ and it is the narrowest one (natural width ≈40 MHz [77]). 00-ZPL can be excited by so called *resonance excitation*.

At any temperature higher than absolute zero molecule interacts with host (solid) matrix which leads to appearing Phonon Side Bands (PSB) in the emitted spectrum, thus probability of ZPL is zero, in this case PSB can be approximated by Gaussian function. Whereas at cryogenic temperature < 40 K ZPL are resolved and can be approximated by Lorentzian function, where the width of the peak 00-ZPL described by lifetime of the excited state of the molecule; PSB are as well resolved and in this case can be expressed by Poissonian distribution, since they

shows quantized electronic transitions incorporating phonons. PSB is red-shifted in respect to ZPL.

Lifetime of DBT

Lifetime of ground vibrational level of first excited electronic state $S_{1,v=0}$ is governed mainly by fluorescence, however another decay mechanism – *intersystem crossing* influences as well. Intersystem crossing referred to nonradiative transition from singlet to triplet level or opposite from triplet to singlet level. Probability of intersystem crossing ($S_1 \rightarrow T_1$) and ($T_1 \rightarrow S_1$) is low. Radiative decay from excited triplet state $T_1 \rightarrow S_0$ is called *phosphorescence*, which is slow form of relaxation (1.5μs [27]). It should be noted that $S_1 \rightarrow T_1$ transition interrupts fluorescence signal, this effect referred as *blinking* [78], resulting in discrete switching on-off process of individual molecule.

Since probability of non-radiative processes are very low, Quantum Yield (QY) close to 100% [25], it is determined as ratio of decays rate of radiative processes to the sum of rates of radiative and non-radiative of the molecule, *i.e.* ratio between number of emitted photons and number of absorbed (pumped) photons.

Host Matrix for DBT

The molecules should be embedded into crystal (host matrix) in order to avoid oxidization and also ensure optical stability as well as preventing thermally induced overheating [23]. Moreover, by controlling thickness of host matrix it can be controlled the distance between the molecule and photonic device surface, which is important for efficient evanescent coupling to waveguide mode of the photonic device.

In the current work it was chosen to use Anthracence (Ac) [25] as a host crystal.
Anthracence host matrix has the following advantages:

- Ac is stable at room and cryogenic temperature.
- Ac ensures low probability of intersystem crossing, since triplet level of Ac is higher than first excited singlet level S_1 of DBT [25], resulting in higher count rate of emitted fluorescence signal.
- For further integration DBT:Ac on Si_3N_4 photonic device it is important that effective refractive index of Ac crystal is 1.8 which is lower than for Si_3N_4. Furthermore, the chip can be easily covered by the solution by means of spincoating.

DBT:Ac as single photon emitter

DBT is good candidate as integrated single photon emitter because of the following properties:

- concentration of DBT in the solution DBT:Ac can be controlled by dissolving in toluene to obtain suitable, *i.e.* insuring one molecule in the diffraction-limited excitation beam spot. Thus, single molecule can be investigated individually by tightly focused pump light an allowed transition.

- Spectral selection can be obtained at cryogenic temperature, where excitation light can be tuned to match particular one molecule linewidth, where narrow emission is lifetime-limited 40 MHz [77].
- On-demand single photon emission can be obtained under pulsed optical excitation, where duration of pump pulse (ps range) should be much shorter than lifetime of the molecule (3-4 ns), whereas CW excitation light leads to emission single photons with random time intervals in between [23] .
- High fluorescence Quantum Yield obtains almost 100% [25], which ensures high fluorescence emission rate 10^6 per second [27].
- Low probability of inter system crossing which is also suppressed by host matrix (Ac), thus it can be neglected.
- Near-Zero probability of emitting two photons simultaneously [23].
- Fluorescence wavelength lies in the wavelength region (770-890 nm), where Si_3N_4 as potential material for integrated photonic devices in the visible range has high transparency and silicon photodiodes have high Quantum Yield.
- Host matrix allows integrating molecules on photonic devices on the chip and controlling the distance between emitter and waveguide.
- High photostability (flux of molecules emission 10^{12} before photobleaching [27]).

Easy removing recipe process of DBT:Ac by help of Acetone allows to re-use photonic devices on the chip many times.

2.5 Concluding remarks

Engineered and examined scalable nanophotonic elements are the solid base of integrated circuit on chip. However, modification and optimization of the architecture of each photonic component can improve their main characteristics and extend the utilization applications, which is the topic of the next Chapters in this Thesis. The main goal is to integrate single photon source with optical components in one circuit, which provides enhancement of emitted light, and spatial separation and filtration of excitation light on chip. Integrated grating couplers as output ports should allow to read enhanced single photon signal.

One of the promising candidates as single photon source is DBT molecule, due to its photostability at room and cryogenic temperature, almost unitary Quantum Yield, negligible photobleaching. Furthermore, embedding this source into host matrix besides preventing oxidization of molecules also makes it simpler to integrate molecules on chip by means of spincoating. Moreover, host matrix makes possible to control the distance between emitter and waveguide by preparation crystals different shape/thickness.

One of the first demonstrations of integration single DBT in photonic circuit is examined in the Chapter 6.

3. Cascaded Mach-Zehnder Interferometer as a tunable filter on chip

Motivation

Realization scalable optically driven single photon sources requires optical filtration of excitation light much stronger that single photon emission to guarantee indistinguishability of the emitted photons. Single photon sources as NDs, SCNTs and organic molecules are good candidates for integration into nanophotonic circuits due to their unique properties discussed in the Paragraphs 1.2 and 2.4.

The goal of work explained in this chapter was to realize compact optical filters integrated in nanophotonic circuit on-chip, whereas cascading several filter stages allow enhancing the overall filtration depth, by pricing increase of insertion optical loss. Another important aspect is tunability of filtering wavelength, which was provided by tuning refractive index via thermo-optic effect [80][81][82][83][84][85][86] with help of local micro-heaters integrated on chip. Such filters can be integrated in photonic circuits with evanescently coupled single photon emitter, in particular SiV.

In this chapter it is shown realization of single and cascaded thermo-optic compact tunable Mach-Zehnder interferometer (MZI) on silicon nitride-on-insulator platform equipped with spiral and meander shaped microheaters. In both cases tunability was ensured by microheaters placed on both branches of MZIs on chip, thus making possible for achieving simultaneously maximum and minimum transmission on required wavelengths, in particular wavelength of SiV fluorescence (λ=740 nm) and excitation light (λ=532 nm), respectively.

3.1 Single MZI thermo-optical tunable filter

The focus of the work was to design and fabricate low-loss thermo-optic MZI based on silicon nitride platform.

Silicon nitride provides broadband optical transparency (visible-NER) [87], sufficient index contrast with SiO_2, thus enables tight mode confinement, increasing density of devices on the chip. At the same time the index contrast is not as high as silicon-on-insulator (SOI), which reduces scattering losses and increases tolerance to the fabrication imperfections (errors).

Wavelength tunabilty of the MZI filter can be achieved by dynamically changing optical path difference between arms which can be done either by altering effective refractive index of the mode in one of the arms or by changing physical length difference Δl between arms. In our nanophotonic circuits the physical length difference Δl remains constant. Therefore, the solution is an introduction thermally induced phase shift $\Delta\varphi$ for the light travelling through one of the arms of MZI, which can be realized by placing metal microheaters on top of MZI branch, thus waveguide beneath undergones a temperature change ΔT which will change effective refractive index in the heated arm of MZI.

MZI photonic device on-chip consists two branches, namely long waveguides which are recombined by Y-splitter, where designed pass difference is rather small - 25μm in order to have FSR≈10.47 nm at λ=738 nm (9). To induce phase shift via refractive index change through thermo-optic (TO) effect metal microheaters were employed. Nanophotonic structures were covered with fabricated cladding buffer layer to isolate optical mode from metal microheaters, *i.e.* to avoid absorption loss due to existence of metal in the vicinity of optical mode. Relatively small thermo-optic coefficient for silicon nitride ($\frac{\mathrm{d}n}{\mathrm{d}T}\sim 10^{-5}\ \mathrm{K}^{-1}$ [88][20], approximately ten times lower than in silicon) leads to a weak modification of the refractive index as a result of TO effect, therefore both branches of MZI consisted long waveguides (1.32-3.75 mm) to induce essential thermal phase shift in one of arms of MZI via heating, and hence rise the amplitude of the shift of the interference fringes of the MZI. To increase effectiveness of the heating, waveguides in both branches were folded into spiral design to concentrate the heat in the center; such geometry at the same time provides a compact device footprint.

Two types of phase shifters were realized: spiral and meander shapes microheaters, which were settled on top of cladding layer covering spiral folded waveguide as illustrated in Fig. 3.1. Stripe was centered in case of spiral-geometry microheater, *i.e.* aligned with the center of waveguide to maximize lap over heat with the guided optical mode of the waveguide.

Applying a voltage to the microheaters beneath waveguide was locally heated leading to induced phase shift φ_{shift} in the MZI arm. The phase difference at the output of the thermo-optic MZI after heating the longer arm can be expressed as

$$\Delta\varphi = \Delta\varphi_{\text{fixed}} + \varphi_{shift} = \frac{2\pi}{\lambda}\Delta l * n_{eff} + \frac{2\pi}{\lambda}(l_{spiral} + \Delta l) * \frac{dn}{dT}\Delta T\ , \qquad (28)$$

the phase difference at the output of thermo-optic MZI while heating the shorter arm can be expressed as

$$\Delta\varphi = \Delta\varphi_{fixed} - \varphi_{shift} = \frac{2\pi}{\lambda}\Delta l * n_{eff} - \frac{2\pi}{\lambda} l_{spiral} * \frac{dn}{dT}\Delta T\ , \qquad (29)$$

where λ is the desired wavelength in the vacuum, Δl is the original fixed length difference between the arms, l_{spiral} is the length of the spiral-arm waveguide, n_{eff} is the effective

refractive index of the guided mode, $\frac{dn}{dT}$ is the thermo-optic coefficient of silicon nitride and ΔT − induced temperature change.

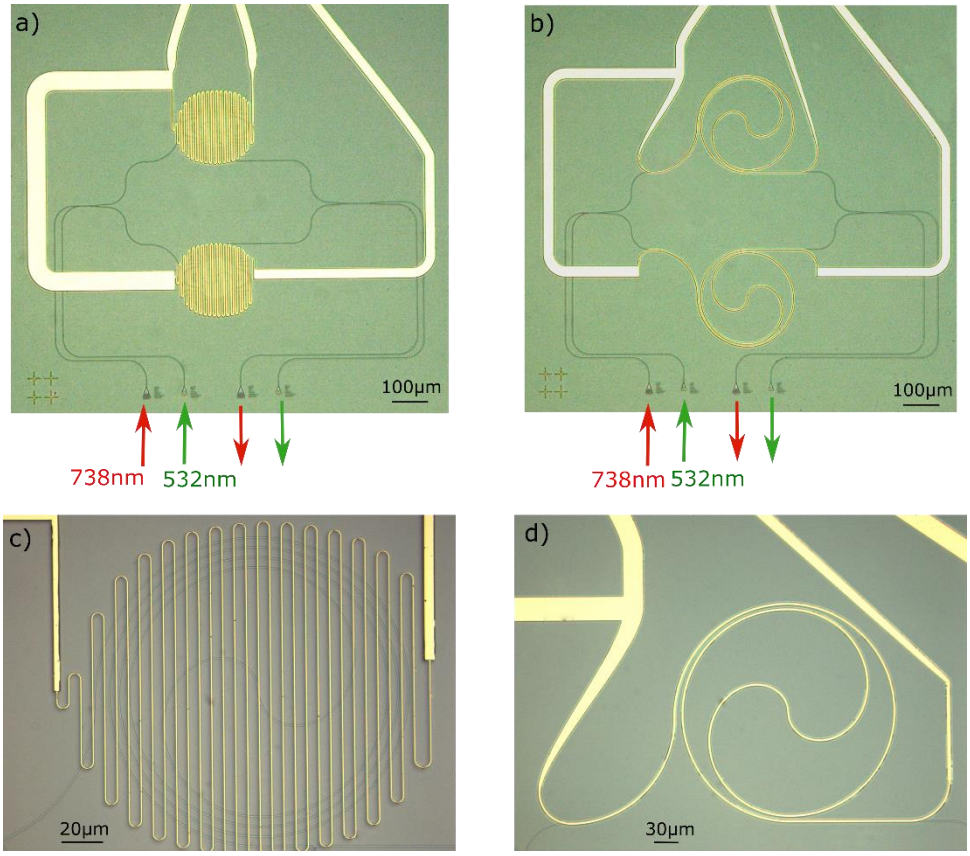

Figure 3.1. Optical micrographs of thermo-optic single MZI equipped with **(a)** double-meander and **(b)** double-spiral shaped microheaters on top of both arms of the MZI with zoom-in on **(c)** meander (width=0.5 μm) and on **(d)** spiral-shaped (width=3 μm) microheaters, Si_3N_4 spiral-folded waveguide is beneath.

The temperature difference which corresponds to the switching power P_π induces π-phase shift ($\varphi_{shift} = \pi$) from (1, 2) was determined as

$$\Delta T_\pi = \frac{\lambda}{2 * l_{spiral} * \frac{dn}{dT}} \quad , \qquad (30)$$

The main advantages of used approach are the following:

- Spiral-arranged thermo-optic MZI provides low-power operation compare to straight arms, since the heat concentrated in the center of the spiral, in particular lateral diffused

heat is employed [80][81][82], furthermore such device ensures small footprint to increase density of devices on the chip.

- In contrast with previously performed works [80][81][83] designed and fabricated thermo-optic MZI in this thesis equipped with microheaters on top of both branches, thus the amplitude of the induced shift of the interference fringes is doubled, namely by applying voltage separately to the microheater on top of the two arms the interference fringes will be either shifted in the long wavelength range or low-wavelength range.

3.2. Design of the chip, fabrication and requirements

Design of photonic devices on chip (Fig.3.2 c)) consisted several matrixes arrays of single and cascaded thermo-optic MZIs with spiral and meander architecture microheaters where geometrical parameters: length of spiral-arm waveguide and heater stripe deposited on buffer layer, inner radius of bending for both waveguides and spiral-shape heater, width of the heater rail, were finely varied in order to determine optimized parameters. Moreover, array of thermo-optic MZI devices with spiral waveguides with placed on top microheater stripes of different length and shape as well as reference devices were realized on the same chip to define propagation, insertion loss and for transmission normalization, respectively. To couple light in and out to the photonic circuit each device was equipped with four grating couplers as two input and output ports (Fig. 3.1) which also play role of TE-polarizers to prevent degradation of interference fringes in terms of extinction ratio. To examine thermo-optic behavior of devices (shift of interference fringes) in broad wavelength range in visible region (500-800 nm) photonic devices with alteration of grating coupler's periods were designed. The waveguide width was estimated from numerical simulations with COMSOL [44] providing single TE-like mode for λ=738 nm at a width of 450 nm (Fig 3.3 a)).

Scalable matrixes of photonic devices were realized on Silicon nitride-on-insulator chip, which consists 200 nm stoichiometric Si_3N_4 on top of 2000 nm buried silicon dioxide on top of silicon. Fabrication of the nanophotonic circuits was carried out using several steps of electron-beam lithography (e-beam) followed by reactive ion etching.

- In the first e-beam lithography step alignment markers were defined on the chip with positive photoresist PMMA (4.5%) and further developed in MIBK:IPA (1:3). Gold (120 nm) with chromium (10 nm) adhesion layer were deposited on chip by electron-beam evaporation followed by lift-off process in acetone [89].
- In the second lithography step the nanophotonic circuits were defined using negative photoresist (ma-N 2403), followed by development in MF-319 for 1 min and reflow process. The waveguides were subsequently dry-etched into the silicon nitride layer using a CHF_3/O_2 plasma.

- During the third fabrication step silicon dioxide buffer layer was realized.
  Cladding layer of thermo-optic photonic device should be sufficiently thick to isolate microheater from optical mode to prevent absorption, outstay for high temperatures and last but not least – any cladding layer should be lower-index than the waveguide material, therefore silicon dioxide buffer layer was used. As a lower-cost and easy alternative to SiO_2 deposition hydrogen silsesquioxane (HSQ) − inorganic polymer [90] was employed. Thus, for development dioxide buffer, HSQ was subsequently deposited on top of the photonic devices on the chip by means of spincoating and then thermally cured resulting in (complete) disassociation of Si-H bonds in HSQ [91].
- In the third e-beam lithography step the design of microheaters and contact pads were transferred into PMMA resist layer (850 nm thickness). After development in MIBK:IPA microheaters and contact pads on the chip it was deposited 10 nm Cr adhesion layer and 120 nm of Au, followed by lift-off in acetone.

During the last two lithography steps position and orientation of the chip were carefully aligned by help of aligned metal markers produced in the first step, resulting in precise e-beam exposing of mask for microheaters on the etched nanostructures, especially in case of spiral-shape microheaters which were co-centered with beneath waveguide. Optical micrographs of fabricated thermo-optic MZIs are shown in Fig. 3.1.

Requirements to materials for thermo-optic filter

To realize thermo-optic filter with low-switching power, *i.e.* to increase heating efficiency, the following requirements should be satisfied:

- Cladding and waveguide material should have low thermal conductivity to slow the rate of heat transfer from the waveguide to environment around. In fact, this will lead in increasing switching time, therefore trade–off between power consumption and temperature switching must be considered, however thermo-optic switch is not an interest of current work. Thus, power consumption of fabricated thermo-optic MZI benefits from not high thermal conductivity of produced upper cladding – porous hydrogenated silicon dioxide layer [90] which is approximately five times less than in SiO_2 at the price of increasing time response.

- Cladding and waveguide material should have low heat capacity

3.3. Optimization of single thermo-optic MZI in two configurations

In the first step devices on the chip were characterized optically via transmission measurements which were performed on optical *fiber-array* setup (Fig.3.2).

Fiber-array setup

Fiber-array includes row of 8 fibers with separation 250μm fixed in the glass cover. Therefore, the distance between input/output ports, *i.e.* grating couplers in the fabricated devices, is multiple of integer number of this separation distance as shown in Fig. 3.2 d). Fibers in fiber array are cleaved at 8° to prevent backscattering light as depicted in the sketch in Fig. 3.2 e). Therefore, the first step of alignment was fixing the respective tilt angle of the fiber-array stage.

Chip was placed on piezo translation-rotation stage as shown in Fig.3.2 a),b) and aligned with respect to an optical fiber array which was observed by CCD camera. The fiber array should approach the chip closely better, to achieve higher transmission, but avoiding touching with fiber of the chip. Supercontinuum light from white-light laser source (Leukos SM-30-UV) carried in single mode optical fiber was coupled to the photonic circuit via Bragg diffraction on apodized grating coupler (subject of Paragraph 2.1.2) as shown in Fig. 3.2 e). Transmitted light through the device was diffracted on the second coupler, directed by further optical fiber and detected by either spectrometer or low-noise detector. Transmitted signal facilitates to further optimize position of the chip in respect to fiber array.

Since the aim of this work was to design tunable filter for integration SiV in the circuit, such filter should be able to cut pump light on λ=532 nm and transmit with maximum efficiency emitted florescence light (λ=738 nm), therefore each thermo-optic MZI was supplied with two input and output ports – grating couplers (see Fig.3.1) designed to couple in/out wavelength range of 738 nm and 532 nm, respectively with several 10 nm bandwidth. Waveguides from both grating ports were combined with a Y-splitter, thus making possible to explore MZI filters in both wavelength ranges.

In the second step of experiments thermo-optical performance of filters was analyzed by applying DC voltage to one of the metallic pads connected with microheaters on top of the both arms of each thermo-optic MZI device through RF contact probes, placed head-to-head with the fiber array.

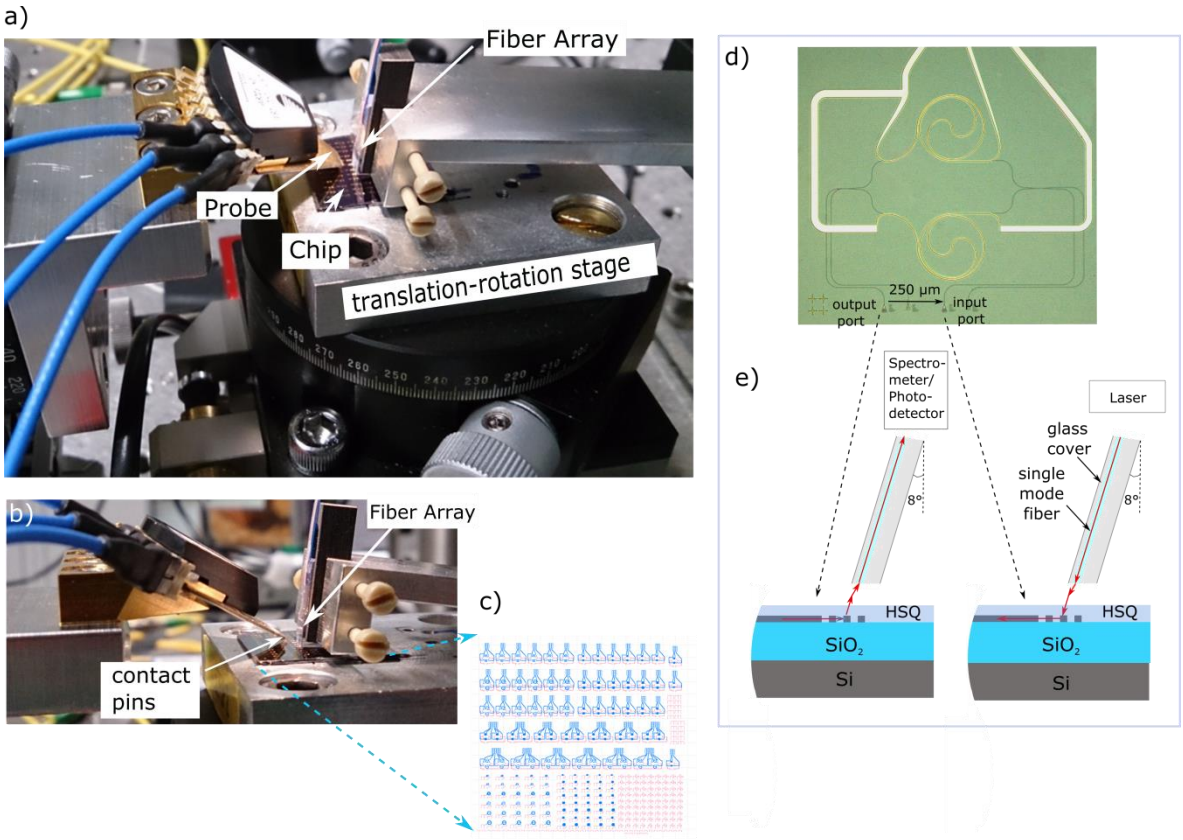

Figure 3.2. **a)** Fiber array measurement setup, where the chip is positioned on translation-rotation stage under fiber array, RF probe is placed head-to-head to the fiber array. **b)** Pins of the probe are in contact with metal pads connected with microheaters on the chip. **c)** GDS-design of fabricated chip. **d)** Optical micrograph of thermo-optic single MZI equipped with spiral microheaters. **e)** Sketch of transmission measurement on fiber-array setup.

The propagation loss of the waveguide is important characteristic of designed device since each arm of MZI consisted long waveguide to increase shift of interference fringes under applying voltage to microheater insuring low power consumption. The propagation loss of the Si_3N_4 rib waveguide was determined on the same chip as the thermo-optic MZIs by measuring the transmission of photonic devices with spiral waveguides with variation of length in the range 1-6.3mm as shown in Fig. 3.3 d)-f) with the same radius of bending and identical width of microheaters deposited on top of buffer HSQ layer, thus keeping radiation loss on bends constant. Thus, measured average propagation loss amounts to 0.49 dB/mm at λ=766nm.

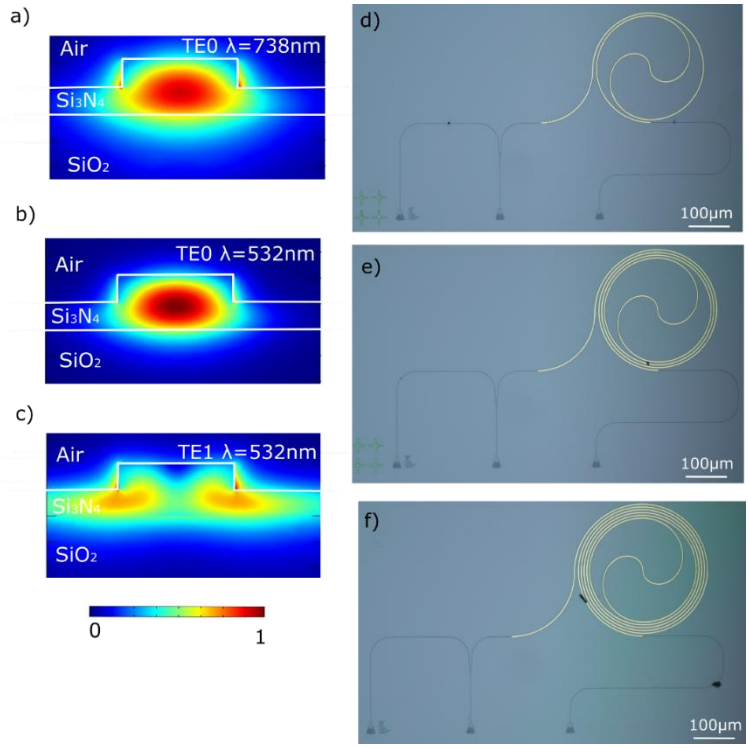

Figure 3.3. Simulated electric field profile of TE-like modes on λ=738 nm **(a)** and λ=532 nm **(b,c)** propagating in the rib waveguide. Optical micrographs of the reference photonic devices with spiral-folded waveguides, radius of inner bend 130 μm with length 1.3 mm **(d)**, 2.7 mm **(e)**, 6.3 mm **(f)** to determine optical propagation loss.

Thermo-optic MZIs with different specifications of the microheaters were designed and fabricated in order to minimize power consumption and propagation loss, and maximize extinction ratio (ER) of the interference pattern.

First goal was optimization of configuration of filter which required lower switching power P_π to obtain phase shift $\varphi_{\text{shift}} = \pi$, therefore it was considered *spiral* and *meander* shape of microheaters. Modulated normalized transmission spectrum for thermo-optic MZI devices with spiral- (violet curve) and meander-geometry (green curve) architecture of microheaters with identical heater-stripe width of 800 nm while heating only one arm shown in Fig. 3.4. Input optical signal wavelength kept fixed at λ=766 nm. Transmission spectrum was normalized for the coupling loss of two grating couplers. Measured switching power for thermo-optic MZI with spiral-shaped microheater $P_\pi = 14.83\,\text{mW}$ is more than two times

lower than with meander-shaped microheater $P_\pi = 35\,\text{mW}$. This result is expected, since spiral-shaped microheater was specifically designed to 'follow' beneath waveguide and to be aligned with the center of waveguide, thus all the length of arm-waveguide is active, *i.e.* it is heated simultaneously and uniformly. In case of meander microheater it covers only local

regions of the waveguide, thus effectively heat only these parts, while the rest length of waveguide experiences only diffusive heat.

In both geometry architecture of heaters lateral diffusion of heat should be taken into account.

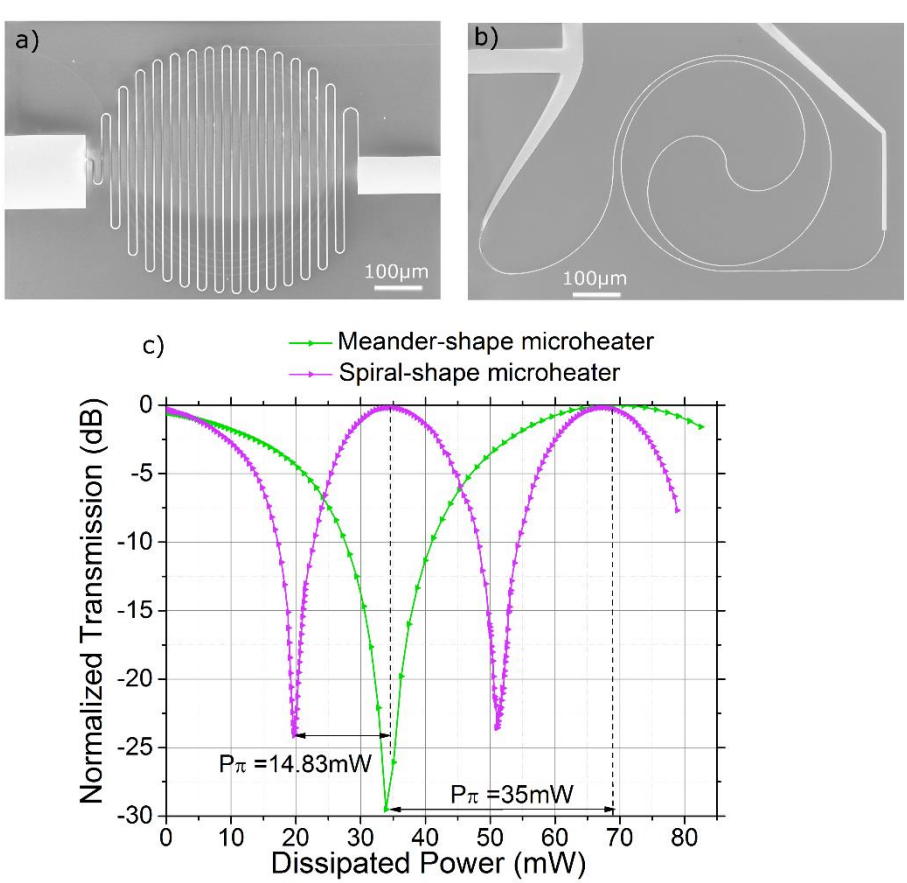

Figure 3.4. SEM images of **(a)** meander (width=800 nm) and **(b)** spiral (width=800 nm) architecture microheaters. **(c)** Modulated normalized transmission of a single MZI device equipped with double-spiral shaped (violet curve) and double-meander shaped (green curve) heaters with identical width of 800 nm of the heater. The voltage is applied to the top microheater of each MZI device. Positions of the peaks for MZI equipped with spiral- and meander- shaped microheater explained by different switching power.

The next step was optimization of geometry of microheaters to further decrease switching power. Therefore, thermo-optic MZIs with variation of radius of the inner bend, width of the microheaters and length of the heated spiral-arm waveguide was fabricated on the chip. Results are shown in Fig. 3.5. Impact of each parameter is independently investigated below.

Length of active arm-waveguide influence

Switching power of spiral-folded waveguide decreases with rising active length as shown in Fig. 3.5, where it is displayed measured dependence of shifting power on the width of heater-

stripe where colorful curves indicate different length of spiral-waveguide arm. For a thermo-optic MZI with a constant width of 800 nm of the microheater and length of spiral-arm 1.32 mm measured switching power P_π=15.7 mW, for a length of 1.78 mm - P_π=14.9 mW, while for a length of 3.75 mm measured shifting power obtained P_π=13.85 mW. The influence of accompanying decrease of the inner bend radius which helps to concentrate heat even more in the center were negligible.

On the one hand, with increasing active-heated length of arm in MZI l_{spiral} it should be utilized less switching power since it's required smaller induced temperature change ΔT to obtain $\varphi_{shift} = \pi$ according to (30). On the other hand, length of heated volume changes with alteration of active length of waveguide leading to higher switching power to provide a given ΔT. The impact of the first effect into thermo-optic process for considered spiral-shape MZIs is much higher than the second one, therefore measured switching power inevitably decreases with increasing active-heated length of MZI.

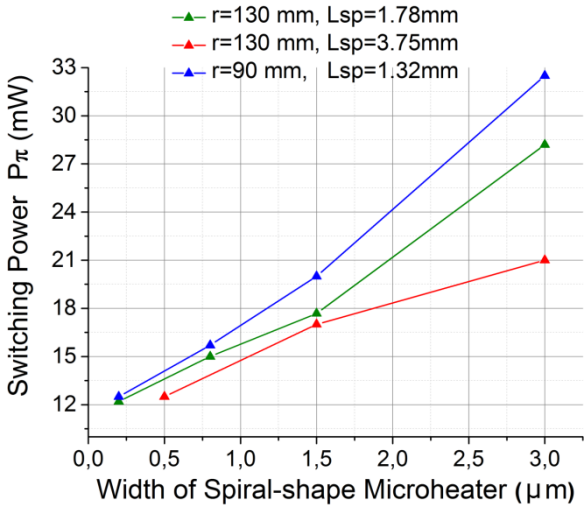

Figure 3.5. The switching power P_π of double-spiral-arm thermo-optic MZI devices equipped with spiral-shaped microheaters as a function of width of the microheater with length of spiral waveguide L_{sp} and inner radius r. Width of waveguide 450 nm.

Width of heater influence

Narrowing of the microheater-stripe when keeping the active length of the waveguide constant yields to smaller power consumption as can be tracked on Fig. 3.5. Decreasing cross-section of the microheater allows to utilize heat more effectively, *i.e.* not to lost it on heating environment around, moreover heated volume of microheater stripes is lower in this case, both of effects yields to temperature rise which decreases switching power.

Radius of inner waveguide bend influence

The impact of changing radius of inner band of spiral waveguide arm in the range 90-130um was negligible.

Experimental examination of thermo-optic MZIs equipped with meander-shaped microheaters showed that the same trends in respect of active length arm, width of microheater and radius of spiral-arm waveguide, however power consumption in this case is more than two times higher comparing with spiral-shape as shown in Fig. 3.4 because of less effectiveness of heat distribution.

Novel design of fabricated thermo-optic MZI supplied with microheaters on top of both branches enables to increase two times the amplitude of shift of the interference fringes in contrast from [80][81][83]. Interference fringes (spectra) can be shifted towards the long or short wavelength range with respect to the central wavelength by applying voltage separately to microheaters placed on both MZI arms.

The phase can be shifted by π by applying voltage which corresponds to the switching power P_π to one or another of the microheaters. Measured shift of the transmission spectra in respect to the central wavelength at λ=738 nm as a function of the electrical power applied to the microheater is displayed in Fig. 3.6 a), b).

It is observed blue-shift, *i.e.* in the short-wavelength region of interference fringes, by applying a voltage to the longer arm (top part on graphs Fig.3.6 a) ,b)) while by heating shorter arm (power dissipation at short arm is increased) of the same device fringes shifted to longer wavelength region (bottom part on these graphs).

The minimum switching power P_π=12.2 mW which corresponds to shift of fringes on half of the FSR achieved for thermo-optic MZI equipped with spiral-shaped heaters with microheater stripe width 200 nm which is roughly half of the width of the rib waveguide taking into account used dioxide buffer thickness. For this MZI the extracted induced temperature change is ΔT=20 K for a wavelength λ=738 nm. For spiral-shaped microheaters with rising the width of microheater the rate of shifting the interference fringes per mW decreases (green and orange curves in Fig. 3.6 a)), but it is still higher in comparison with meander-shaped microheaters (violet curve). The highest rate of shifting the interference fringes is 0.43 nm/mW corresponds to minimal spiral-shape microheater width 200 nm. The same trend is assigned to thermo-optic MZI equipped with meander microheater, but with lower rate of shift, as illustrated in Fig. 3.6 b). The measured insertion loss of the thermo-optic MZI with a spiral-shaped microheater (width=1.5 μm) including optical loss in two splitters is shown in Fig: 3.6 a) where the dark-violet-star-dot curve is the reflection of the light-violet-diamond dot curve.

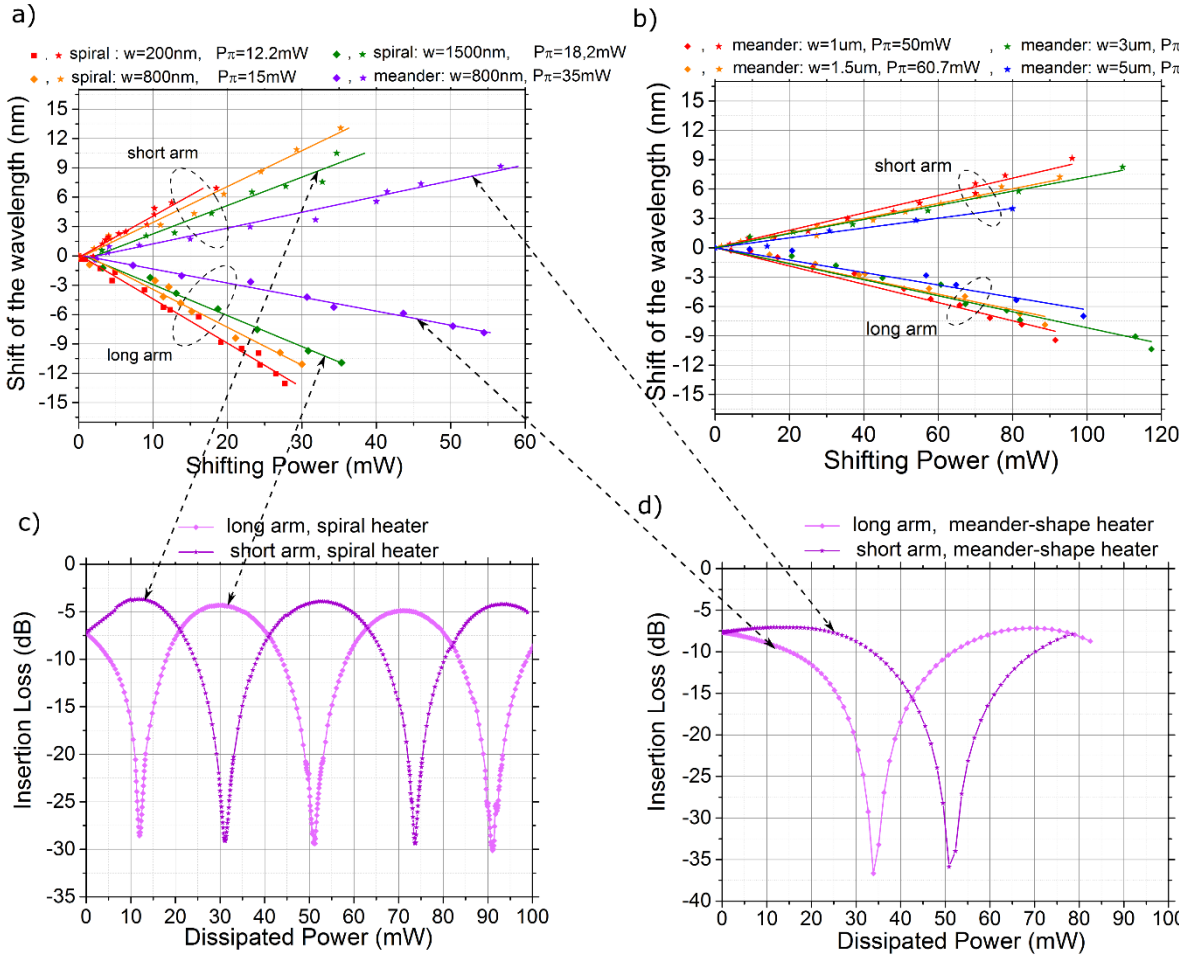

Figure 3.6. Amplitude of shift of interference fringes as a function of dissipated power of thermo-optic MZIs. **a)** The red, orange and green curves correspond to one MZI equipped with double-spiral geometry architecture microheaters, while violet curve-corresponds to MZI with double-meander microheaters. **b)** Curves belong to one MZI equipped with double-meander geometry architecture microheaters. On (a) and (b) diamond-dots correspond to the MZI long arm heating, while the star-dots correspond to the MZI short arm. The microheaters switching power and width are reported on the graph legend. Transmission of one MZI equipped with spiral **(c)** and meander **(d)** shaped microheaters, respectively, as a function of dissipated power on the long arm (light violet diamond-dot curve) and on the short arm (dark violet star-dot curve) of the MZI measured at λ = 771 nm.

Minimal switching power obtained in our experiment is en par with results from [80], with a reported P_π=6.1 mW at λ=1550 nm for a thermo-optic modulator based on silicon-on-insulator (SOI) with a spiral-shaped heated waveguide and meander-shaped heaters. However, thermo-optic coefficient of Si_3N_4 is smaller than Si, the length of the active waveguide used in [80]was approximately 3.37 times longer and the radius of the inner bend is two times less than in the investigated in this thesis thermo-optic MZI device (length 1.78mm, bend 130μm) with $P_\pi = 12.2mW$ in this thesis. Furthermore, insertion loss in [80] is around 6 dB higher compared to the insertion loss in the considered in the thesis single MZI device of 4.2 dB.

In conclusion, low power consumption thermo-optic MZI filters were designed and fabricated where minimal switching power measured in the performed experiments was obtained P_π=12.2 mW for MZI with a spiral geometry architecture microheater with width=200 nm, a spiral-arm waveguide length=1.78 mm and inner band radius=130 μm, where filtration depth achieved 20 dB. Higher ER (ER=30 dB) but lower switching power (P_π=35 mW) and higher insertion loss (6 dB) experienced meander-shape thermo-optic MZI.

3.4 Cascaded MZI thermo-optical tunable filter

To further improve filtration depth it was designed and fabricated cascaded thermo-optic devices with two MZIs shown in Fig. 3.7 a) and c). Due to fabrication imperfections for identically design of MZIs designed length difference have a slight deviation with fabricated path difference which originates a shift between positions of maximums in the interference pattern of both MZIs. Thus, to enhance ER by cascading two MZIs it is necessary to compensate the alteration which can be achieved by thermally induced phase shift in one of the MZIs.

In Fig.3.7 it is compared modulated normalized transmission of single MZI and cascaded thermo-optic MZIs equipped with spiral- (a, b) and meander- (c, d) shaped microheaters. Enhancement of ER by 9.6 dB as displayed in Fig. 3.7 b) was experienced by spiral-shape microheater MZI and 4.7 dB by meander-shape microheater in Fig. 3.7 d). By applying scanning voltage to one microheater of one of the cascaded MZIs interference pattern of this MZI is thermally shifted in respect to the interference pattern of the second MZI, thus when the interference patterns are perfectly overlapped, ER obtains maximum value.
Important to note that extinction ratio of thermo-optic device with two cascaded MZIs is independent on the shape of the microheater as well as one MZI device since in both cases buffer HSQ layer prevents absorption of the light. However, as was determined in Paragraph 3.3 power consumption of thermo-optic devices with a spiral microheater is less than with a meander type.

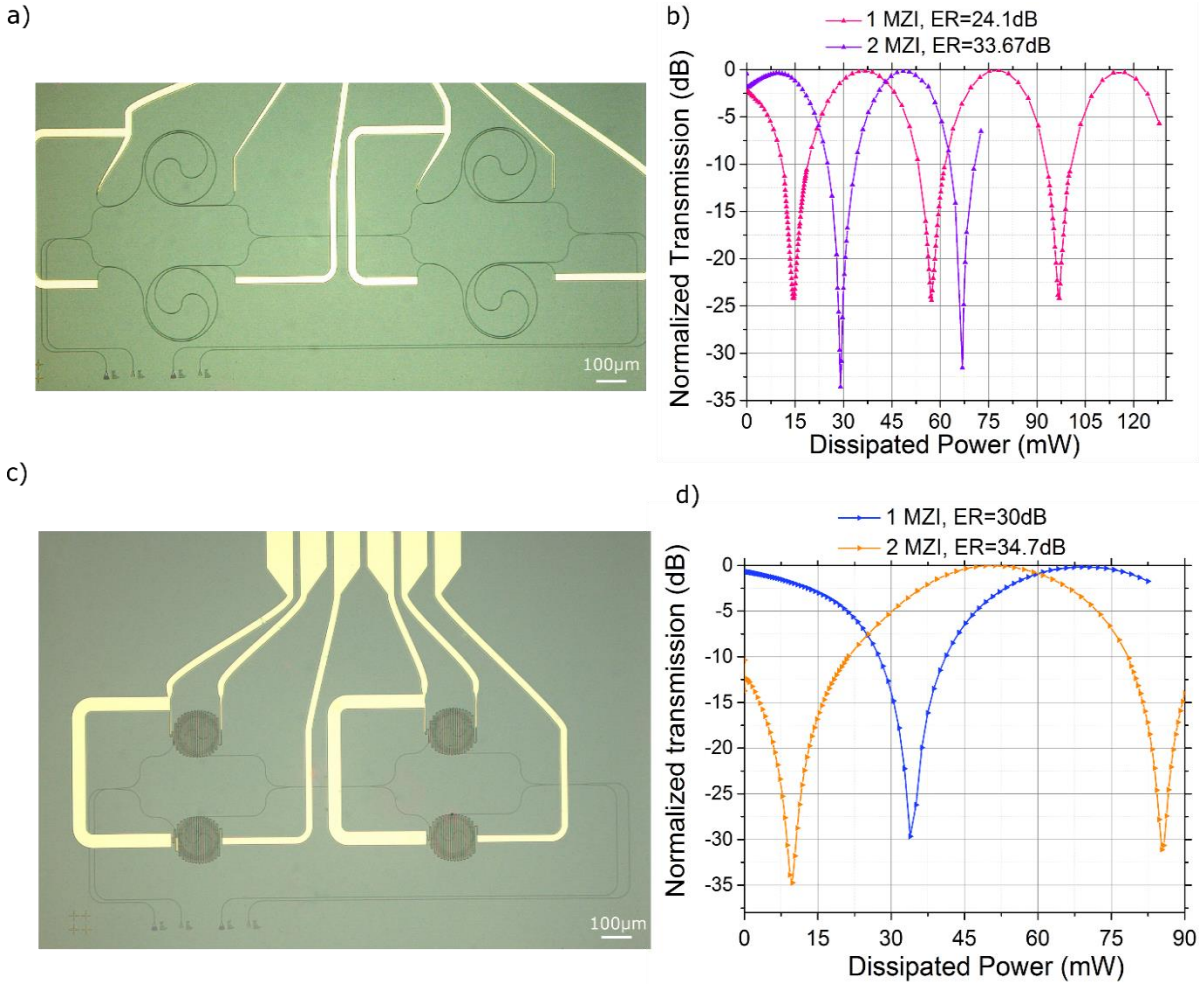

Figure 3.7. Optical micrographs of cascaded thermo-optic MZI devices equipped with **(a)** double-spiral shaped microheater and **(c)** double-meander shape. Comparison of the normalized transmission through a single thermo-optic MZI device and a cascade of two MZIs supplied with a **(b)** double-spiral shaped microheater and **(d)** double-meander shaped. The length of the spiral waveguide in both MZIs is 1.78 mm.

By applying simultaneously two independent scanning electrical voltages to one of the microheaters of the first MZI ('*external*' loop) and one of the microheaters of the second MZI ('*internal*' loop) it was induced corresponding phase shifts in each MZI, thus corresponding interference patterns was overlapped with certain degree depends on the induced phase shift, so modulated intensity at the output of two cascaded MZIs (assuming 50/50 splitting and without counting propagation loss) was determined by me as

$$I_{2\mathrm{MZI}} = \frac{1}{16} * (4 + 4\cos(\Delta\varphi_1) + 4\cos(\Delta\varphi_2) + 2\cos(\Delta\varphi_1 + \Delta\varphi_2) + 2\cos(\Delta\varphi_1 - \Delta\varphi_2)) , \quad (31)$$

where $\Delta\varphi_1$ is the phase difference in the first MZI and $\Delta\varphi_2$ the phase difference in the second MZI, $\Delta\varphi_1$ and $\Delta\varphi_2$ – can be found by (28,29) depends on which arm was heated. Determined analytical modulated transmission is shown in Fig. 3.8 a), whereas measured

normalized transmission at the output of thermo-optic cascaded 2 MZIs device while applying two scanning voltages to one of the microheaters of the first MZI and one of the microheaters of the second MZI simultaneously is displayed in b). It should be noted that the measurement was performed while coupling light on 770nm in the circuit. Theoretical and measured results are in a good agreement, taking in account that dissipated power in the microheater is proportional to $\Delta\varphi$.

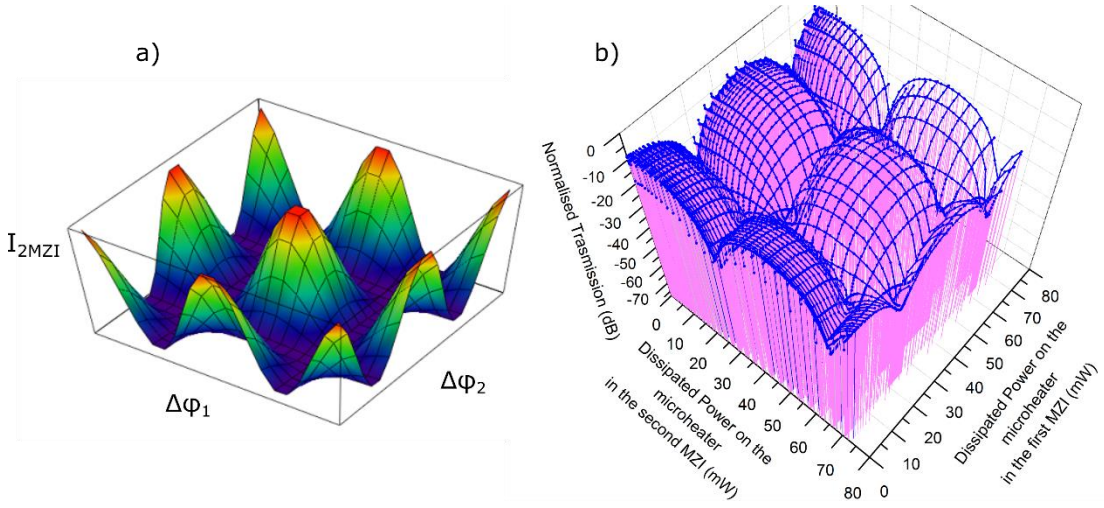

Figure 3.8. a) Analytical modulated intensity at the output of two MZIs as a function of phase difference $\Delta\varphi_1$ and $\Delta\varphi_2$ of the first and second MZI, respectively, according to (31). **b)** Measured normalized transmission of two cascaded spiral-arm MZIs equipped with spiral-shape microheaters (width=1um) by employing a voltage on top one of the arms of first and second MZIs.

3.5 Tuning performance of single and cascaded thermo-optical MZI filters

The goal of the work was to design tunable filter which can be integrated in *hybrid* nanophotonic circuit with coupled single photon emitter to block excitation light and transmit emitted fluorescence light simultaneously. Investigated in Paragraph 3.4 approach, *i.e.* inducing phase shift by thermal heating one of the arms of MZI, allows designing such filter because of the two important features of MZI:

- interference pattern of MZI covers wavelength range from the absorption edge of the material (Si_3N_4) till long-wavelength cutoff,
- free spectral range of interference fringes for different wavelength is different according to (9) from Paragraph 2.1.3.

Therefore, it can be always found a point in the interference patterns, *i.e.* value of applied power to the MZI arm, where one desired wavelength is transmitted at interference maxima and another desired wavelength is suppressed at interference minima.

Designed and fabricated thermo-optic single and cascaded MZIs displayed in Fig.3.1 a) and Fig. 3.7 a) intended to be integrated in hybrid nanophotonic structure with SiV color centers, therefore they should allow to transmit light on around λ=738 nm and cut excitation at around 532 nm. To prove this approach both laser light beams were coupled simultaneously to the device by help of grating couplers.

Firstly, it was considered tunable filter based on single spiral geometry architecture thermo-optic MZI with the lowest power consumption as was shown in Paragraph 3.3, namely with long waveguide arm length L=1.32 mm and narrow spiral-shape microheater – 200nm. To examine the performance, it was applied scanning voltage to one of the arms of MZI, where as a response - modulated transmission in terms of insertion loss of the device is depicted in Fig. 3.9. By applying *P*=33 mW to the microheater on top of long arm of a single MZI passed signal at λ=738 nm (pink curve in Fig. 3.9) obtained maximum – -6.4 dB, whereas inserted loss on λ=532 nm (green curve) amounts 17dB, thus filtration characteristic obtains 10.6 dB.

Interestingly to note, that measured ER of interference pattern on λ=738 nm is higher (ER=19.3 dB) than on 532 nm (ER=7.8 dB), since the waveguide which carries both wavelengths was designed as single mode at λ=738 nm, whereas for propagated light on λ=532 nm such waveguide is not anymore single mode (Fig 3.3 c)), yielding to degradation of interference pattern in terms of decreasing ER.

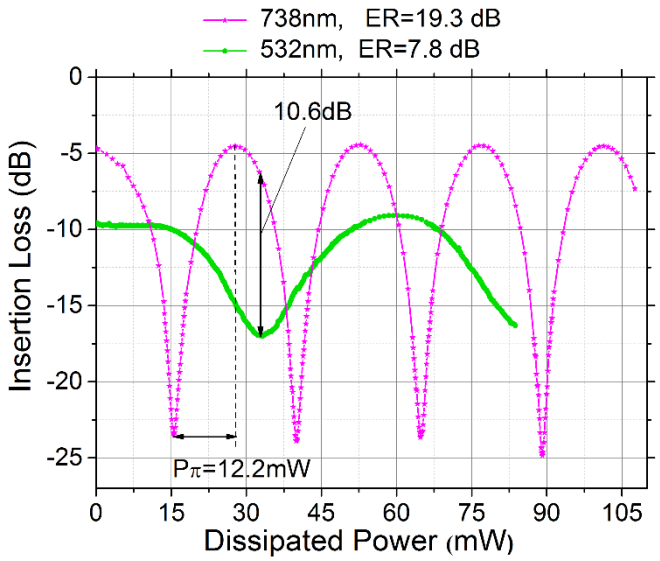

Figure 3.9. Modulated insertion loss a thermo-optic spiral-folded arms single MZI equipped with double-spiral architecture microheater with inner radius of bend 130 um and length = 1.78 mm. Pink curve corresponds to measured transmission at 738 nm, green curve corresponds to measurement performed at 532 nm.

In order to improve filtration characteristic, it was examined cascaded thermo-optic MZIs shown in Fig. 3.7 a), equipped with spiral-shaped microheaters. It was applied two scanning electrical voltage to one of the microheaters of the first MZI and one of the microheaters of the second MZI. Measured modulated transmission of cascaded MZIs in terms of insertion loss as a function of dissipated power on the microheater of first MZI and second MZI while coupling light on λ=738 nm and λ=532 nm is illustrated in Fig. 3.10 a) and b). Maximum filtration characteristics is achieved in the point where there is maximum transmission on λ=738 nm, while light at λ=532 nm is blocked, *i.e.* transmission is minimal. These requirements are satisfied when the dissipated electrical power on the long arm on the first MZI amounts as 40 mW and of the second MZI is 43 mW, which correspond to inserted loss at λ=532 nm a of 30 dB which is higher than in case of single MZI and transmission at λ=738 nm of -10 dB. As a result, in this case obtained filtration depth is 20 dB which exceeds 10 dB that of a single MZI.

ER of considered device with spiral-shape microheaters on λ=738 nm is 32.9 dB which is 13.6 dB higher than in case of the same geometry single MZI (pink curve on Fig 3.9). In case of coupling light at λ=532 nm maximum obtained value of ER is 11.35 dB, above 3.55 dB than in single MZI (green curve on Fig 3.9).

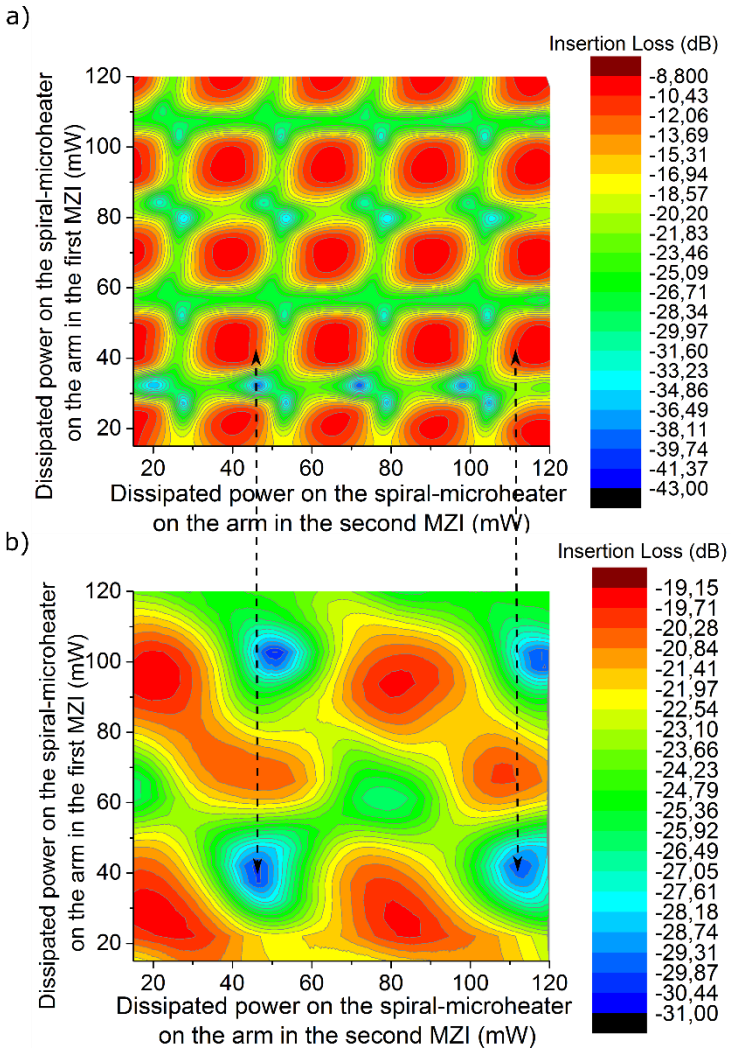

Figure 3.10. Transmission of two cascaded thermo-optic MZIs equipped with spiral-shaped microheaters as a function of dissipated power by employing a voltage to the microheaters on top of one of the arms of the first and second MZIs. **a)** The contour graph shows transmission at 738 nm, ER=32.9 dB. **b)** Contour graph displays transmission at 532 nm, ER=11.35 dB. Parameters of MZI: width of heater 200 nm, minimum radius of spiral-folded waveguide 130 um.

3.6 Concluding remarks

It was designed, fabricated and measured low-loss thermo-optic single MZIs and two cascaded MZIs equipped with spiral and meander shaped microheaters based on a silicon nitride-on-insulator platform, which function as integrated on chip tunable filters in the visible range to simultaneously transmit light at desired λ=738 nm and cut light at another desired λ=532 nm, which corresponds fluorescence and pump light of ZPL of SiV, respectively. Minimal measured insertion loss including propagation loss in the waveguides and loss in both branches amounts 4.2 dB for thermo-optic MZI equipped with spiral shaped microheater. It was explored approaches to decrease switching power of single thermo-optic MZI with a spiral-folded waveguides in both branches; in particular it was considered spiral and meander geometry architecture of microheaters where the first one showed lower switching power because of more efficient heating. To further economy power consumption the width of microheaters and length of active (heated) waveguide was varied, and eventually it was determined in the experiment that longer spiral-folded waveguide and narrower width of microheater are beneficial to use. Thus, minimum measured switching power P_π=12.2 mW obtained for a single thermo-optic MZI with spiral-shape microheater which was aligned with beneath Si_3N_4 waveguide, where the width of microheater was 200 nm, which equals roughly half of the rib waveguide width, whereas length of spiral-arm was 1.78 mm for thickness of the SiO_2 top cladding layer (between microheater and waveguide) equal to 0.85-1 μm. This value compares favourably to previous results [81][84][85] taking into account low thermo-optic coefficient for silicon nitride ($\frac{dn}{dT} \sim 10^{-5}\ K^{-1}$, about ten times lower than in silicon). Designed, fabricated and measured on-chip single MZIs with spiral-shaped microheaters showed a maximum ER=25 dB which is higher than in reported before articles [81][85][86].
To improve filtration depth of thermo-optic MZI it was designed and fabricated cascaded two MZIs device which demonstrated maximum value ER=34.7-36.5 dB regardless the shape of microheater since optical mode was isolated from absorption loss in metal microheaters by sufficient thickness of buffer HSQ layer.

The novel design with double microheaters on top of both arms of single and cascaded MZIs allows to double the range of the shifting amplitude of the interference fringes namely interference fringes can be blue- or red-shifted depends on to which branch of MZI was applied voltage.

Finally, it was demonstrated possibility to use such low power consumption thermo-optic filter as a tunable filter to pass light on λ=738 nm within a bandwidth=10.5 nm and suppress λ=532 nm with filtration depth of 10.44 dB and 21.5 dB, respectively for single and double cascaded thermo-optic MZIs. Moreover, demonstrated architecture tunable filters are multifunctional, namely allowing to transmit and block desired wavelengths in the wide wavel ength range for future applications in hybrid nanophotonic circuits.

In order to increase further filtration depth of such cascaded filter it is necessary to optimize further splitter/combiner parameters and cascade more than two stages of filters, at the same time insuring overall low insertion loss of the device, which will make possible to integrate such filter into the *hybrid* circuit with single-photon emitter.

4. Double apodized single Bragg grating filter on-chip

Motivation

One of the requirements which should be satisfied to build all integrated *hybrid* photonic circuit with coupled single photon emitter is the necessity to block excitation light. In the Chapter 3 it was demonstrated Cascaded tunable MZI filter on-chip, which ensures maximum and minimum transmission on desired wavelengths in the visible region. In particular, integrated optical filters were realized for use in combination with an emission sources at around 738 nm and 532 nm, which should be transmitted and blocked, respectively. These wavelengths correspond to ZPL of SiV fluorescence and excitation light, respectively, thus making possible to integrate cascaded MZI filters in hybrid circuit with coupled SiV. However, working principle (thermo-optic effect) of developed MZI filters requires applying voltage to the microheaters, which was equipped each arm of MZI, to provide tunability, which will be quite challenging to use in experiments at cryogenic temperature. Insertion loss of such filters amounts 4.2 dB per stage. Also, fabrication of these filters on-chip required three steps of electron beam lithography.
Therefore, the aim of the next step of the work was to engineer scalable passive optical filter, which does not require electric control in case of cascading several stages of filters, and so which can be employed at cryogenic temperatures, and can be fabricated in single lithography step. The Bragg grating filters are widely used in fiber-optic communication systems to achieve in particular wavelength-selection and dispersion compensation [96]. Integrated Bragg gratings on silicon-on-insulator (SOI) platform are employed as filters, wavelength division multiplexors, sensors, [99][100][101][102].
Waveguide integrated low loss Bragg grating filter in the visible wavelength region based on silicon nitride on insulator platform on-chip, satisfies the requirements reported above, and was investigated in this thesis.

4.1 Single Non-uniform Bragg grating filter

Bragg grating structure is the waveguide with sidewall corrugations, where the guided optical mode experiences periodic modulation of effective refractive index in the propagation direction, as shown in Fig. 4.1 b), c). The physical mechanism of Bragg filter based on multiple and distributed reflections of light on each corrugation while propagation of light through grating, where the reflections interfere constructively only in narrow band centered at one particular wavelength, *i.e.* Bragg wavelength $\lambda_{Br} = 2\Lambda n_{eff}$, where Λ – period of the grating. Thus, this wavelength range is strongly reflected, while the light at the wavelength range out of that

spectrum transmits through the grating (ideally without scattering), due to destructive interference of multiple reflections of this light in the backward direction.

It was designed and fabricated single Bragg grating with variation of parameters to maximize filtration depth and minimize insertion loss. Scalable matrixes of photonic devices including Bragg filters were realized on the chip consisting of 200 nm Si_3N_4 on top of 2000 nm SiO_2 on top of silicon and on another chip which consists of 150 nm Si_3N_4 on top of 500μm SiO_2. Fabrication of the nanophotonic circuits based on single step of electron-beam lithography followed by half-etching of silicon nitride layer (for chip which consisted 200nm Si3N4) and fully-etching of silicon nitride (for chip which consisted 150 nm thickness of Si_3N_4) via reactive ion etching as was discussed in Paragraph 3.2.

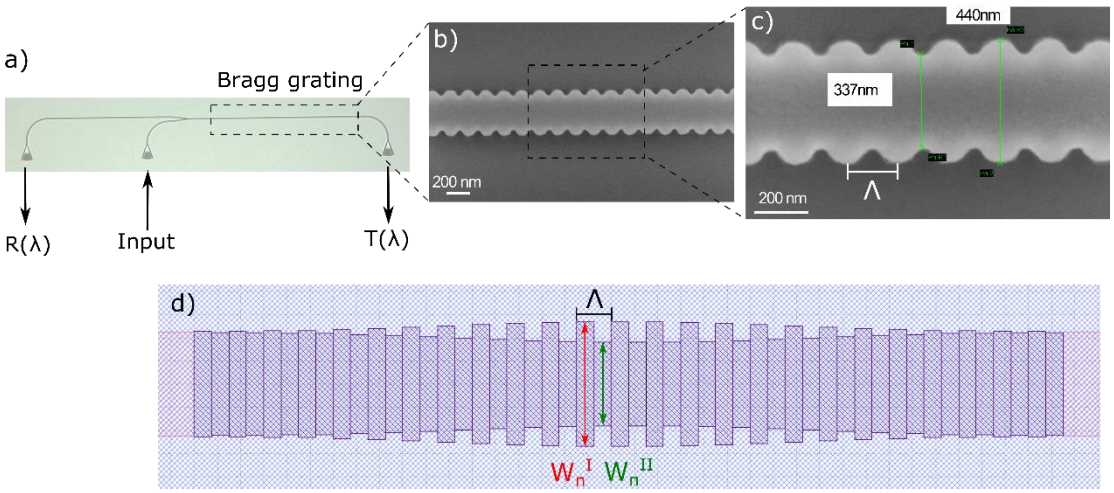

Figure 4.1. a) Optical micrograph of fabricated photonic device which consists of Bragg grating filter in Si_3N_4 on chip. **b)** SEM image of part of Bragg grating with zoom-in on **(c). d)** Schematic design of filter with labeled period Λ and width of segment I and II, respectively W_n^I, W_n^{II}. Realized grating on b) and c) was smoothed due to fabrication.

Non-uniform Bragg grating filters, *i.e.* with complex profile of corrugation of sidewalls, achieve higher filtration depth with the same number of periods, due to suppression of reflection side-lobs.

Therefore, Bragg filters with Gaussian attenuation of corrugation were designed (shown in Fig. 4.1), investigated and discussed in this Chapter. The *novelty* of the developed reflectors is *double* Gaussian *inside* and *outside* envelope of the corrugation of sidewalls. Namely, the period is divided in two equal segments (I and II), where the width of the first segment (I) increases as

$$W_n^I = W_{n-1}^I + 2 * A * e^{-b*\left(\frac{n - N/2}{N}\right)^2}, \qquad (33)$$

whereas the width of the second segment (II) decreases as

$$W_n^{II} = W_{n-1}^{II} - 2 * A * e^{-b*\left(\frac{n - N/2}{N}\right)^2}, \qquad (34)$$

where n – numerator of current period, $n = 0, \dots N$; N – number of periods; A – amplitude of the envelope; W_{n-1}^{I} , W_{n-1}^{II} – width of the period $n-1$ for the I and II segments, respectively. Coefficient b was defined as a function of A to provide smooth transition of waveguide into grating part, to ensure smooth coupling of grating (Bloch) mode into guided mode, in order to suppress scattering loss. Thus, b was calculated from the requirement to have the first corrugation equals 1nm, so for $n = 0$: $A * e^{-b*\left(\frac{n - N/2}{N}\right)^2} = 1$, thus $b = \frac{\ln(A)}{0.25}$.

Thus, measured Reflection and Transmission spectrum of Bragg grating with double Gaussian apodization according to (33, 34) are shown in Fig. 4.2. Measurement was performed by coupling supercontinuum light from white light source via input grating coupler, whereas reflected and transmitted light was collected via another two grating couplers, as depicted in Fig. 4.1 a). Normalized measured Transmission and Reflection spectra are shown in Fig. 4.2.

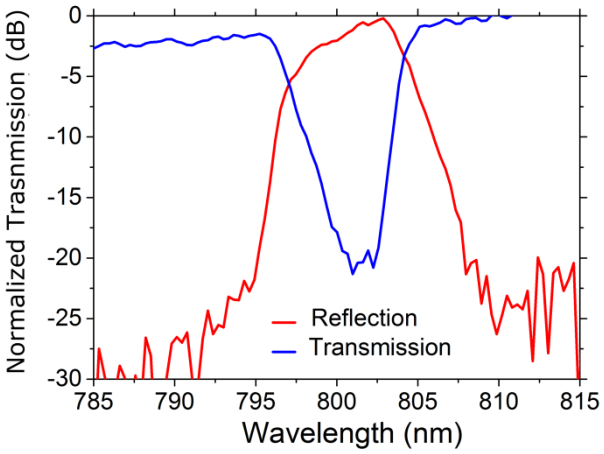

Figure 4.2. Measured normalized Reflection (red curve) and Transmission (blue curve) spectrum of non-uniform Bragg grating with double Gaussian apodization with 1700 periods ($N = 1700$), $\Lambda = 260nm$, $A = 220nm$ on silicon nitride-on-insulator. Waveguide thickness 150nm.

Thus, this Bragg filter provides filtration depth up to 21dB with 3-dB bandwidth of 5.61nm.

4.2 Experimental investigation and optimization

The dependencies of the main parameters of non-uniform Bragg filter, such as filtration depth, bandwidth and central wavelength, on geometrical parameters of the grating, which was verified in the measurements, are investigated in this Paragraph.

Period variation

Scale-up the period leads to considerable red-shift of central wavelength according to Bragg condition $\lambda_{Bragg} = 2 * n_{eff}\Lambda$. This was observed experimentally and shown in Fig. 4.3, the rate of tuning is $\frac{\delta\lambda_{Bragg}}{\delta\Lambda} = 2.5$. The average filtration depth obtains 20-21dB, whereas average 3-dB bandwidth is 6.75nm, the average optical loss inserted by filter in the reflected light is 4.1dB.

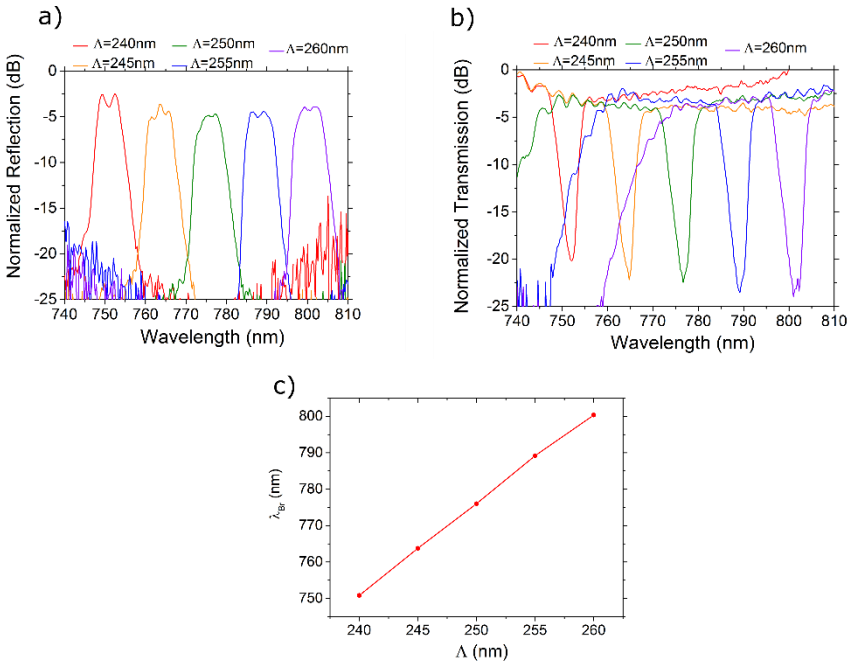

Figure 4.3. Measured Normalized Reflection **(a)** and Transmission **(b)** spectra of non-uniform double Gaussian apodized Bragg grating filters on-chip with varied period Λ with number of periods $N = 1500$ and A=210nm. **c)** Measured dependency of Bragg wavelength versus period Λ. Waveguide thickness 150 nm.

Corrugation amplitude (A) variation

Increase of corrugation amplitude A leads to rise of coupling coefficient of the grating [103], yielding in wider bandwidth of the reflected spectrum and higher filtration depth, it was verified in measurements and shown in Fig. 4.4. Furthermore, with increasing corrugation effective refractive index slightly rise for considered double apodized grating, therefore, according to Bragg's law Bragg wavelength growth with measured rate $\frac{\delta\lambda_{Bragg}}{\delta A} = 0.03$.

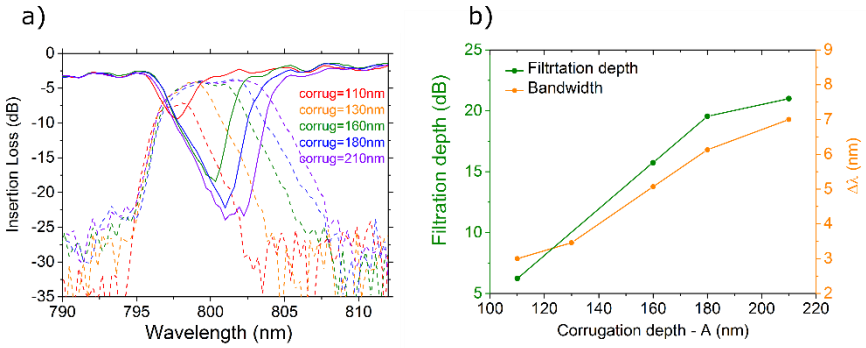

Figure 4.4. Measured Normalized Transmission (solid curves) **(a)** and Reflection (dashed curves) **(b)** spectra of non-uniform double Gaussian apodized Bragg grating filters on-chip with varied corrugation amplitude A, grating consists $N = 1500$. **c)** Measured filtration depth and 3-dB bandwidth versus corrugation amplitude A. Waveguide thickness 150nm.

Number of periods variation

Non-uniform Bragg grating filters with single outside (33), inside (34) and double Gaussian (33 and 34) envelopes were investigated via measurements. With increasing number of periods N bandwidth of the reflected spectrum decreases and filtration depth rise. At certain N extinction ratio (ER) of reflected signal will saturate, since it will be limited only by radiation loss, analogous to photonic crystal investigated in Chapter 5. Saturation number of periods was determined for three types of gratings and shown in Fig. 4.5. As can be seen, saturation number of periods of Bragg filter with single outside or inside envelope is $N_{sat} > 2500$, while at $N = 2500$ 3-dB bandwidth achieved 2 and 2.6 nm; ER=25 dB and ER=23 dB, respectively. Bragg filter with double apodization decreases saturation number in almost five times, thus $N_{sat} \approx 700$ with 3-dB bandwidth 2.9 nm and ER=25.1 dB. Obviously, less number of periods in the grating is beneficial in terms of low insertion loss, due to uncontrolled scattering on fabrication imperfections, and compaction of photonic device.

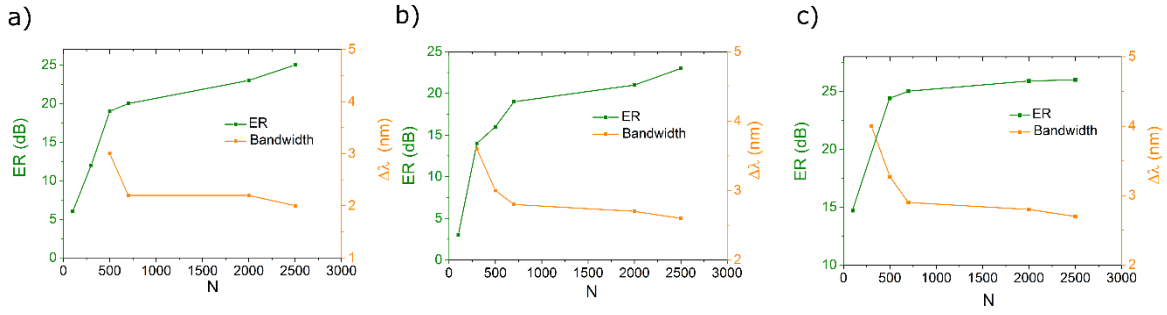

Figure 4.5. Measured Extinction ratio of Reflected signal and 3-dB bandwidth versus number of periods N of non-uniform Bragg grating filter with single outside **(a)** and inside **(b)** Gaussian apodization and with double Gaussian apodization **(c)**. Parameters of the filter: $\Lambda = 220\ nm$, waveguide thickness 200 nm.

4.3 Conclusion and Outlook on a contra-directional Bragg grating filter

The Non-uniform Gaussian apodized Bragg filters on silicon nitride-on-insulator on chip were designed and fabricated in single lithography step. Bragg filters produce non-repetitive response in comparison with MZI. Furthermore, bandwidth of stopband and filtration depth can be controlled by the shape and parameters of sidewall corrugation as was demonstrated in this Chapter. *Novel* double apodized single Bragg filter on chip was developed, which obtains up to 21dB filtration depth with 3-dB bandwidth 5.5-7 nm, which consists far fewer periods in comparison with single-apodized Bragg filter. Averaged insertion loss in reflected light of one filter is 4.1 dB. Tunability of Bragg wavelength is ensured by changing the period of the grating. All this makes Bragg filter the good candidate to be integrated in *hybrid* nanophotonic circuit in order to block excitation light.

Outlook on Bragg filter based on contra-directional coupler

Single-photon experiments, however, require higher filtration depth, which, in general, can be achieved by cascading single Bragg filter to enhance extinction ratio of reflected light, but this will lead to rise of insertion loss. Therefore, it was fabricated and investigated contra-directional Bragg grating filter on silicon nitride-on-insulator platform, analogous as was reported, in particular on SOI also in [104][105][106][107][108][109][110][111][111][112]. Such filters can be cascaded to enhance filtration depth insuring zero insertion loss. As well as for single Bragg filter considered in this chapter, double Gaussian apodization of both gratings allowed to maximize filtration depth also in case of contra-directional grating filter. Thus, one double Gaussian apodized Bragg filter based on contra-directional Bragg grating on Si_3N_4 provides 21dB filtration depth. Further optimization is required to obtain negligible insertion loss to cascade several stages of such Bragg filter in order to increase filtration depth, which allows to integrate such filters for applications into photonic circuits.

5. Freestanding cross-bar Photonic crystal cavity

Photonic crystal cavity (further PhC cavity) is a perfect candidate to be integrated in nanophotonic circuit on-chip to enhance emission line of single photon emitter coupled into resonance mode, where the source should be placed into cavity region, resulting in rise of on-resonance coupling efficiency due to Purcell enhancement. PhC cavity provides high Quality factor of the resonance modes, where resonance wavelength can be precisely tuned in nanometer-scale by variation of geometry parameters of the photonic crystal. Explored in the current work PhC cavity is based on the waveguide and cross-bar structure with drilled holes, therefore can be naturally further integrated in the nanophotonic circuit. A *novel* 1D freestanding *cross-bar PhC cavity* allows to evanescently couple single photon emitter placed on top of the cavity, where enhanced emitted light is coupled out through waveguide which consists PhC cavity, while direct excitation of the source is provided through crossed waveguide.

The first part of work was dedicated to the design of PhC cavity, which was performed via simulations. In particular, PhC modulated mirror was built based on numerically computed Band diagram with the bandgap in the interested wavelength region (*Paragraph 5.1.1*). Determined Bragg mirrors were further employed as PhC mirrors positioned from both sides of the cavity in nanobeam and cross-bar PhC devices. The second part of work was dedicated to optimization parameters of PhC cavity, to obtain high Q resonance modes on required wavelength, which was verified via simulations and measurements, which were found in excellent *agreement (Paragraph 5.1.2).* The influence of tuning geometrical PhC parameters on the main characteristics of the cavity (Q-factor and resonance wavelength) was numerically and experimentally investigated in *(Paragraph 5.1.3).*

Full experimental and via simulations characterization of fabricated optimized freestanding cross-bar PhC cavity on chip is shown in *Paragraph 5.2*. To obtain maximum Purcell enhancement optimized position of the source on the cavity region was precisely defined via performed simulations of Local Density of States enhancement, corresponding spatial enhancement map was built *(Paragraph 5.2.2).* Precise positioning of single photon source is still challenging, thus, such enhancement map allows to evaluate enhancement of the source placed in any position on the cavity region, which can be determined by help of SEM or/and AFM in the experiment.

The main figure of merit for an emitter coupled to a cavity is transmission coupling efficiency into cavity (β-factor), which was determined via sets of simulations for investigated cross-bar PhC cavity *(Paragraph 5.2.3).* The main achieved results and Outlook on the future work are discussed in *Paragraph 5.3*.

5.1 Engineering freestanding cross-bar PhC cavity

PhC cavity consists of two PhC (Bragg mirrors) where in between it is introduced cavity region where in subsequent experiments the source can be positioned, the sketch of the device is shown in Fig. 5.1. Thus, engineering of PhC cavity device starts with determination through several sets of simulations of Bragg mirror's parameters, which can trap the light in between longer-better to assure high Quality factor of PhC cavity and at the same time provide low radiation loss, which can be achieved by modulation refractive index of the segments.

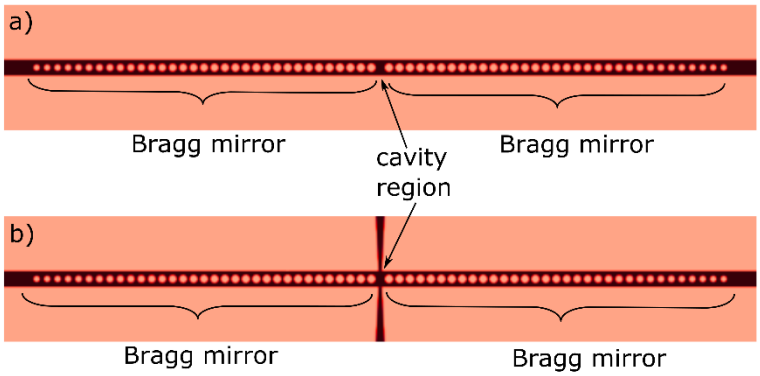

Figure 5.1. Top view of freestanding nanobeam **(a)** and cross-bar PhC **(b)** cavity computed using free and open-source MEEP software [92].

When the parameters of Bragg mirrors were fixed, the next round of simulations was performed, namely the computation of the entire PhC cavity device with introduced cavity region to determine electric field distribution of resonance modes and their Quality factor (further Q-factor). By tuning the parameters of the geometry, especially cavity length, Q-factor can be maximized, whereas by changing periodicity of the segments target resonance wavelength can be obtained. Simulation results were verified by transmission measurements of fabricated PhC cavities.

5.1.1 Investigation of Modulated Photonic crystal (Bragg mirror)

The goal of the first step of computation of Photonic crystal (PhC) cavity was to build PhC mirror (Bragg mirror) with the bandgap in the required frequency region, where further by introducing the defect, *i.e.* increasing spacing between two central holes, the mode will be pulled down into the bandgap yielding into TE-like resonance mode on target wavelength. In order to decrease radiation loss in such PhC cavity filling fraction of segments from both sides of cavity should be modulated, namely quadratic interpolated according to the following expression:

$$ff(n) = ff_f - \frac{ff_f - ff_l}{(N-1)^2}(n-1)^2, \qquad (32)$$

where ff_f – filling fraction of the first (inner) segment, ff_l – filling fraction of the last (outer) segment, n – count number of segment, N – total number of mirror segments (periods). Thus, more specifically, the first aim was to determine filling fraction of the inner and outer segments with bandgaps overlapping in the interested frequency region. Target frequency of resonant modes were 738 nm which corresponds to ZPL of SiV (topic of Chapter 1) and 785 nm corresponds to ZPL of DBT molecule (subject of Paragraph 2.3 and Chapter 6).

Choice of parameters of the photonic crystal (Bragg mirror)

Thickness of waveguide was pre-determined by the choice of the conventional silicon nitride-on-insulator wafer with 200 nm thick layer of Si_3N_4. Width of the waveguide was set 450 nm to confine single fundamental transverse-electrical (TE0) mode in the wavelength range of interest in the waveguide according to performed simulation in COMSOL (topic of Paragraph 2.1.1) in order to prevent degradation of Quality factor as a result of multimode dispersion, at the same time the width of the waveguide was large enough to pull the resonance mode away from the light cone.

Period a of drilled holes was estimated according to Bragg's law [45] as $a = {\lambda_0}/{2n_{eff}}$, where n_{eff} – effective refractive index of the mode, $n_{eff} = 1.546$ on $\lambda = 738\,nm$ of freestanding waveguide corresponds to ZPL of SiV.

The goal was to engineer PhC cavity, where antinodes of the major electric field component (further E_y) is in the cavity region (in Si_3N_4), to enhance emission of single photon emitter positioned on top of the cavity in further experiment. This type of cavity called *Dielectric* in contrast with *air type*, where electric field is concentrated in the material with lower refractive index, *i.e.* in air holes. In both cases mirror strength γ [55] of the inner hole ff_f should equal zero, while mirror strength of the outer hole ff_l should achieve maximum possible value.

According to Bloch-Floquent theory considered in Paragraph 2.1.4 it is sufficient to consider single segment of 1D periodic PhC, *i.e.* to determine bandgap for one cell, which can be allocated to the uniform photonic crystal with infinite number of such periods.

To determine geometric parameters of modulated periodic PhC (Bragg mirror), which yields in the highest mirror strength for the last segment and zero mirror strength for the inner segment, it was studied cells with different periodicity and with variation of filling fractions ff using *free open-source MPB software [93]*. Computed mirror strength for sweep of parameters while keeping wavelength constant 738nm and 785nm, respectively shown in Fig. 5.2 a),b).

For the target wavelength $\lambda = 738\,nm$ uniform PhC with periodicity $a = 300\,nm$ (dark blue curve in Fig. 5.2 a) provides highest mirror strength γ =0.087. Dielectric PhC cavity can be originated by quadratic interpolation filling fraction between $ff_l = 0.29$ for the last segment (diameter of corresponding hole is 227nm) and $ff_f = 0.44$ (diameter of corresponding hole is 280nm), thus the distance between two central closest holes (n = 1 and n = 2) is ≈ 30nm.

For the target wavelength $\lambda = 785\,nm$ PhC with periodicity $a = 330\,nm$ (dark blue curve on Fig.5.2 b) provides highest mirror strength γ =0.0858. In this case dielectric type PhC cavity can be originated by quadratic interpolation filling fraction between $ff_l = 0.28$ (diameter of corresponding hole is 230.2 nm) and $ff_f = 0.44$, (diameter of corresponding hole is 288.5nm), thus the distance between two closest central holes is ≈ 41nm.

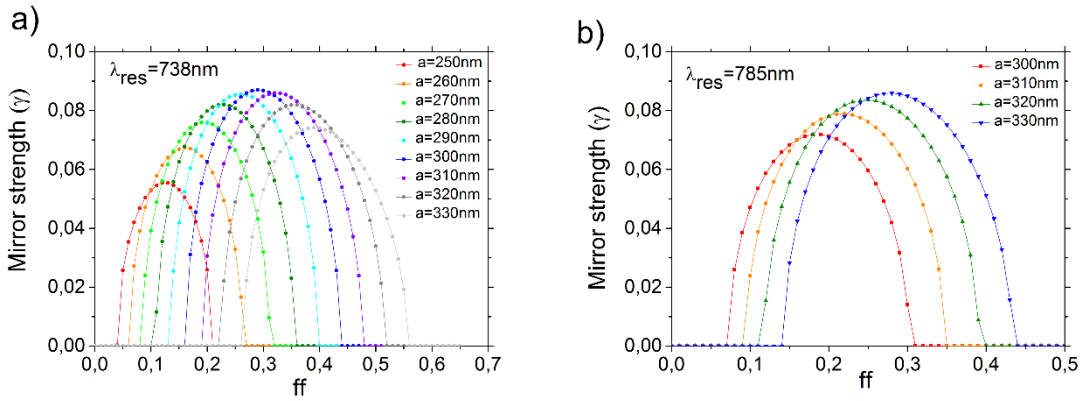

Figure 5.2. Computed Mirror Strength as a function of filling fraction of the segment for variation of PhC periodicity a (indicated in the legend) for resonance wavelength $\lambda = 738\,nm$ **(a)** and $\lambda = 785\,nm$ **(b)**.

Due to fabrication limitations devices, where the distance between holes is less than 50nm, will potentially have lower Quality factor, due to not round shape of the holes, and in the worst case, even connection between holes. Therefore, from fabrication point of view radius of holes should be decreased or/and periodicity increased.

Scaling up the period of PhC while keeping other parameters constant as shown in Fig. 5.2 or scaling down ff_f and ff_l (Fig. 5.3) leads to the shift of resonance wavelength of PhC cavity in the longer wavelength range, according to Bragg's law. Colorful curves in

Fig. 5.3 indicate mirror strength as a function of filling fraction of the cell for variation of resonance wavelengths (730-790 nm), period of PhC was set 300 nm. Thus, dielectric PhC cavity with period 300 nm, which provides resonance wavelength at 785 nm, can be formed by two modulated Bragg mirrors with quadratic envelope of filling fraction between $ff_f = 0.30$, corresponding to the first segment, and $ff_l = 0.16$, corresponding to the last segment, where each mirror consists of N periods; in this case minimal distance between two biggest neighbor holes is 73 nm, which can be resolved during fabrication.

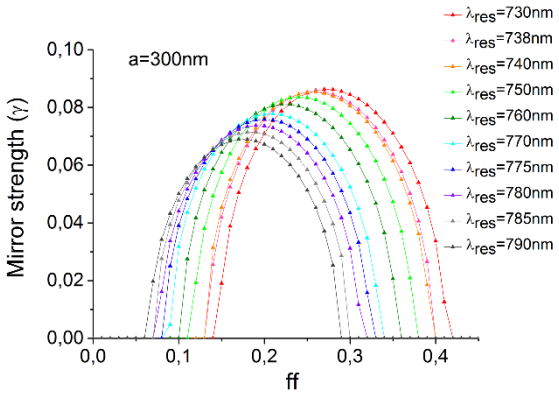

Figure 5.3. Computed Mirror Strength as a function of filling fraction of the segment for variation of PhC resonance wavelength (indicated in the legend) for photonic crystal with period $a = 300\ nm$.

To decrease radiation loss in PhC cavity it is necessary to engineer Gaussian profile of the electric field of resonance mode as was verified in [94], which was achieved by quadratic interpolation of filling fraction of the segments (Fig. 5.4 c)) according to [55], yielding to linear dependence between mirror strength and the index of the segment in PhC cavity, which is evident in Fig. 5.4 b).

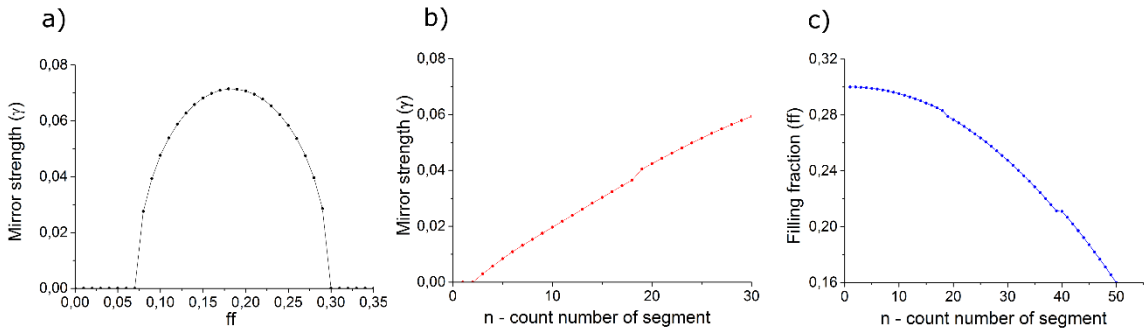

Figure 5.4. a) Mirror strength as a function of filling fraction for PhC with a=300 nm, target $\lambda_{res} = 785 nm$. Mirror strength **(b)** and filling fraction **(c)** versus the index number of the segment in PhC.

Thus, in order to hit target resonance wavelength 732 nm and 785 nm, it was designed and fabricated PhC cavities with variation of parameters, in particular filling fraction and period; as it will be shown in the next Paragraph 5.1.2, PhC cavity device with modulated Bragg

mirrors from both sides of cavity with $a = 300nm$, $ff_f = 0.30$ and $ff_l = 0.16$ achieves highest Quality factor.

Simulation Band diagram of the photonic crystal (Bragg mirror)

Simulated using free open-source MPB software [93] TE-like band diagram of designed and further fabricated freestanding modulated PhC crystal by employing several steps of electron-beam lithography (subject of *Supporting Information*) shown in Fig. 5.5 a), as it was highlighted before it was sufficient to simulate one computational cell, the solution can be extended for full Bragg mirror with infinite number of segments. Band diagram depicted in Fig. 5.5 a) can be interpreted in the following way.

It is shown dielectric (solid curves) and air (dashed curves) bands for respective uniform photonic crystals (Bragg mirrors), formed with infinite number of identical segments with filling fraction $ff_f = 0.30$ and $ff_l = 0.16$, respectively. In other words, Bragg mirror with infinite number of identical periods with $ff = 0.30$ reflects wavelength range formed by respective bandgap, established between two red curves b_1 , b_2.

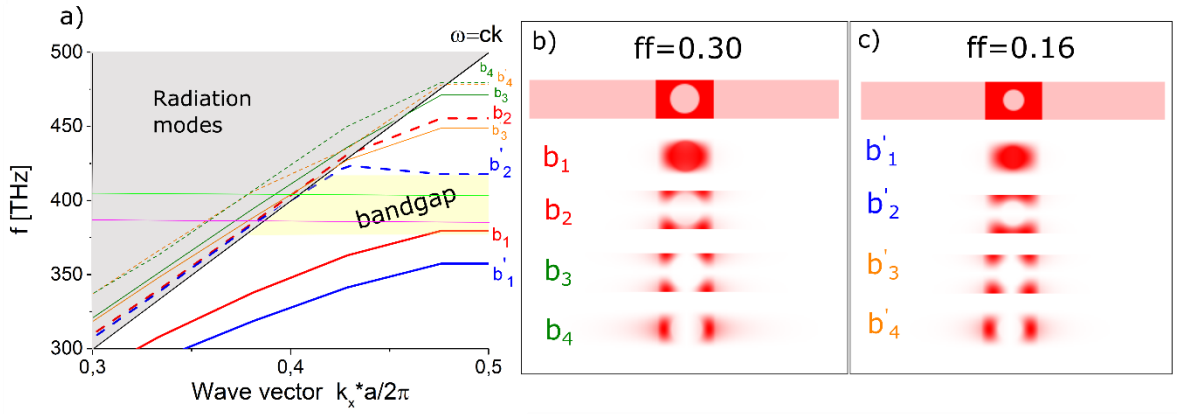

Figure 5.5. TE-like polarized band diagram of freestanding PhC. **a)** Band diagram inside first irreducible Brillouin Zone of uniform PhCs with periodicity a=300 nm with segments $ff_f = 0.30$ *and* $ff_l = 0.16$*, respectively, with corresponding TE-like bandgaps – between red curves* (b_1, b_2) *and between blue curves* (b_1', b_2')*, respectively. This band diagram, at the same time, displays* TE-like *bandgap of modulated PhC with inner segment* $ff_f = 0.30$ and outer segment $ff_l = 0.16$, which is in the overlapped yellow shade region. Solid blue and red curves corresponds to dielectric modes, while dashed curves - to air modes of corresponding PhC. The Light line is shown in black $\omega = ck$. Horizontal light green and pink lines show desired resonance wavelengths 738 nm (406.6 THz) and 785 nm (382.1 THz), respectively.

Freestanding PhC parameters: width=450 nm, height=200 nm. On b) and c) it is shown cross-section (z=0 plane) of time-averaged magnetic field energy density at the Brillouin-zone edge $k = \pi/a$ of the dielectric (b_1, b_1'), air (b_2, b_2') and higher-order (b_3, b_3', b_4, b_4') modes, respectively for inner $ff_f = 0.30$ **(b)** *and outer* $ff_l = 0.16$ **(c)** segments of photonic crystal.

Whereas, uniform photonic crystal with infinite number of identical segments with $ff = 0.16$ reflects *wavelength range,* formed by respective bandgap established between two blue curves b_1' , b_2'. Thus, modulated photonic crystal (modulated Bragg mirror), constructed by segments with quadratic interpolated filling fractions between $ff_f = 0.30$ and $ff_l = 0.16$, has a bandgap (yellow region) in the overlap region between bandgaps for considered uniform PhCs with ff_f and ff_l segments, respectively. The results are summed up in Table 1. This region corresponds to the range 717-791 nm, which satisfied required frequency range with target frequencies: 738 nm (ZPL of SiV) and 785 nm (ZPL of DBT molecule). Thus, red solid curve b_1 - *dielectric band edge* and dashed curve b_2' – *air band edge* form bandgap of dielectric type modulated PhC.

Dielectric edge modes (b_1, b_1') of PhC are characterized by electric field of the mode concentrated in higher index material, whereas magnetic field of these mode have maximum in lower index material (in the hole). Air edge modes (b_2, b_2') experience the opposite behavior as shown in Fig.5.5 b), c).

PhC mirror type	First (inner) segment	Last (outer) segment	Bandgap in frequency range	Bandgap in wavelength range
uniform	$ff = 0.30$	$ff = 0.30$	379-455 THz	659-791 nm
uniform	$ff = 0.16$	$ff = 0.16$	357-418 THz	717-840 nm
modulated	$ff_f = 0.30$	$ff_l = 0.16$	357-455 THz	717-791 nm

Table 1. PhC mirrors (Bragg mirrors) with corresponding simulated bandgaps.

5.1.2 Simulation of nanobeam and cross-bar PhC with internal cavity

The goal was to engineer wavelength-scale cross-bar PhC cavity which can be integrated with other photonic devices on chip to couple single photon emitter and enhance its spontaneous emission rate, where resonant wavelength of PhC cavity should match emission line of the source.

A *novel* 1D freestanding *cross-bar PhC cavity* designed, simulated and fabricated in the thesis (Fig. 5.6) allows to evanescently couple single photon emitter placed on top of cavity, where enhanced emitted light will be coupled out through waveguide which consists PhC cavity, while direct illumination of the source is provided through crossed waveguide. Thus, spatial separation of excitation and emitted light is ensured. Spontaneously emitted fluorescence light coupled into resonance mode will be trapped inside the cavity and enhanced due to Purcell effect.

Crossed waveguide is tapered in order to suppress amount of pump light, which can be leaked inside PhC, *i.e.* decrease crosstalk, and at the same time to reduce influence of cross-bar on

Quality factor of resonance modes, especially on odd modes, as it is shown further in this paragraph.

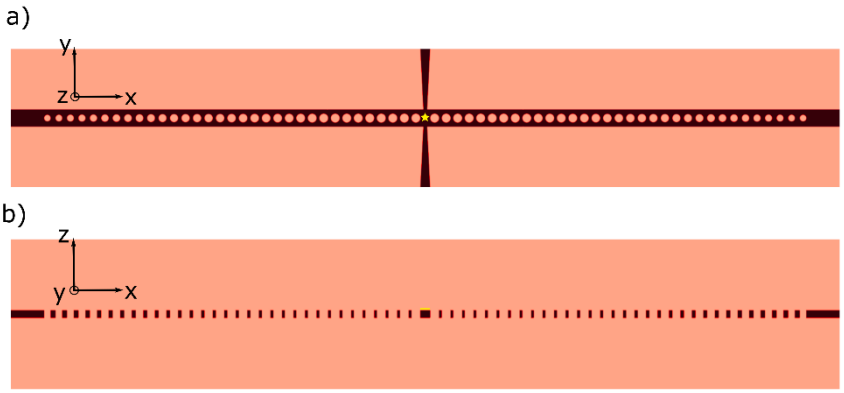

Figure 5.6. Schematic of freestanding cross-bar PhC cavity with evanescently coupled emitter (yellow star), placed on top of cavity region in xy plane **(a)** and xz plane shown on **(b).** These sketches obtained as an output of performed simulations using free open-source software MEEP.

Proposed cross-bar PhC cavity preferably carries TE-like polarized resonant modes inside TE-like bandgap examined in previous Paragraph 5.1.1.

For efficient coupling fluorescence light from single photon emitter to the PhC cavity main requirements should be satisfied:

- emitter should be positioned at the antinode of electric field of the wavelength-matched resonance mode of the cavity;
- polarization of emitted light should be aligned with the polarization of wavelength-matched resonance mode of the cavity (TE-like resonance mode with a major field E_y). However, in the experiment it is challenging to position emitter in the required place, therefore it is difficult to pre-define polarization of the emitter.
- Linewidth of resonance peak of cavity should be wider than transition linewidth of spontaneously emitted light.

It should be noted that it was designed, computed, fabricated and further measured freestanding Si_3N_4 PhC cavity, where waveguide with drilled holes is suspended in the air in contrast with photonic crystal cavity on substrate, in order to increase refractive index contrast between PhC waveguide and cladding, yielding to stronger confinement of the modes due the fact that light line is pulled up (light line determined as $\omega = ck/n_{clad}$). Thus, Fourier components of the resonance modes are situated further out of the light cone, resulting in lower radiation loss, yielding in higher Quality factor of the mode. However, fabrication of suspended PhC required several steps of electron beam lithography which is discussed in the *Supporting Information*.

Computation nanobeam and cross-bar PhC cavity

The first set of 3D simulations were focused to study high-Q resonant modes of the cavity by employing free open-source software MEEP [92]. In simulations a Gaussian pulse dipole source with a H_z main component (dipole is parallel to the electric field E_y) was positioned in the center of the cavity with pulse centered at λ_{res} with bandwidth $\Delta\lambda$.

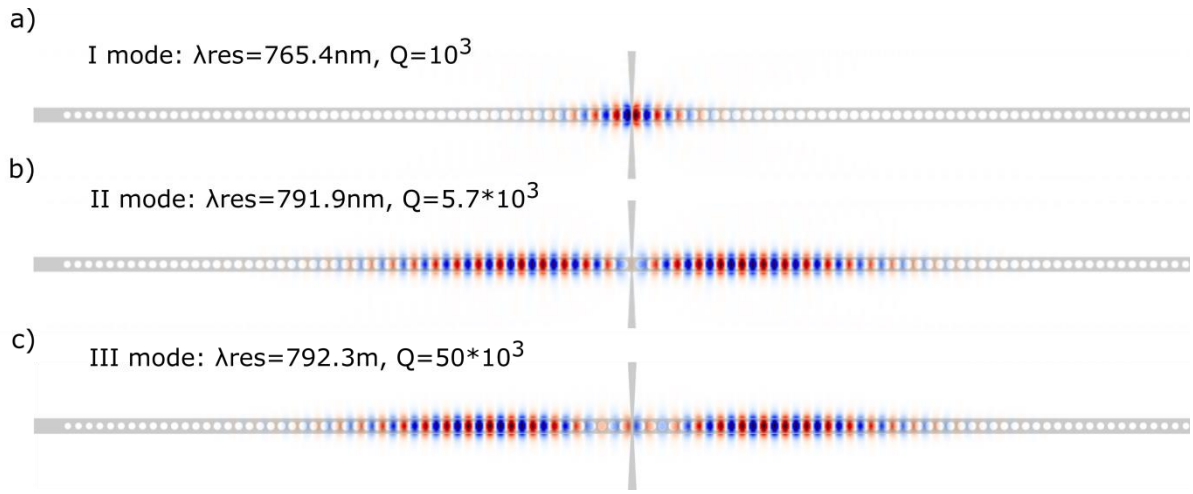

Figure 5.7. Simulated Electric field distribution (E_y component) TE-like fundamental **(a)**, second-order **(b)** and third-order resonance modes profile, supported in freestanding cross-bar PhC cavity. Electric field profiles superimposed with dielectric permittivity of the structure. PhC cavity parameters: cavity length 190 nm, first three segments from each side of cavity are identical with $ff = 0.30$, filling fraction of the next N=50 segments are quadratic tapered between $ff_f = 0.30$ to $ff_l = 0.16$ counting from the center, periodicity $a = 300nm$.

Firstly, it was performed 3D simulation of freestanding PhC cavity with geometric parameters previously determined during Band diagram computations presented in Paragraph 5.1.1. PhC cavity formed by two modulated photonic crystals (Bragg mirrors) from both sides of cavity constructed by segments with quadratic interpolated filling fraction. Electric field distribution for the first three resonance modes of considered cross-bar PhC cavity is shown in Fig. 5.7. As can be seen from simulations Quality factor of fundamental (further I mode) where electric field concentrates in the region of the cavity is $\mathrm{Q} = 10^3$ which is 50 times smaller than for the third-order mode (further III mode) $\mathrm{Q} = 50 * 10^3$. This can be partly attributed to the influence of cross-bar geometry.

To determine effect of crossed waveguide on Q-factor behavior of freestanding nanobeam and cross-bar PhC cavities (Fig. 5.8) with identical parameters were further compared. Electric field (E_y) distribution for the first three TE-like resonance modes for both PhC cavities are displayed in Fig. 5.8.

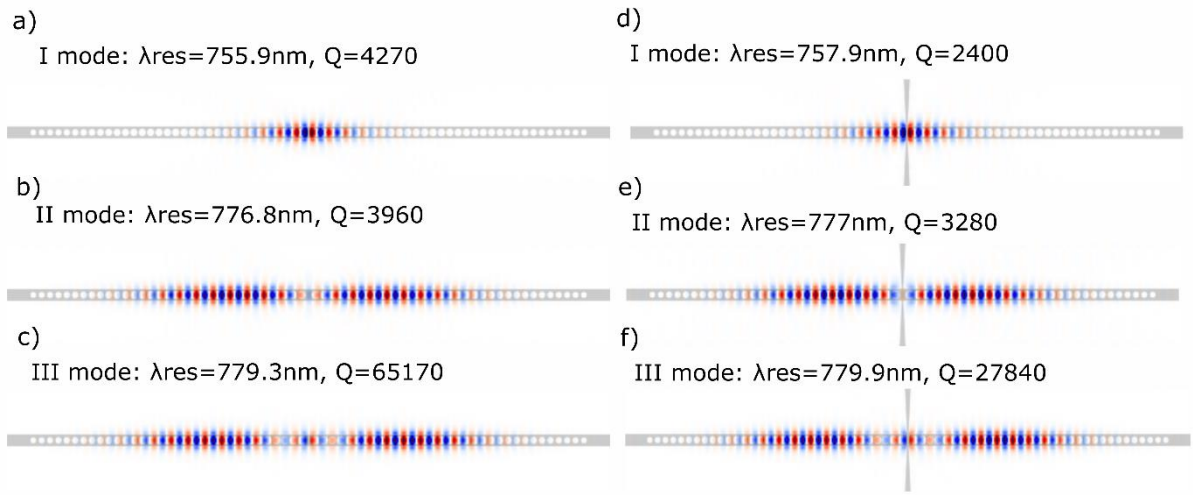

Figure 5.8. Simulated Electric field distribution (E_y component) TE-like fundamental (I mode) **(a,d)**, second-order (II mode) **(b,e)** and third-order (III mode) **(c,f)** resonance modes profile supported in freestanding nano-beam PhC cavity (a,b,c) and cross-bar PhC cavity (d,e,f). Electric field profiles superimposed with dielectric permittivity of the structure. PhC cavity parameters: cavity length 200 nm, first three segments from each side of the cavity are identical with $ff = 0.30$, filling fraction of the next N=30 segments are quadratic tapered between $ff_f = 0.30$ to $ff_i = 0.16$ counting from the center, periodicity $a = 290nm$.

As it can be seen, Q-factor of odd resonance modes of nanobeam PhC, where electric field is concentrated in the region of the cavity, is two times higher in comparison with cross-bar PhC cavity, due to the presence of crossed waveguide in the middle of the cavity, which acts as an 'extra channel' of optical loss, so that mode is leaked out for each cycle of the light inside the cavity. In contrast, Q-factor for the second order modes, which have nodes in the region of the cavity, are approximately equal for both geometry of cavities, since maximums of electric field are away from the center of cavity, thereby crossed waveguide does not influence. Thus, odd resonance modes, especially III mode, experience considerable damping due to the cross-bar as expected. Wavelengths of corresponding resonance modes for both types of PhC cavities are approximately equal.

5.1.3. Simulation and Experimental investigation of PhC cavity parameters

The chip with nanobeam and cross-bar simulated PhC cavities determined in Paragraph 5.1.2 was designed and fabricated. Fabrication is the subject of *Supplementary Information*. The design of the chip contained PhC devices with variety of parameters to define optimized architecture of cavity to achieve highest Quality factor. Via first sets of simulations (Fig.5.8) highest Q-factor was achieved for cross-bar PhC cavity with determined modulated Bragg mirrors (Paragraph 5.1.1), where filling fraction of the segments were quadratic tapered between $ff_f = 0.30$ to $ff_l = 0.16$ counting from the center, where the cavity length amounts 200nm and period amounts 290nm (periodicity can be tuned to match required resonance wavelength). Therefore, these values were chosen as the main based on which it was varied geometrical parameters of PhC cavities on chip.

Optical characterization of PhC devices was performed on the *fiber-array* setup via transmission measurements. The setup is introduced in the Paragraph 3.3. Depending on the measurements, either laser light from tunable TLB laser (765-780 nm) or supercontinuum light from white-light laser source (Leukos SM-30-UV) was coupled to the photonic device by employing apodized grating couplers which was examined in the Paragraph 2.1.2, transmitted light was coupled out on the second coupler, directed by further optical fiber and detected by either low-noise photoreceiver or spectrometer.

On-chip freestanding cross-bar PhC cavity device shown in Fig. 5.9, it contains four out-couplers to perform transmission measurements via couplers 1, 3 while crosstalk measurements discussed further in this chapter were performed via couplers 2, 4.

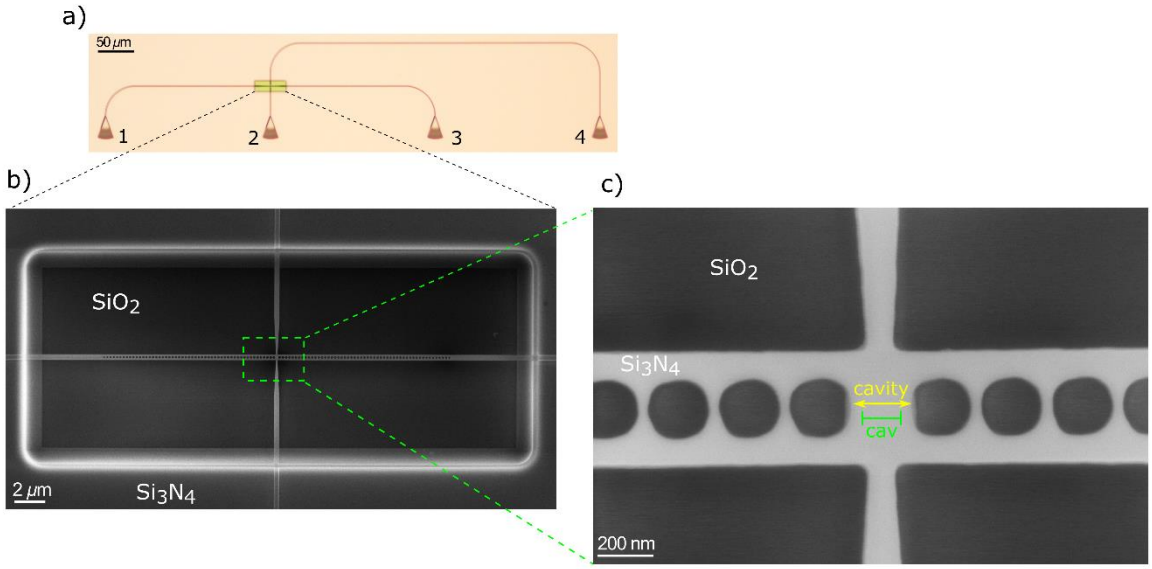

Figure 5.9.: Freestanding cross-bar PhC cavity. **a)** Optical Micrograph of PhC device. **b)** SEM image of free-standing PhC cavity with zoom-in in the cavity region **(c)**, where green line (cav.) indicates designed cavity length, *i.e.* distance between two central segments.

Variation of cavity length (cav)

In the first step it was investigated dependence of Quality factor and wavelength of resonance modes on the cavity length (indicated as *cav*. in Fig. 5.9), *i.e.* the distance between two central segments, since this parameter influences the most on Quality factor in comparison with other studied parameters of PhC cavity. Extra rounds of simulations were performed in order to predict Q-factor dependency on the cavity length for cross-bar PhC device with previously determined in Paragraph 5.1.1 periodicity, filling fractions of the segments and width of the waveguide, where electric field profiles for the first three resonance modes were shown in Fig. 5.8 d),e),f). To prove simulation results actual fabricated freestanding cross-bar PhC cavities were measured. Since the laser range was limited to 765-780 nm it was possible to monitor only the third and the fourth order modes (further III and IV order modes) in this wavelength window. In fact, III order mode showed highest Quality factor according to previously performed simulations as was depicted in Fig. 5.8. Experimental and simulation results are displayed in Fig. 5.10.

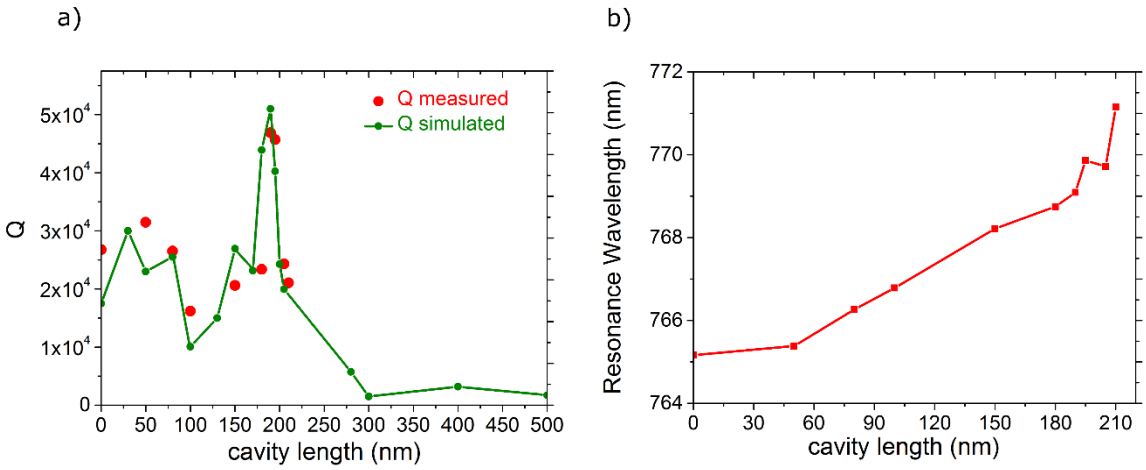

Figure 5.10. Experimentally measured (red curve) and simulated (green curve) dependency **(a)** Q-factor and **(b)** resonance wavelength of III-order TE-like resonance mode on cavity length for freestanding cross-bar PhC cavity with the following parameters: period a = 290nm, each modulated Bragg mirror consists 3 identical segments from each side of the cavity with $ff = 0.30$ following by N = 50 segments with quadratic tapered holes between $ff_f = 0.30$ $ff_l = 0.16$.

It is obvious that measured and simulated results are in agreement which is evident in Fig. 5.10 a). Measured Q-factor obtains maximum value $Q = 47 * 10^3$ determined as $Q = {}^{\lambda}/_{\Delta\lambda}$ while simulated is $Q = 51 * 10^3$, when cavity length is optimal 190nm for examined cross-bar PhC cavity parameters. Further increasing the spacing between two central holes, *i.e.* increasing cavity length, leads to drastically reduction of Quality factor. With increasing the length of the cavity there is more space for the resonance mode to oscillate, so mode is pulled down further from the upper band inside the bandgap, thus the resonance wavelength increases as shown in Fig. 5.10 b).

Measured Transmission spectrum of considered cross-bar PhC cavity with optimized cavity length 190nm is displayed in Fig. 5.11. Spectrum shown in a) over a broad wavelength range was obtained by coupling supercontinuum light by means of apodized grating coupler, thereby considered spectrum range is limited only by transmission wavelength range of coupler. Out-coupled light was detected with low resolution (1.3nm FWHM) spectrometer, therefore the highest quality factor Q=567 can be resolved. Since sensitivity of spectrometer was as well low and power of supercontinuum laser was not sufficient, the first three high Q-factor resonance modes were not detected with the spectrometer, due to low transmission because of scattering on non-uniformity as a result of fabrication imperfections. Higher order modes with lower Q-factor, where light makes less cycles inside the cavity, hence, experienced less scattering on fabrication imperfections, and were detected. d).

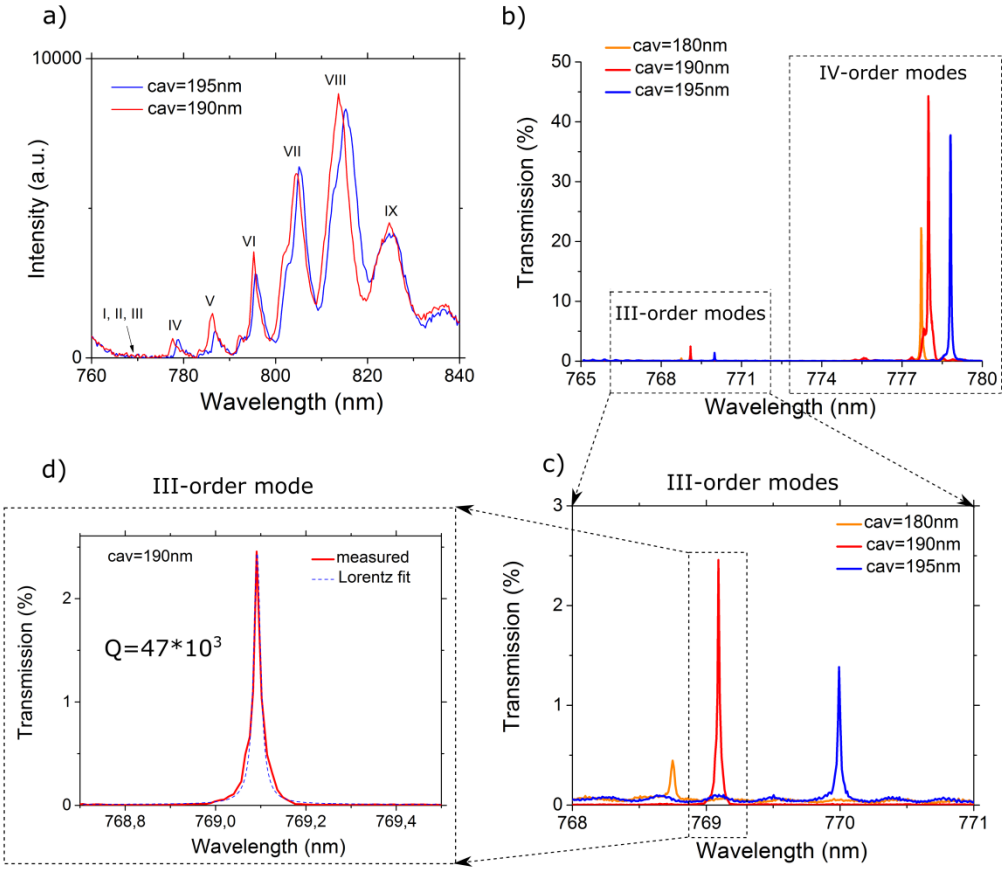

Figure 5.11. Measured transmission spectrum of freestanding cross-bar PhC cavities with optimized cavity length cav=190 nm (red curve), 195 nm (blue curve) by coupling supercontinuum light **(a)**, tunable laser light in the range 765-780 nm **(b)** with zoom-in into III-order modes on **(c)**. Index number of resonance modes is displayed on the plots. **d)** Measured III-order resonance peak (solid curve) and Lorentzian fit (dashed curve), measured $Q = 47 * 10^3$. Parameters of measured PhC cavity: period a = 290 nm, each modulated mirror consists 3 identical segments from each side of the cavity with $ff = 0.30$ following by $N = 50$ segments with quadratic tapered holes between $ff_f = 0.30$, $ff_l = 0.16$.

Therefore, it was employed more powerful tunable TLB laser (21mW output power) but with limited tuning range 765-780 nm with the scanning step 0.01nm. Laser light was coupled to the PhC device through coupler 1 (Fig. 5.9) so that III, IV-order resonance modes in the transmitted light was outcoupled from coupler 3 and were monitored with low-noise detector. Cavity resonances III- and IV-order peaks with the highest measured $Q = 47 * 10^3$ are shown in Fig. 5.11 b), c),

IV-order resonance mode was also experimentally studied for considered cross-bar PhC cavities with variation of cavity length, results are shown in Fig. 5.12. Q-factor experienced a slight decay with increasing cavity length with the highest measured value $Q = 23 * 10^3$ when there is no inserted extra spacing between two central holes (zero cavity length). Rise of resonance wavelength with increasing cavity length is as expected.

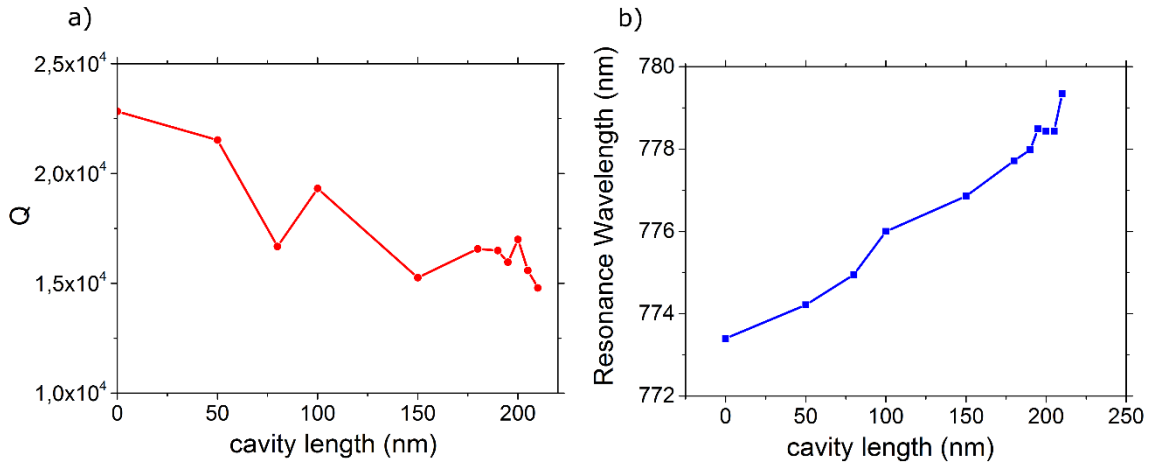

Figure 5.12. Experimentally measured dependency of Q-factor **(a)** and resonance wavelength **(b)** of IV-order TE-like resonance mode on cavity length for freestanding cross-bar PhC cavity with the following parameters: period $a = 290\,\mathrm{nm}$, each modulated mirror consists 3 identical segments from each side of the cavity with $ff = 0.30$ following by $N = 50$ segments with qudratic tapered holes in the range $ff_f = 0.30$ $ff_l = 0.16$.

Variation of ff_l

It was studied dependency Quality factor and resonance wavelength on the filling fraction of the last hole ff_l for freestanding nanobeam and cross-bar PhC cavities. It should be noted that changing the size of the last hole leads to the shift of filling fraction of all segments except the very first one, keeping other parameters constant.

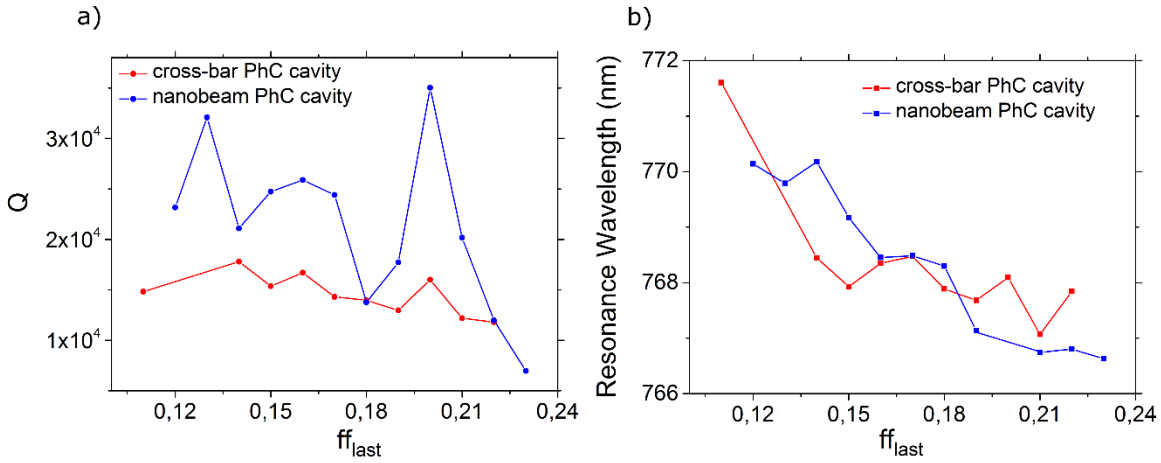

Figure 5.13. Experimentally measured Q-factor **(a)** and resonance wavelength **(b)** of III-order TE-like resonance mode as a function of filling fraction of the last segment ff_l for freestanding cross-bar PhC cavity (red curves) nanobeam (blue curves) cavities with identical parameters: $a = 290\,\mathrm{nm}$, $cav = 200\,\mathrm{nm}$, each modulated mirror consists 3 identical segments from each side of the cavity with $ff = 0.30$ following by $N = 30$ segments with quadratic tapered holes between $ff_f = 0.30$ and ff_l.

Regarding Q-factor it can be seen similar trends for both types of PhC cavities (cross-bar and nanobeam) as shown in Fig. 5.13 a), namely it is obtained peak values at $ff_l = 0{,}13$, $ff_l = 0{,}16$, $ff_l = 0{,}20$. Proving simulation results indicated in Fig. 5.8, Q-factor of cross-bar PhC device is approximately twice lower than for nanobeam PhC with identical parameters.

Increase ff_l shifts resonance wavelength toward shorter wavelength regardless the type of PhC device as depicted in Fig. 5.13 b), since averaged effective refractive index of resonance modes in the cavity decreases.

Although observed resonance wavelength of the third-order mode for cross-bar PhC cavity with $ff_l = 0.16$ is shifted on around 10nm in comparison with simulation results displayed on Fig. 5.8, which can be attributed to the fabrication imperfections, measured resonance wavelength for nanobeam and cross-bar PhC cavities with identical parameters are approximately the same as was predicted also by simulations.

Variation of N

In the next step, the dependency of Quality factor of PhC cavity on the number of mirror segments in each Bragg mirror was characterized. It was determined by measuring Transmission through nanobeam PhC cavity, namely tracing behavior of III- and IV-order resonance modes as depicted in Fig. 5.14.

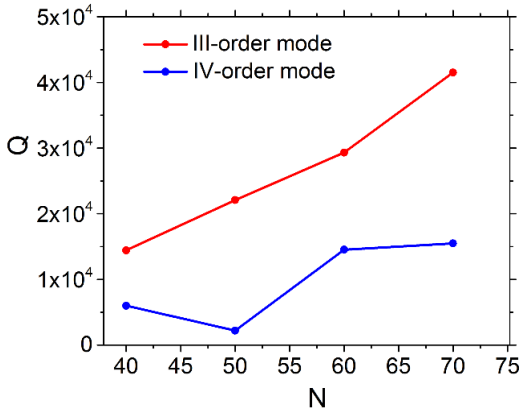

Figure 5.14. Experimentally measured Q-factor of III-order (red curve) and IV-order (blue curve) TE-like resonance mode as a function of number of segments in each Bragg mirror for freestanding nanobeam PhC cavity with the following parameters: a = 295nm, cav = 100nm, each modulated mirror consists 3 identical segments from both sides of the cavity with $ff = 0.30$ following by N segments with quadratic tapered holes from $ff_f = 0.30$ to $ff_l = 0.16$.

Anticipated trend, proved in the measurements, of rise Q-factor with increasing number of segments in each photonic crystal mirror from both side of cavity region, due to the deeper penetration of the mode into the mirror, resulting in exponential rise of Q_{wg}, thus lifetime of the mode trapped in the cavity is longer. With infinite number of holes Q_{wg} will exponentially grow, however overall Q-factor will be limited by radiation loss due to

not-complete bandgap of considered 1D PhC cavity. This trend can be attributed to 1D cross-bar PhC devices as well.

Tuning mechanisms of λ_{res}

The next goal was to determine mechanisms of tuning wavelength of resonance modes for cross-bar PhC cavity.

Obviously, with increasing periodicity a of mirror holes resonance wavelength rises by Bragg's law, which is an evident in Fig. 5.15. Furthermore, increasing length of the cavity leads to increase of resonance wavelength as well, since the mode has greater space to oscillate in the cavity region, so the mode is pulled down further from the upper band inside the gap.

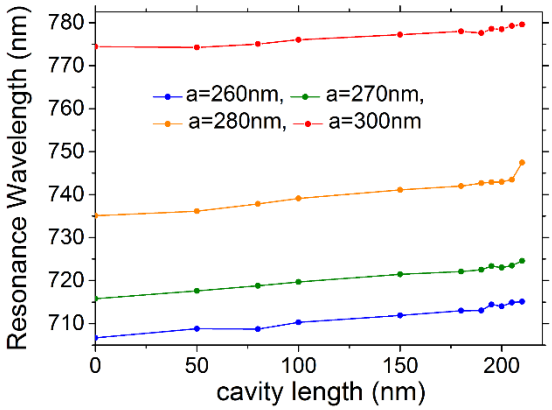

Figure 5.15. Experimentally measured Resonance wavelength of the I mode as function of cavity length for freestanding cross-bar PhC devices with different periods (color of curve indicates periodicity labeled in the legend of the plot).

It can be derived tuning coefficients of resonance wavelength with periodicity $\frac{\delta\lambda}{\delta\Lambda} \approx 0.5 - 2$ and cavity length $\frac{\delta\lambda}{\delta cav} \approx 0.02 - 0.05$. Thus, it is clear that change of spacing between holes has higher impact on the resonance wavelength. Therefore, periodicity ensures scaling of PhC cavity, unless drastic change of period leads to the shift of the bandgap out of the spectral range where required resonance wavelength needed to be localized.

Resonance wavelength is sensitive to the width of the tapered end of cross-bar and number of mirror segments of PhC cavity, experimental results are displayed in Fig. 5.16.

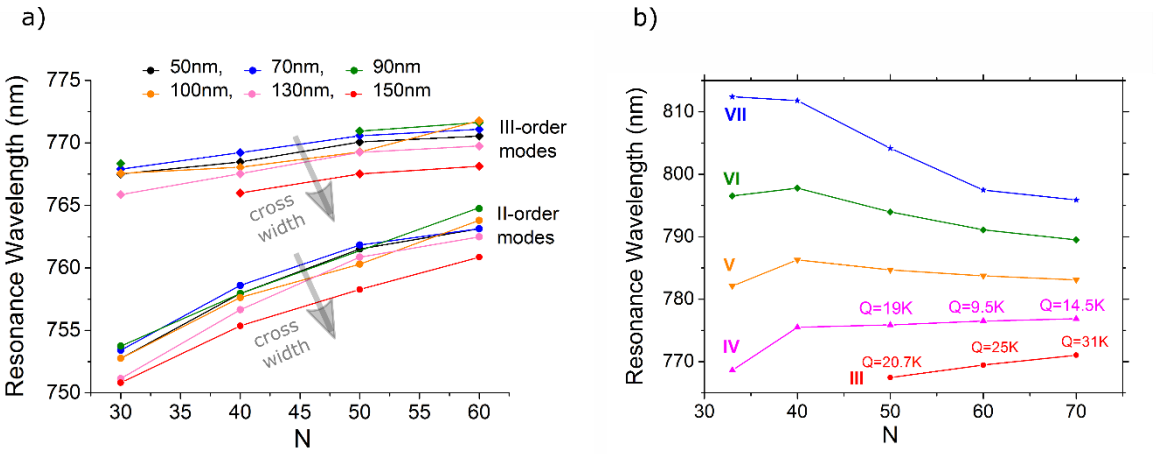

Figure 5.16. a) Experimentally measured dependency of resonance of II- and III-order modes on number of mirror segments N. Colorful curves correspond to freestanding PhC devices with different width of cross-bar indicated in the legend of the plot. PhC cavity parameters: $a = 295\,\mathrm{nm}$, $cav = 200\,\mathrm{nm}$, $ff_f = 0.29$, $ff_l = 0.16$. **b)** Resonance wavelength as a function of number of mirror segments N. Index of the mode is indicated on the plot. PhC cavity parameters: $a = 290\,\mathrm{nm}$, $cav = 200\,\mathrm{nm}$, $ff_f = 0.30$, $ff_l = 0.16$, width of cross-bar 100 nm.

Interestingly, the rise of width of crossed waveguide leads to decrease of resonance wavelength as can be seen in Fig. 5.16 a), however effective refractive index in the middle of the cavity increases which would expectedly shift resonance towards longer wavelength. This can be explained in the following way: rise of the width of tapered end of cross-bar increases leakage of the resonance mode into crossed waveguide for each cycle of propagation of the mode inside cavity, thus crosstalk is higher, therefore penetration of the mode inside photonic crystal mirrors is slightly lower, resulting in reduction of effective length of the cavity (assuming that other parameters kept constant), thus resonance wavelength decreases. Increasing width of the crossed waveguide will also lead to decrease of *Q*-factor since crosstalk is higher.

Another trend derived from Fig. 5.16 a): rise of the number of mirror segments increases resonance wavelength for II-and III-order modes because of the growth of effective length of PhC cavity, as a result of deeper penetration of the mode into longer Bragg mirrors from both sides of cavity. At the same time for higher order modes this trend is not always true as indicated in Fig. 5.16 b). Higher order modes are lossier, *i.e.* have lower *Q*-factor, since they experience higher radiation loss. Thus, beginning from certain number of mirror segments further increase of N yields in shorter distance penetration of resonance mode into Bragg mirror, yielding in reduction of effective length of PhC cavity, thereby resonance wavelength decreases. Moreover, this tuning effect of resonance wavelength is stronger for higher index mode. As illustrated in Fig. 5.16 b) for III- and IV-order modes increasing N still leads to slight rise of resonance

wavelength, in contrast with V-, VI- and VII- modes, where beginning from N=40 mirror segments resonance shifts towards lower wavelength range as was explained.

PhC cavity in comparison with Fabry-Perot cavity

In PhC cavity resonance mode (standing wave) is trapped in between two Bragg modulated mirrors, so it is equivalent to superposition of two counter-propagating planewaves which are backreflected from Bragg mirrors (as was shown in Paragraph 2.1.4). The difference is that in ideal Fabry-Perot cavity radiation loss is ignored and the only considered loss mechanism is due to imperfections in mirrors. One more important difference that resonance peaks in Fabry-Perot cavity are equidistant in contrast with localized modes of PhC cavity. It can be explained in the following way on the example of simulated and further fabricated and measured freestanding cross-bar PhC cavity. Computation examination of considered PhC cavity showed the following resonance modes presented in the Table 2, which was further proved during transmission measurements shown in the next Paragraph 5.2.1.

I mode	$\lambda_{res} = 736.4\ nm$
II mode	$\lambda_{res} = 752.2\ nm$
III mode	$\lambda_{res} = 754.5\ nm$
IV mode	$\lambda_{res} = 762.3\ nm$
V mode	$\lambda_{res} = 765.1\ nm$
VI mode	$\lambda_{res} = 772.5\ nm$
VII mode	$\lambda_{res} = 775.3\ nm$
VIII mode	$\lambda_{res} = 785.3\ nm$
IX mode	$\lambda_{res} = 795.5\ nm$

Table 2. List of simulated Resonance modes of freestanding cross-bar PhC cavity with lattice constant $a = 280\ nm$, cavity length 195 nm and modulated Bragg mirror which consists of 3 identical segments from both sides of the cavity with $ff = 0.30$ following by 40 segments with quadratic tapered holes in the range $ff_f = 0.30$ to $ff_l = 0.16$.

As can be seen from the Table 2 resonance wavelength of the I mode is on 15.8 nm lower than for the II mode, whereas the difference between II and III modes is only 2.3nm, the same trend holds true for the III mode, which wavelength lower than IV mode on 7.8nm and for further odd modes. This behavior is direct consequence of electric field distribution of the modes inside PhC cavity, namely along distributed Bragg mirrors (see Fig. 5.8).

In the far generalization, consideration of two certain resonance mode inside PhC cavity can be approximated by equivalent Fabry-Perot cavity, which theoretically can support these particular modes. For measured two modes carried in cross-bar PhC cavity shown in Fig. 5.17, difference between two peaks is 8.8nm, which corresponds to equivalent Fabry-Perot etalon with optical

length 20.76μm, which is less than the geometrical length of the entire PhC (31.68μm) as expected.

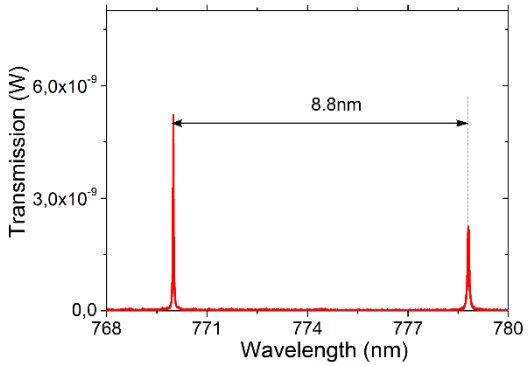

Figure 5.17. Experimentally measured transmission spectrum in the range 765-780 nm of freestanding cross-bar PhC cavity with cavity length 195 nm.

Modulated Photonic crystal (Bragg mirror)

It was designed, fabricated and measured separate photonic device consists of freestanding modulated crystal which is employed as Bragg mirror (Fig. 5.18 a)) in considered PhC cavities. Measured Reflection spectrum of fabricated Bragg mirror is shown in Fig. 5.18 b) (pink curve), as can be seen bandwidth of the reflection spectrum is in the range ≈ 740 nm-785 nm, which is in agreement with simulated bandgap value (717-791 nm), investigated in Paragraph 5.1.1.

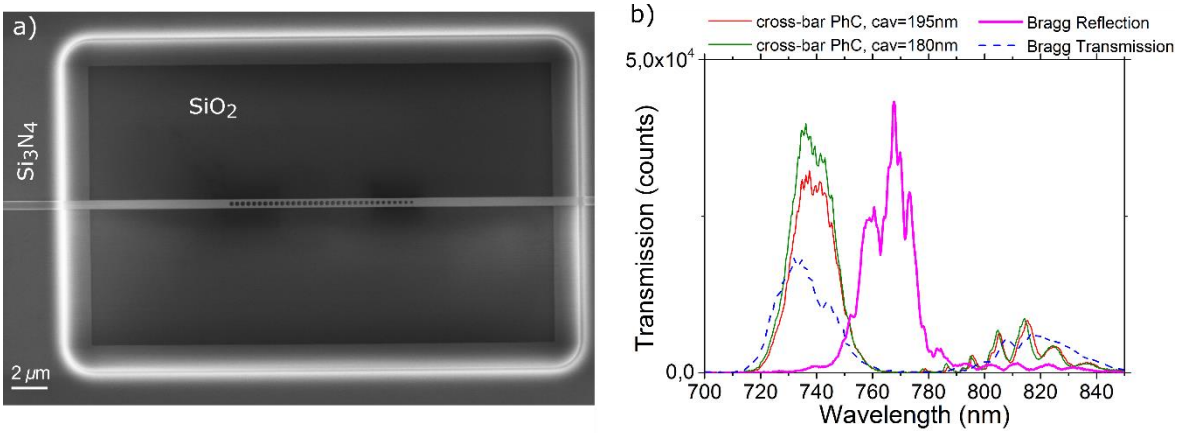

Figure 5.18. a) SEM image of freestanding Bragg mirror with periodicity of air holes 300nm. **b)** Measured Reflection (pink curve) and Transmission (blue curve) spectrum of the Bragg mirror. Transmission spectrum of freestanding cross-bar PhC cavity, which contains Bragg mirrors with identical parameters with cavity length 180 nm (green curve) and 195 nm (red curve), respectively. Bragg mirror parameters: periodicity 300nm, three identical segments with $ff = 0.30$ following by $N = 50$ segments with quadratic tapered holes from $ff_f = 0.30$ to $ff_l = 0.16$.

This can be explained by stronger bandgap confinement of resonance modes in close vicinity to the band edge as was noted also in [95].
With decreasing periodicity of the air holes in Bragg mirror the bandgap, thus reflection spectrum will be blue-shifted to in particular required wavelength 740nm, therefore wavelengths of resonance modes of corresponding PhC cavity will be shifted in the shorter wavelength range as well. As was investigated in this chapter change of the cavity length shifts resonance wavelength of PhC cavity, however with lower tuning coefficient in comparison with change of period.
Increasing ff of the segments in Bragg mirror decreases effective refractive index of Bloch mode, thus bandgap shifts in lower wavelength region, however in this case the diameter of the first and last holes should be optimized once again (the holes in between are determined by quadratic interpolation between ff_f and ff_l) through simulations to achieve smooth transition of Bloch mode into waveguide mode, to decrease radiation loss.

5.2 Full characterization of cross-bar PhC cavity for evanescently coupled emitter

5.2.1 Simulation and Experimental Results

The goal was to design, simulate, fabricate, optically characterize and employee cross-bar PhC cavity for evanescent coupling SiV as potential single photon emitter. Considered *novel* cross-bar structure allows to outcouple fluorescence light through waveguide which consists PhC, while excitation light can be coupled through crossed waveguide, at the same time.

Optimized parameters for freestanding cross-bar PhC cavity was determined and verified in the Paragraph 5.1.3, in particular optimized cavity length was defined as 190-205nm. Therefore, main parameters of PhC cavity were kept the same only period was varied to ensure scalability to match target wavelength which corresponds to SiV ZPL $\lambda = 738nm$.
Simulated Electric field distribution (E_y- component) for the first three order TE-like resonance modes for fabricated cross-bar PhC cavity is shown in Fig. 5.19. As can be seen the first mode is very close to the desired $\lambda = 738nm$.

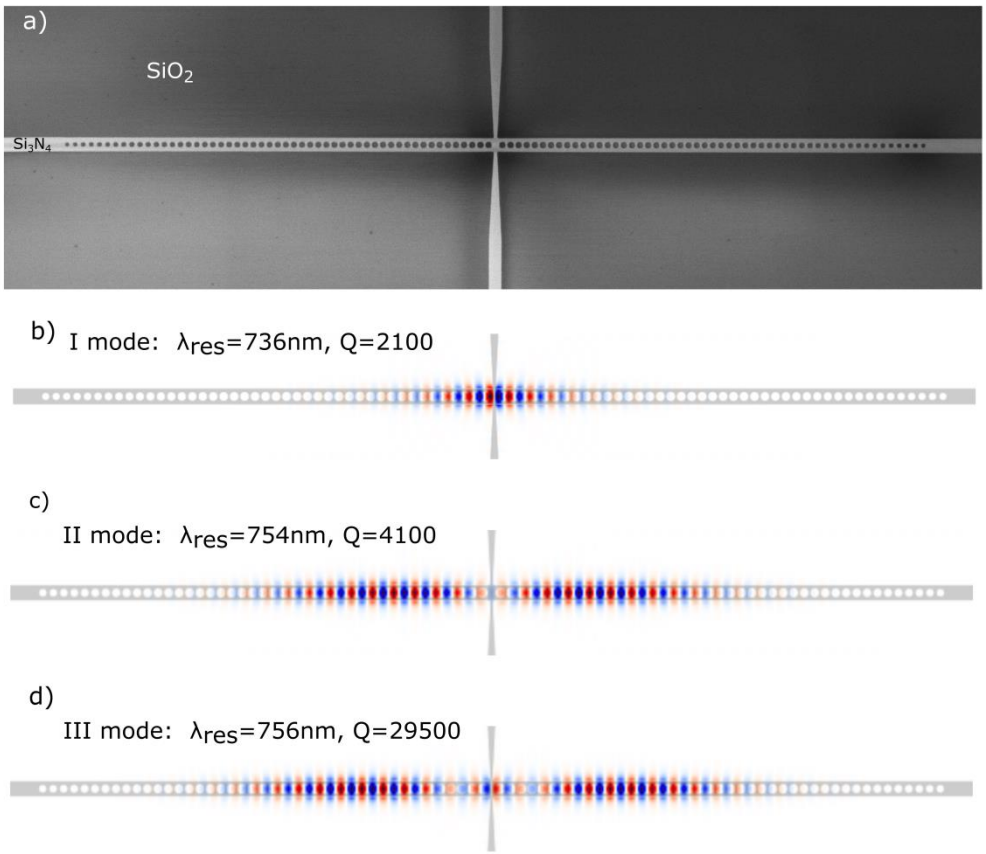

Figure 5.19. a) SEM image of fabricated freestanding cross-bar PhC cavity. Simulated Electric field profile (E_y component) of TE-like resonance modes, superimposed with dielectric permittivity of the structure, of cross-bar PhC cavity for I-, II-, III-order resonance modes on **(b)**, **(c)**, **(d)** respectively. Resonance wavelength and Q-factor are indicated on the plot.
PhC cavity parameters: cavity length 195nm, first three segments from each side of cavity are identical with $ff = 0.30$, the next N=40 segments quadratic tapered between $ff_f = 0.30$ and $ff_l = 0.16$ counting from the center, periodicity $a = 280nm$.

The first mode was further explored, namely extra set of simulations were performed to determine magnetic field (H_z-component), Poynting vector (S) and Energy density distributions displayed in Fig. 5.20. To decrease computation time and highly resolve resonance modes number of mirror segments were decreased in further simulations.

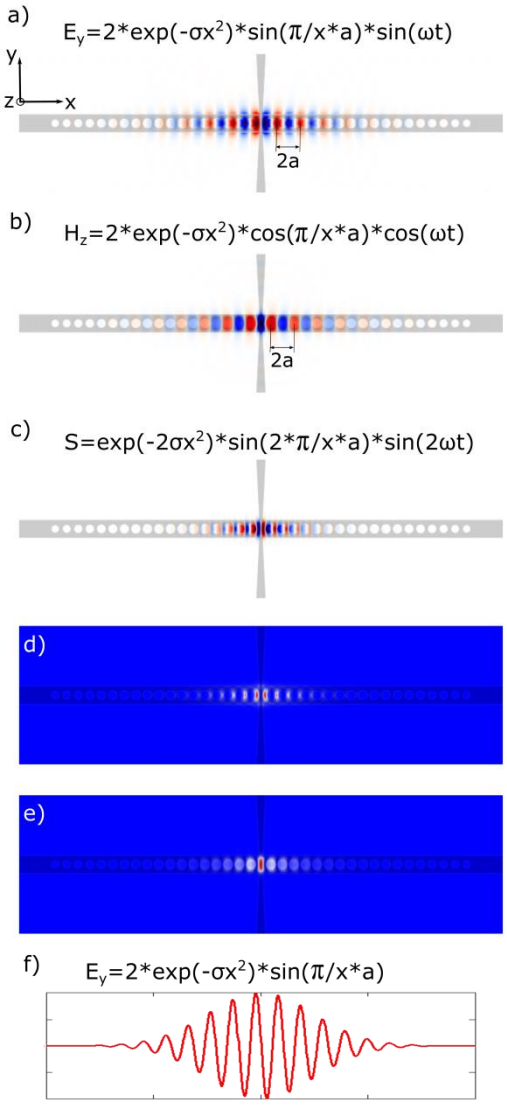

Figure 5.20. Simulation results. **a)** Electric field distribution (E_y component). **b)** Magnetic field distribution (H_z component). **c)** Poynting vector distribution. **d)** Energy density distribution at the moment of time when electric energy density component is maximum. **e)** Energy density distribution at the moment of time when magnetic energy density component is maximum. All distributions, superimposed with dielectric permittivity of the structure, of the fundamental TE-like resonance mode for freestanding cross-bar PhC cavity with the following parameters: cavity length 195 nm, first three segments from each side of cavity are identical with $ff = 0.30$, next N=40 segments quadratic tapered between $ff_f = 0.30$ to $ff_i = 0.16$ counting from the center, periodicity $a = 280nm$. **f)** Analytical Electric field distribution (E_y component).

It should be highlighted important aspects of electro-magnetic field, Poynting vector and Energy distributions for the first-order resonance mode which are evident in Fig. 5.20:

- Electric field has a Gaussian envelope $E_y = \sin\left(\frac{\pi x}{a}\right) * \sin(\omega t) * \exp(-\sigma x^2)$, determined in Paragraph 2.1.4, as a result of quadratic tapering of filling fraction of the

segments in each Bragg mirror from both sides of the cavity. This suppresses mode mismatch between cavity and Bragg mirror regions by insuring smooth transition of effective refractive index of the mode resulting in decrease radiation loss, due to suppression of tails of Fourier harmonics of the resonance mode inside the light cone.

- There is a node in the E_y distribution in the middle of the cavity, which can be attributed to two effects: to presence of crossed ('pump') waveguide, which acts as a channel of optical loss, yielding in decrease of Quality factor, and also to particular cavity length.
- Explored cross-bar PhC cavity is dielectric type, *i.e.* electric field of the mode is concentrated in higher index material (Si_3N_4), as can be seen in Fig. 5.20 a).
- Electric E_y and Magnetic H_z components are inversed, namely there is antinode in H_z distribution in the center of cavity in contrast with E_y. This can be explained by the nature of standing wave, where the energy is passed back and force between the region where electric field has maximum (magnetic field has a node) and the region where magnetic field has a maximum (electric field has a node) with zero energy net stream in both directions, as can be seen in Fig. 5.20 d), e). Standing wave does not transfer energy, since it is superpose of two travelling waves which travel in opposite directions, *i.e.* carry energy in opposite directions.
- Poynting vector of standing wave $S_x = E_y * H_z = \sin(2\omega t) * \sin(2kx) * \exp(-2\sigma x^2)$ oscillates with double frequency in comparison with corresponding field components. Poynting vector shows an impact of both magnetic and electric components at one time, in contrast with the energy distribution for standing wave; the time-averaged of Poynting vector is zero.
- The envelope of Energy and Poynting vector distributions described by $\exp(-2\sigma x^2)$ decays two times faster in comparison with electric and magnetic fields.

Measured transmission spectra of fabricated PhC cavities with variation of cavity length embedded in photonic devices are shown in Fig. 5.21. It can be tracked resonance peaks in each spectrum which slightly shift with tiny change of cavity length. In particular, it is shown spectra for two identical PhC devices with cavity length 205nm (green and blue curves in Fig. 5.21), which has a slight shift < 1nm in comparison with each other, which proves reproducibility of freestanding PhC devices on the chip.

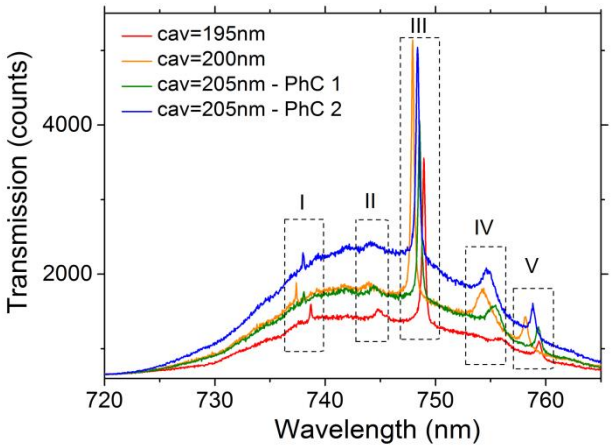

Figure 5.21. Experimentally measured Transmission Spectrum of freestanding cross-bar PhC cavities with varied cavity length (195-205nm) colorcoded and indicated in the legend. PhC cavities have the following parameters: $a = 280nm$, first three mirror segments from each side of cavity are identical with $ff = 0.30$, next N=40 segments quadratic tapered from $ff_f = 0.30$ to $ff_l = 0.16$ counting from the center. Index of the mode is indicated on the plot.
Transmission measurements of considered on this plot PhC devices were performed in the group of Prof. A. Kubanek in Ulm University.

Comparison of simulated and measured transmission spectra for one PhC cavity is shown in Fig. 5.22.

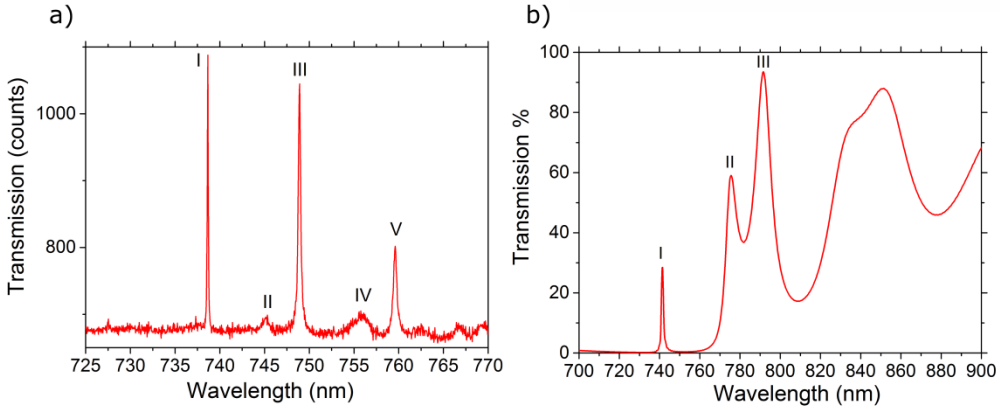

Figure 5.22. Measured **(a)** and simulated **(b)** Transmission Spectra of freestanding cross-bar PhC cavity with cavity length 195nm, $a = 280nm$, first three mirror segments from each side of the cavity are identical with $ff = 0.30$, next N segments are quadratic tapered from $ff_f = 0.30$ to $ff_l = 0.16$ counting from the center, where measured device contains N=40 segments, whereas simulated - N=7. *Transmission measurement of considered on this plot PhC device was performed in the group of Prof. A. Kubanek in Ulm University.*

As can be seen measured and simulated resonance wavelength of the first mode are almost identical (with slight shift 2 nm) in contrast with higher order modes. It can be explained by the

electric profile of the I mode, which is distributed over approximately first 10 holes, as can be seen in Fig. 5.19 b) and 5.20a). Higher order modes distributed over entire length of PhC, taking into account that it was simulated PhC with 10 segments in each mirror in comparison with measured fabricated device containing 43 segments in each PhC mirror.
It was performed more precise simulations to determine resonance wavelength and Quality factor for the identical cross-bar PhC device with 43 segments, comparison with measurements results presented in the Table 3.

	Simulated λ_{res}	Measured λ_{res}	Simulated Q-factor	Measured Q-factor
I mode	736.4 nm	738.6 nm	2100	6500
II mode	752.2 nm	745.3 nm	4200	4100
III mode	754.5 nm	748.9 nm	27600	2500
IV mode	762.3 nm	755.8 nm	3300	2400
V mode	765.1 nm	759.6 nm	25500	1740

Table 3. Simulated and Measured Resonance wavelength and Q-factor of cross-bar PhC cavity with cavity length 195nm, $a = 280nm$, first three mirror segments from each side of cavity are identical with $ff = 0.30$, next N=40 segments are quadratic tapered from $ff_f = 0.30$ to $ff_l = 0.16$ counting from the center.

Simulation results presented in Table 3 are in agreement with optical characterization of fabricated devices with a discrepancy, which can be attributed to fabrication imperfections, namely for fundamental mode there is a slight shift of 2nm, while for higher order modes $\approx$ 7nm. In order to determine influence of the crossed waveguide on transmission, it was computed transmission through Nanobeam PhC also (Fig. 5.23).

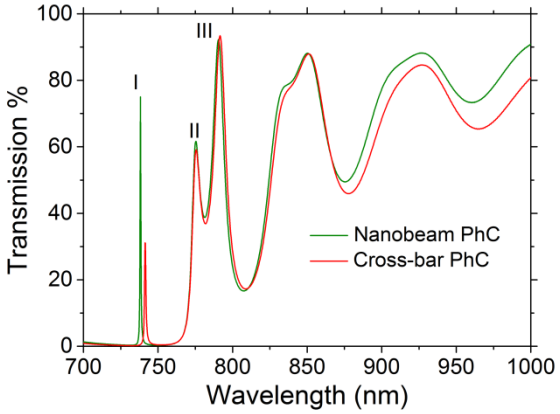

Figure 5.23. Comparison of simulated transmission through freestanding cross-bar (red curve) and Nanobeam (green curve) PhC cavity with the rest identical following parameters: cavity length 195nm, $a = 280nm$, first three mirror segments from each side of cavity are identical with $ff = 0.30$, next N=40 segments are quadratic tapered from $ff_f = 0.30$ to $ff_l = 0.16$ counting from the center.

Transmission of the fundamental mode through cross-bar PhC is ≈ two times lower in comparison with nanobeam PhC, which is direct consequence of presence of crossed waveguide, since the peak of electric field of the fundamental mode is concentrated in the center of the cavity.

To sum up, NDs (SiV) can be evanescently coupled to the fundamental mode (measured $\lambda_{meas\_res} = 738.6nm$) matched to ZPL of SiV of fabricated and investigated cross-bar PhC cavity device on chip, where excitation light can be coupled and carried to the emitter by tapered crossed waveguide, taking into account measured crosstalk -20 dB, in other words 20 dB extra filtration of pump light.
It is obvious that emitter should be positioned in the antinode of electric field distribution of matched resonance mode in order to obtain strong Purcell enhancement and, thereby, high coupling efficiency into waveguide mode. For positioning of ND cluster on the cavity region it is consistently employed an atomic force microscope (AFM) [96], in particular pick and place method in contact mode of AFM. Further pushing of ND ensures fine positioning of the source. Optimized position of the dipole on the cavity region, where maximum enhancement of emitted light can be obtained, was evaluated via simulations of Local Density of States (LDOS) enhancement investigated in Paragraph 5.2.2. The main figure of merit of emitter coupled into cavity is transmission coupling efficiency into cavity (β-factor), which is evaluated in Paragraph 5.2.3.

5.2.2 Simulation of Local Density of States Enhancement spatial map

The goal was to determine position of evanescently coupled source on the cavity region, where it can be achieved maximum Purcell enhancement factor of emitted light, in order to increase coupling efficiency of the emitted light into waveguide mode. As it was set in the Paragraph 2.2, Purcell enhancement factor approximates single-resonant LDOS enhancement, where the latter one is proportional to overlap integral between electric filed distribution of the resonance mode of the cavity and electric pattern of the source. Therefore, maximum enhancement of emitted light can be achieved by placing the source in the antinode of electric field of matched by the wavelength and polarization resonance mode.

LDOS enhancement spectrum $LDOS_{x_0,y_0,z_0}(\lambda)$ was determined via Finite Difference Time Domain (FDTD) simulation using MEEP software [92]. Gaussian pulse point-dipole was located in varied position (x_0, y_0, z_0) where the major field component of the dipole was set as E_y to excite TE-like resonance modes. The LDOS calculation needs to run for a full period of the cavity lifetime $2Q/f_{res}$, therefore it was computed PhC cavity with fewer number of mirror segments than in actual fabricated device, to decrease computation time which influences only on Quality-factor, *i.e.* linewidth of resonance peaks.

LDOS characterizes interaction between electric field of the dipole and electric field distribution of the resonance modes in the cavity, therefore source position and frequency are important. Thus, it was performed set of simulations to determine LDOS spectrum of resonance modes for different positions of the dipole along PhC (along x-axis in Fig. 5.20), since convolution of electric field along this direction is the strongest. Shift the dipole either along width or height of the waveguide from the center (along y -, z -axis, respectively) leads to only slight decay in the enhancement. It was studied relative LDOS enhancement spectrum in respect to the structure without scattering elements, *i.e.* without drilled holes. Thus, computed Normalized LDOS spectrum for variation of positions of dipole on top of cavity region is shown in Fig. 5.24.

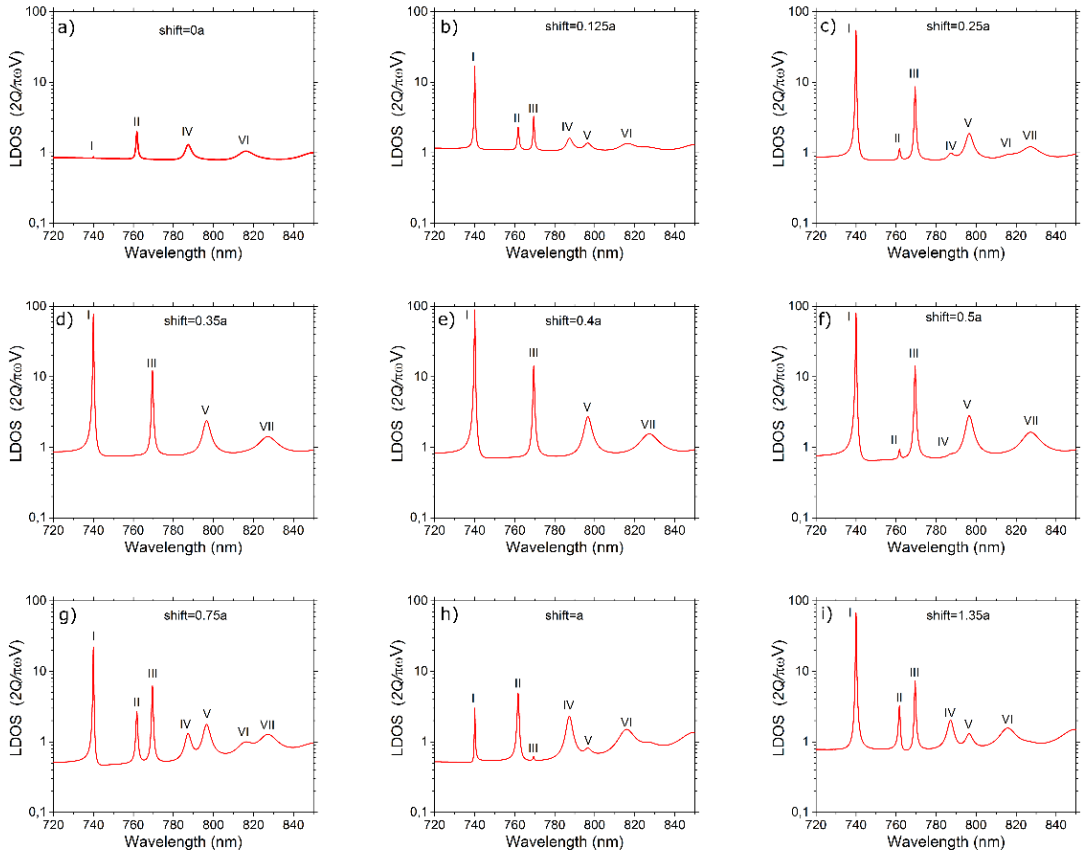

Figure 5.24. Simulated LDOS spectrum enhancement of the light emitted from the dipole placed on top of freestanding cross-bar PhC cavity, where the dipole position along longitudinal direction, (*x*-axis in Fig. 5.20) is varied. The positions are indicated in terms of the shift of the dipole from the center along *x*-axis, the shift is weighted in *a* and indicated on the plots. Freestanding cross-bar PhC cavity has following parameters: cavity length 195nm, first three segments from each side of cavity are identical with $ff = 0.30$, next N=15 segments quadratic tapered from $ff_f = 0.30$ to $ff_l = 0.16$ counting from the center, periodicity $a = 280nm$.

To sum up results in more conclusive way it was built LDOS enhancement map illustrated in Fig. 5.25, which explicitly allows to track spatial distribution of odd and even resonance modes with corresponding LDOS enhancement factors.

Important conclusions from simulations of LDOS enhancement reported below.

- When the dipole is placed in the center of the cavity (position 1 in Fig. 5.25) coupling to even resonance mode experiences only slight enhancement since there is a minimum in the electric field distribution (major E_y-component) of corresponding even resonance modes. Whereas coupling to odd resonance modes leads to absolute minimum enhancement factor, since there is a node in the electric field distribution of corresponding odd resonance modes, which can be seen in electric field distribution for the first mode shown in Fig. 5.19 b). Therefore, peaks corresponds to odd modes are missed in LDOS enhancement spectrum in Fig. 5.24 a).
- Shifting the emitter away from the center of the cavity along PhC leads to drastic rise of the enhancement of coupled light into odd modes and in contrast – decay of the enhancement of light coupled into even modes. Thereby, enhancement of odd resonances starts appearing and growing with shifting the dipole further away from the symmetry plane as shown in Fig. 5.25 b), e).

  Shift of the dipole on 0.4a (position 5 in Fig. 5.25) leads to maximum enhancement of coupled light into odd modes, as displayed in LDOS spectrum in Fig. 5.24 e), since the dipole is located in antinode of corresponding odd resonance mode. At the same time, this position of the dipole leads to minimum enhancement of coupled light into even modes, which is as well explained by the distribution of the electric fields of corresponding even localized modes.
- Coupling into considered odd modes leads into higher LDOS enhancement factor in comparison with even modes, which can be mostly attributed to higher Q-factor and also to lower mode volume of odd modes for this particular PhC cavity.
- Emission of the source in the bandgap (off the resonance modes) is inhibited, but since it is investigated 1D cross-bar PhC cavity which has not-complete bandgap (subject of Paragraph 5.1.1), radiation modes occurs for each frequency where emitted light can be coupled, leading into LDOS enhancement ≈ 1 in the bandgap region (LDOS 'background' on Fig. 5.24 and 5.25).

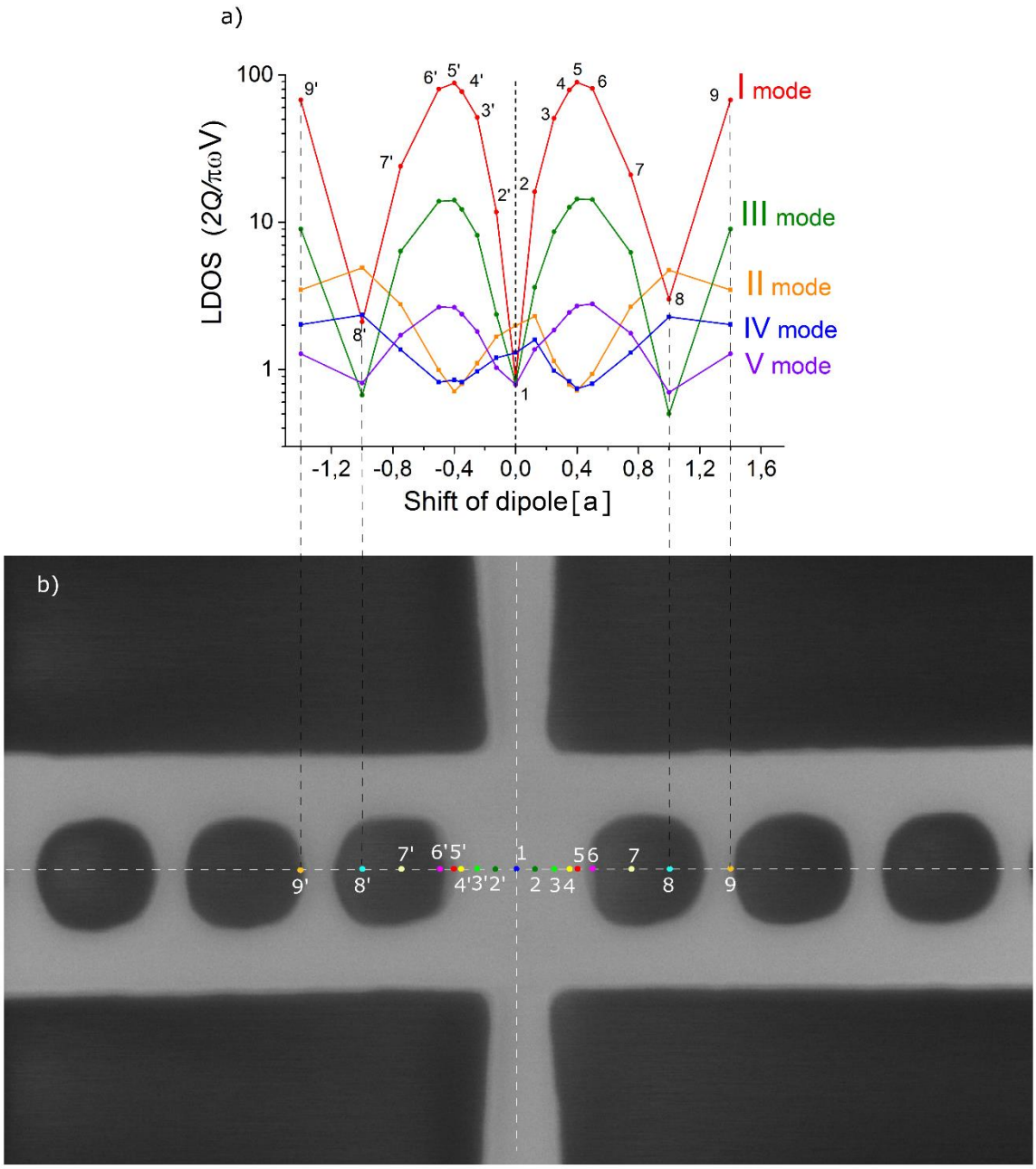

Figure 5.25. a) Simulated LDOS spectrum enhancement of the light emitted from the dipole placed on top of freestanding cross-bar PhC cavity, where the dipole position along longitudinal direction, (*x*-axis in Fig. 5.20) is varied. The positions are indicated in terms of the shift of the dipole from the center along *x*-axis in Fig. 5.20, the shift is weighted in *a*.
Colorful curves correspond to resonance modes labeled in Roman numbers (I-V) on the plot. **b)** SEM image of cavity region of fabricated and measured freestanding PhC cavity, where points indicate position of the dipole for which LDOS enhancement spectrum was computed on (a); numbers numerous the positions. PhC cavity has the following parameters: cavity length 195nm, first three segments from each side of cavity are identical with $ff = 0.30$, next N=15 segments quadratic tapered between $ff_f = 0.30$ and $ff_l = 0.16$ counting from the center, periodicity $a = 280nm$.

Impact of different factors on LDOS

To determine influence of crossed waveguide on LDOS enhancement it was simulated freestanding nanobeam PhC cavity with identical parameters (Fig. 5.26 a)). As can be seen cross-bar decreases mostly the enhancement of the fundamental mode (in around 5 times), as well as shifts resonance wavelength (on 3nm) in lower wavelength range, where its influence on higher order modes is negligible, as can be predicted from electric field distribution of the modes (Fig. 5.19).

Maximum theoretical enhancement factor can be obtained in case of embedding the source inside the PhC, namely at the center of the cavity, in this case enhancement factor of all modes increase by ≈ 2 times as shown in Fig. 5.26 b). Another consequence of this optimized position is suppressing enhancement of the light coupled into radiation modes due to not-complete bandgap of 1D PhC. However, in terms of fabrication emitter can be positioned on top of the cavity.

Shift of the source along width of the waveguide, *i.e.* along *y*-axis decreases LDOS enhancement as can be seen on Fig. 5.26 c), namely in 1.8 times in case of moving the dipole on *0.25w* where *w* - width of waveguide equaled 450nm, which corresponds to the shift on 112.5nm from the center. Placing the dipole at the edge of the waveguide, *i.e.* shift of the dipole on 0.5a-10nm=215nm (violet curve) leads to decrease of LDOS enhancement in 3 times in comparison with symmetric central position.

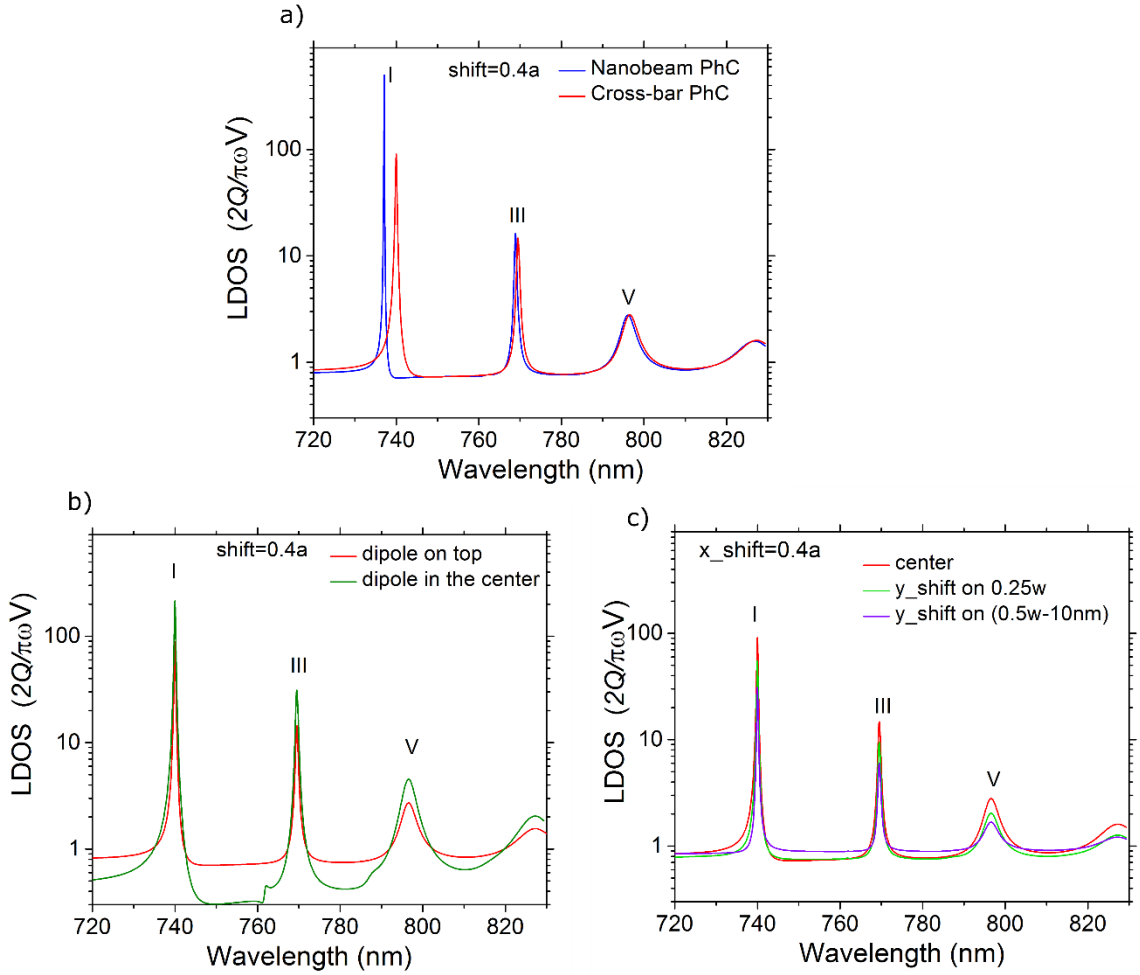

Fig. 5.26. a) Simulated LDOS enhancement of emitted light from the dipole placed on top of the cavity region of freestanding cross-bar (red curve) and Nanobeam (blue curve) freestanding PhC cavities with identical parameters. **b)** Simulated LDOS enhancement of emitted light from the dipole placed on top of cavity (red curve) and inside in the center of the cavity (green curve) of freestanding cross-bar PhC cavity **c)** Simulated LDOS enhancement of emitted light from the dipole placed on top of freestanding cross-bar PhC cavity in the center of the nanoguide (red curve), shifted along y-direction on 0.25w=112.5nm (light green curve) and shifted along y-direction on 0.5w-10nm=215nm (violet curve), where w - width of the waveguide.
In all considered simulations in this figure the dipole was shifted on optimized distance 0.4a along x-axis.
Freestanding cross-bar PhC cavity has the following parameters: cavity length 195nm, first three segments from each side of cavity are identical with $ff = 0.30$, next N=15 segments quadratic tapered between $ff_f = 0.30$ and $ff_i = 0.16$ counting from the center, periodicity $a = 280nm$.

Considerations related with experimental coupling of the dipole into PhC cavity

To sum up, according to the performed simulations to achieve maximum enhancement factor of emitted light coupled into the first resonance mode with target computed and, in fact measured wavelength 738nm, the dipole should be shifted on *0.4a* along longitudinal direction from the symmetry plane from the center of the cavity (position 5 on Fig. 5.25).

It should be noted, that fabricated freestanding cross-bar PhC devices consist N=43

mirror segments from each side of cavity, leading to drastic increase of *Q*-factor and, so of LDOS enhancement factor, in comparison with computed enhancement for PhC cavity with N=15. LDOS enhancement for fabricated and characterized PhC cavity with higher number of holes can be evaluated from its measured *Q*-factor, simulated mode volume and comparison with LDOS enhancement of light coupled to the same order resonance mode of identical PhC cavity with smaller number of holes N (knowing simulated Q and mode volume of this PhC as well). At the same time, it should be taken into account, that placement of the emitter is still challenging task, therefore slight displacement of the position from optimized one, and as a consequence decrease in enhancement factor, should be expected. This reduction can be evaluated from relations of LDOS enhancements for different positions of the dipole along each axis (Fig. 5.25, 5.26). Furthermore, it should be highlighted, that LDOS enhancement spectrum was computed for the case when the polarization of the source perfectly aligned with major field of TE-like resonance modes (E_y), however in reality the discrepancy related with positioning and alignment of the emitter in respect to the polarization of the resonance modes will decrease enhancement factor.

5.2.3 Simulation of β-factor coupling efficiency of emitter in cross-bar PhC cavity

β-factor characterizes probability of coupling of emitted photon into waveguide mode, thus it strongly depends on spatial position of the source on PhC due to LDOS enhancement factor. Coupling efficiency correlates with LDOS factor, *i.e.* β-factor can be enhanced in case of coupling into resonance mode or inhibited when LDOS enhancement is suppressed (in bandgap and off-resonance case).

β-factor can be extracted as the ratio between the Poynting vector flux through PhC cavity and the overall radiated power of the source.

To determine β-factor coupling into waveguide mode of PhC cavity it was performed FDTD simulations using MEEP software, resulting in β-factor spectrum, where transmission coupling efficiency into each resonance mode of PhC cavity can be tracked. Broadband Gaussian pulse point-dipole with major field component of the dipole E_y perfectly aligned with polarization of resonance modes was placed in the interested position on top of the cavity to excite TE-like resonance modes. Overall radiated power was derived as Poynting's vector flux over a closed surface around dipole. Namely it was positioned six detector planes around the dipole and accumulated Fourier transforms of electric E_y and magnetic H_z field components in every detector plane for every point via summation over time steps, and at the end of run time Poynting flux spectrum was computed. β-factor simulation of PhC cavity is time-consuming since it is needed to run the computation until the localized modes decayed out from the cavity region.

To register fraction of radiated light coupled to resonance mode and further coupled to waveguide mode, it was placed detector planes at the two ends of PhC cavity, which detect Poynting vector flux transmitted through PhC cavity.

Simulated β-factor spectrum of probability of coupling emitted light from the dipole into resonance mode and further to waveguide modes is shown in Fig. 5.25. The dipole was positioned on top of freestanding cross-bar PhC cavity (explored in the Chapter 5.2) and shifted on 0.4a in the longitudinal direction from the center of symmetry where LDOS enhancement, so Purcell enhancement factor, is maximized, as was determined in Paragraph 5.2.2.
To evaluate enhancement of coupling into resonance modes (and further in corresponding longitudinal waveguide modes of PhC) it was also computed β-factor spectrum transmission coupling efficiency into waveguide mode of identical geometry cross-bar waveguide without PhC (without drilled holes), the results is shown as dashed green line in Fig. 5.27 a). To understand origin of β-factor values Transmission spectrum of considered cross-bar PhC cavity (Fig. 5.27 b)) and LDOS enhancement spectrum for considered position of the dipole (Fig. 5.27 c)) are shown.

From the analysis of these graphs the following notations can be made:

- LDOS enhancement and Transmission values determine β-factor for certain resonance mode. Thus, however transmission of I-order resonance mode is low - 28%, LDOS enhancement reaches 41, this all leads to $\beta=60\%$, where in case of III-order mode enhancement is low (≈ 3), but transmission is high (93%), resulting in $\beta=73\%$.
- Obviously, β-factor coupling of emitted light into cavity of considered PhC cavity is higher in comparison with coupling efficiency into guided mode of identical cross-bar structure without drilled holes, due to Purcell enhancement. Thus, β-factor coupling into fundamental resonance mode on 20% higher than coupling into nanoguide mode.

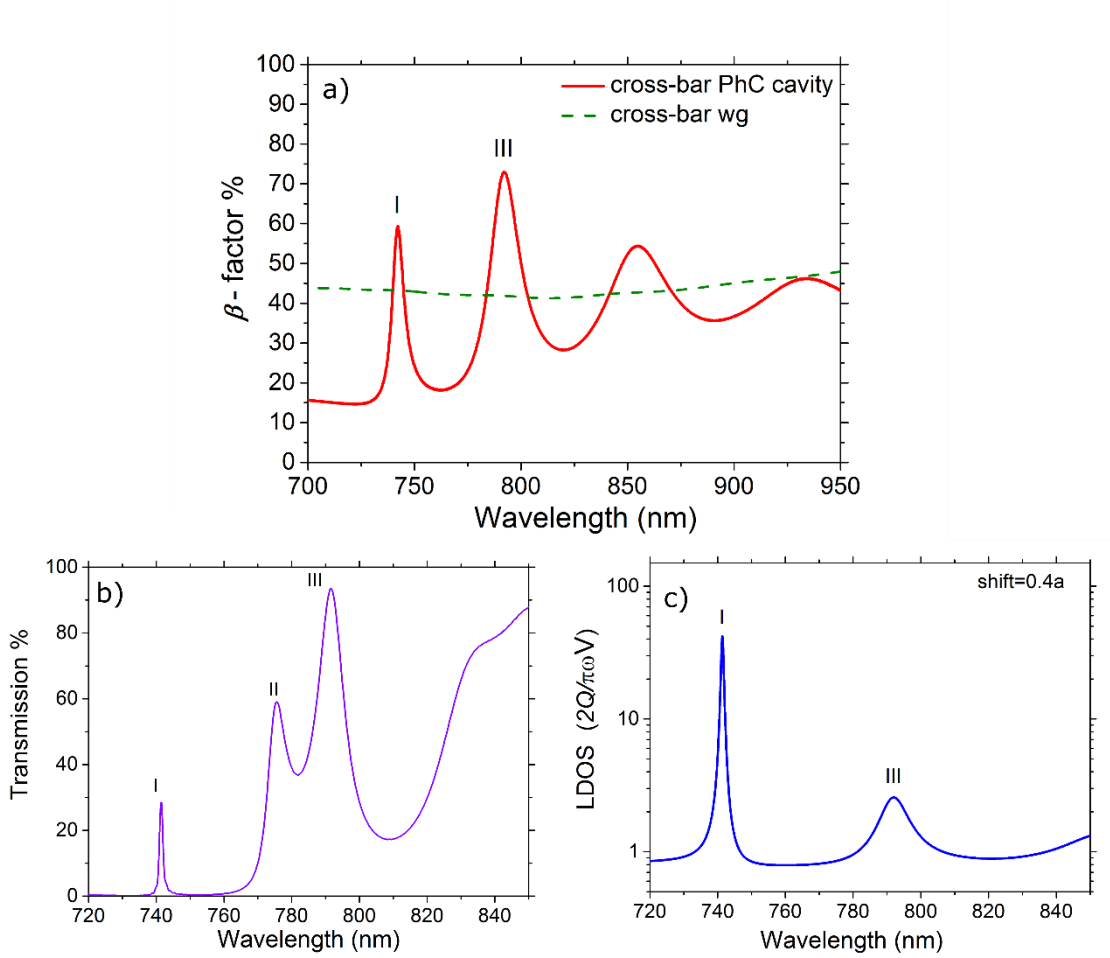

Figure 5.27. a) Simulated β-factor transmission coupling efficiency of emitted light into resonance modes and further longitudinal guided modes of freestanding cross-bar PhC cavity for the dipole positioned on top of the cavity region and shifted on 0.4a away from symmetry plane along PhC. Dashed line shows β -factor efficiency of coupling emitted light into waveguide mode for identical geometry cross-bar freestanding waveguide. **b)** Simulated Transmission spectrum through considered cross-bar PhC cavity. **c)** Simulated LDOS enhancement spectrum of emitted light from the considered dipole.
Simulated freestanding cross-bar PhC cavity has the following parameters: cavity length 195nm, first three segments from each side of cavity are identical with $ff = 0.30$, next N=7 segments quadratic tapered from $ff_f = 0.30$ to $ff_l = 0.16$ counting from the center, periodicity $a = 280nm$.

5.3 Concluding remarks

It was designed, fabricated, experimentally and via simulations fully investigated *novel* 1D freestanding *cross-bar* PhC cavity integrated on chip, which ensure spatial separation excitation and enhanced emitted light for coupled remitter on the cavity region. Measured cross-talk is -20 dB, in other words such structure provides 20 dB extra filtration of pump light. Computation and measurement results were in agreement. It was optimized geometry structure parameters of PhC cavity based on simulation and measurement results, in particular optimized length of cavity (195 nm) gives drastic rise of Q-factor with max measured value $Q = 47 * 10^3$, while simulation value is $Q = 51 * 10^3$.

Determined electric, magnetic fields, Poynting vector flux and Energy distributions of resonance modes localized in the cavity was the first indication of optimize positioning emitter inside the cavity, while the next step − computation of LDOS enhancement spatial map defines precisely optimal positions of the single photon source to couple effectively into certain resonance modes localized in the cavity. Moreover, measured Q, simulated mode volume allows to evaluate enhancement factor for any position of the source on the cavity region for PhC cavity with big number of holes, which direct numerical computation is highly time-consuming. Evaluation of enhancement factor can be done by comparison with LDOS enhancement maps for identical PhC cavity with lower number of holes, which was characterized (Q, mode Volume) via simulations.

Further performed transmission coupling efficiency into cavity mode (β-factor) simulations proved optimized positions of the dipole found from LDOS computation, thus maximum coupling efficiency into required resonance mode and further in corresponding longitudinal guided mode was determined.

Designed PhC cavity devices on chip will be further employed to couple single photon emitter (SiV) into frequency matched fundamental resonance mode (738nm). The source ideally should be shifted on around half of the period (precisely 0.4a) and aligned with TE-polarized resonance mode, in order to achieve maximum enhancement of emission rate via Purcell effect, where according to performed simulations LDOS enhancement obtains 41 for PhC cavity with just 10 mirror segments from both sides of cavity region. Thus, transmission coupling efficiency into employed resonance mode obtains 60%.

It should be noted that higher order odd resonance modes with antinodes of electric field in the cavity region can be as well employed to couple emitted light from vibronic bands of NDs. In particular, for third order mode LDOS enhancement factor equals 3 was computed, yielding in higher $\beta = 73\%$.

6. Coupling of nonclassical light from DBT molecule into Si_3N_4 circuit on-chip

Direct coupling of single photon emitter to single-mode waveguide on chip is favorable for realizing integrated quantum photonic circuits [112][113]. Long-distance quantum communication requires coupling of single photon emission into tight propagating optical modes of optical fibers or of integrated photonic elements on chip. In this Chapter it is shown one of the first demonstrations of coupling single DBT molecule into ridge Si_3N_4 waveguide via evanescent coupling, where apodized grating couplers were employed as output ports of the waveguide for detection single photons emitted from the molecule at room temperature.

Dibenzoterrylene (DBT) is dye molecule. DBT is a photostable single photon source in the near infrared at room and at low temperature, DBT has almost unitary quantum yield [25], negligible blinking limited by the intersystem crossing yield to the short-lived triplet state [26]. In order to protect molecule against oxidization DBT was embedded in host matrix – Anthracene crystal (DBT:Ac) which increases photostability of the molecule up to emitting 10^{12} photons before photobleaching [27]. Moreover, crystalline host matrix makes possible to control the distance between DBT and waveguide, optimization of this parameter increases coupling efficiency of the emitted light into waveguide mode via evanescent coupling, also molecules, which are embedded in host matrix, can be easily spincoated on the chip. Overall, this all makes DBT a promising single photon source for integration it within nanophotonic circuit, where Si_3N_4 is a solid candidate for waveguide material to carry optical mode in the visible range.

Experimental measurements for the realization coupling single DBT molecule into hybrid nanophotonic circuits were performed in European Laboratory of Nonlinear Spectroscopy (LENS, University of Florence) by me together with Dr. Pietro Lombardi under the supervision of Dr. Costanza Toninelli during my half-a-year scientific work in Florence as a part of Erasmus Mundus Europhotonics PhD Program.

6.1 Investigation DBT:Ac

This paragraph focused on the characterization of DBT molecule independently from nanophotonic device, whereas the topic of Paragraph 6.2 is integration DBT into the photonic circuit.

6.1.1 Optical experimental setup based on an epi-fluorescence microscope

In current work it was used epi-fluorescence setup to investigate DBT:Ac, where excitation and detection of light was performed through the same objective, whereas pump light was filtered out using long-pass filters. The experimental setup which was used to characterize molecules spincoated on the glass and further coupled to nanophotonic devices, investigated in the Paragraph 6.2, is depicted on Fig. 6.1. Several types of laser sources: continuous wave (CW) $\lambda = 767nm$ excitation laser, CW $\lambda = 785nm$ diod laser to perform transmission measurements, Ti:Sa pulsed laser to perform lifetime measurement, were employed depending on the performed type of measurement.

For studying DBT:Ac spincoated on the glass slide it was used oil-immersion objective to increase numerical aperture (NA=1.4), while for excitation and collection outcoupled fluorescence from nanophotonic device it was inserted air objective (NA=0.55), due to required longer focal length, since molecules integrated in nanophotonic device were illuminated from the backside of the chip with thickness ≈ 525 um. The system allows 100um field of view, whereas investigated chip was mounted on three-axis piezo-positioner allowing scanning the sample. In detection path the setup was equipped with an electron-multiplied charged-coupled device (EMCCD) for imaging and a spectrometer for spectral analysis. To perform second order correlation and lifetime measurements as well as to acquire fluorescence maps it was utilized a couple of single photon avalanche photodiodes (SPADs), where for the first task SPADs were arranged in Hanbury Brown and Twiss (HBT) scheme [75]. To block excitation light it was inserted long-pass filters in the detection path.

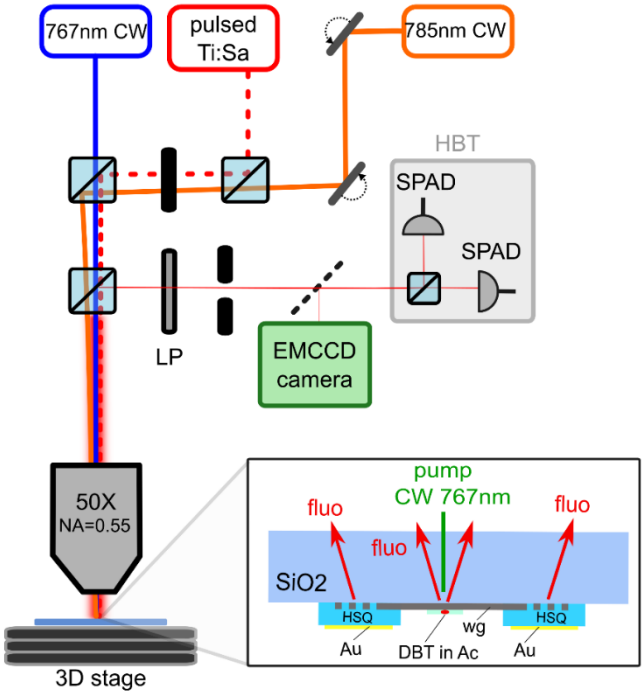

Figure 6.1. Optical scheme of epi-fluorescence setup. Inset panel displays sketch of the excitation of DBT:Ac integrated to the photonic device on the chip.

6.1.2 DBT: Ac sample characterization

To characterize molecules at room temperature solution of DBT embedded in Ac was spin-coated on top of the microscope glass slide. To prepare molecule doped crystals DBT solution was dissolved in toluene to achieve a 1 mM solution and then more diluted in the mixture of Ac/diethyl ether (concentration of 2.5 mg/Ml) by a factor of 10^6–10^8.

By inserting wide-field lens in the excitation path of epi-fluorescence microscope (Fig. 6.1), CW pump beam (767 nm) is focused onto the objective back-aperture yielding a wider area of illumination, so called 'wide-filed illumination' to characterize several DBTs embedded in one Ac crystal as depicted in Fig. 6.2 a), b). Hence, fluorescence light from individual DBT molecule can be distinguished (white spots on b)). Measured red-shifted fluorescence spectrum of DBT:Ac is shown in Fig. 6.2 c), it has max on 790 nm and wide bandwidth ≈ 50 nm, since spontaneous decay terminates on different vibrational levels of ground state of DBT. The left side of the spectrum is cut by inserted long-pass filters of pump light, whereas on the longer wavelength range detected fluorescence spectrum intensity decreases due to lower detection efficiency of the spectrometer.

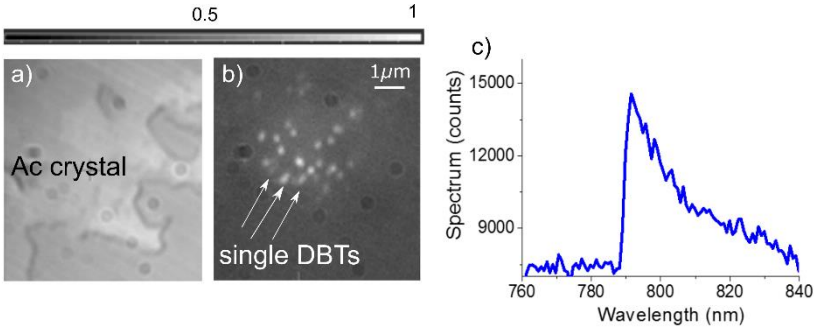

Figure 6.2. a) CCD image of thin 50nm Ac film with embedded DBTs spincoated on glass slide. **b**) Wide-field CCD image of DBT:Ac, where fluorescence from individual molecules can be distinguished (white spots). **c)** Measured spectrum of fluorescence light of DBT:Ac.

The molecules are embedded in host matrix, therefore their orientation is fixed. By changing polarization of the excitation light by means of rotation half-wave plate, which was inserted after polarizing cube in the excitation arm, certain molecules can be excited – switched on, since most of the observed DBTs on Fig. 6.2 b) are embedded in one Ac crystal and thereby aligned similarly. When the polarization of excitation light is aligned with polarization of the molecule (Fig. 6.3 a), d)) emitted red-shifted fluorescence of molecule is maximized, while with increasing misalignment between them (rotation of polarization of excitation light on 90°) fluorescence signal decreases as shown in Fig. 6.3 b).

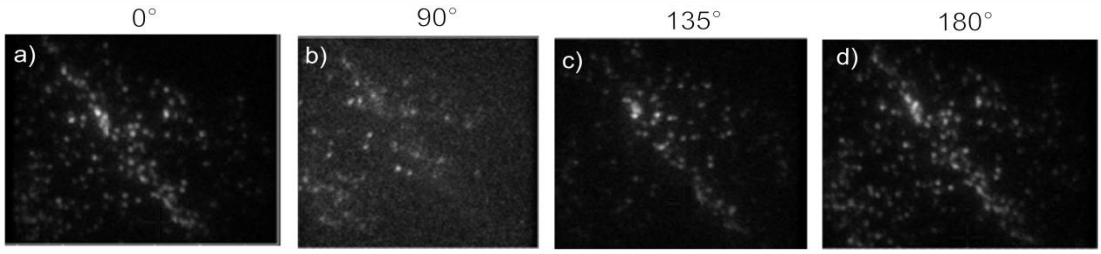

Figure 6.3. DBT's fluorescence intensity dependence on the polarization of the excitation light, numbers indicate rotation angle of the polarization of pump light.

6.1.3 Photon-correlation measurement of single DBT

To perform single photon measurements under CW excitation two main requirements should be satisfied:

1. *selection single DBT molecule*.
   For spatial isolation of single molecule it should be ensured that there is only one molecule in the laser excitation spot. This can be achieved by decreasing concentration of DBT in Ac. Switching from wide-field illumination to confocal illumination diffraction-limited spot can be excited, where polarization of pump light can be tuned to align it with the studied

molecule. By inserting pin-hole in the detection path scattered light as well as fluorescence emission from neighbor emitters can be cut.
Spectral selection of the emitted fluorescence light is achieved by inserting long pass filters into detection path to cut excitation light.

2. *Efficient collection of fluorescence emission from single molecule* is achieved by employing objective with high NA as well as using SPADs with high detection efficiency, low dark count and low after-pulse probability.

Spatially selected molecule was excited with CW laser 767 nm at room temperature, where spectrally selected emitted fluorescence signal was directed into two SPADs, which were arranged in HBT scheme (Fig. 6.1). Second–order correlation measurement showed a pronounced dip in the coincidence histogram (black curve on Fig. 6.4) where it was fitted by the following function (red curve):

$$g^{(2)}(\tau) = 1 - a * exp\left(-\frac{|\tau|}{\tau_{DBT}}\right) \qquad (35),$$

where τ_{DBT} – lifetime of the molecule which characterized by spontaneous emission rate, a – dip depth, τ – delay.

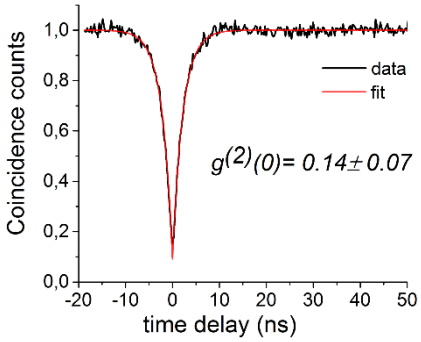

Figure 6.4. Measured antibunching dip in the fluorescence light from single DBT:Ac as an evidence of single-photon emission.

Pronounced antibunching dip with the depth $a = 0.86$ at zero delay was observed, which is the signature of single photon emission. The performed experiment verified the single molecule concentration of prepared and employed solution of DBT:Ac, and also proved that there is no corruption of molecules. Thus, prepared single DBT:Ac solution was further employed in the next experiment, investigated in Chapter 6.2.

6.2 Integration single DBT:Ac in Si_3N_4 circuit on-chip

6.2.1 Design of the chip and fabrication technique

The aim of the work was to couple DBT:Ac into the photonic device, and employ apodized grating couplers as output ports of the ridge Si_3N_4 waveguide (WG) for detection single photons emitted from single molecule at room temperature. Model of *hybrid nanophotonic device* is shown in Fig. 6.5, where mirror-enhanced grating couplers were employed in order to increase outcoupling efficiency by redirecting diffracted toward air light to downward (collection) direction (subject of Paragraph 6.2.2). Namely, grating couplers are fully etched to the bottom silicon dioxide layer, buried in a 760-nm-thick hydrogen silsequioxane (HSQ) buffer layer with a 120-nm-thick gold mirrors on top.

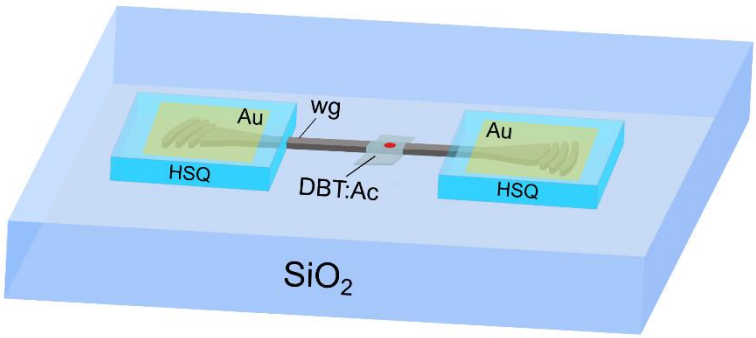

Figure 6.5. Model of hybrid nanophotonic device with integrated single-photon DBT molecule (red point) embedded in Ac crystal (grey layer).

It was employed Si_3N_4 as a waveguide material as a promising platform for integrated photonics applications, precisely silicon nitride provides broadband optical transparency covering the entire visible range up to the near infrared spectrum [87]. Refractive index contrast of Si_3N_4 on SiO_2 is not as high as for silicon-on-insulator (SOI), which reduces scattering losses and increase tolerance to the fabrication imperfections.

Thus, to experimentally realize the devices we employ silicon nitride-on-insulator wafers consisting of 175 nm stoichiometric Si_3N_4 on top of glass. Fabrication of the nanophotonic circuits was carried out using several steps of electron-beam lithography (e-beam).

1. In the first e-beam step the nanophotonic circuits were defined on top of Si_3N_4 layer in ma-N 2403 negative photoresist, then developed 1 min in MF-319 (ingredients: water: 97-98%. Tetramethylammonium hydroxide: 2.45%), following reflow process – heating the chip 2 minutes on hot plate at 100°C. After, devices were dry-etched into the

silicon nitride layer using a CHF_3/O_2 plasma. Photoresist was subsequently removed in O_2 plasma.

2. During the second electron-beam lithography step protective HSQ layer was defined on top of grating couplers by means of e-beam lithography of spincoated HSQ negative photoresist and subsequent development step in MF-319.
3. In the third step, gold mirrors on top of grating couplers were produced by means of e-beam writing positive PMMA mask with subsequent development it in the solution of Methylisobutylketon (MIBK) and Isopropanol (IPA) MIBK:IPA=1:3, and further evaporation of 10 nm Cr layer, utilized as an adhesion layer, and 120 nm gold layer; after that lift-off process in Acetone was performed to remove unexposed PMMA with metal layer on top.

Alignment on fully-etched global markers, prepared in the first e-beam step, was performed during the next fabrication steps. Thus, by employing this fabrication technique it is possible to produce hundreds of nanophotonic devices on the chip.

The parameters of Si_3N_4 waveguide were verified via simulations in COMSOL [44] software for single-TE-like mode operation around ZPL of DBT – 785 nm: width of the waveguide is 500 nm, while the thickness is predefined by the wafer 175 nm. Simulated electric filed distribution of TE-like mode (Fig. 6.6 e)) in the waveguide yields in $n_{eff} = 1.551$.

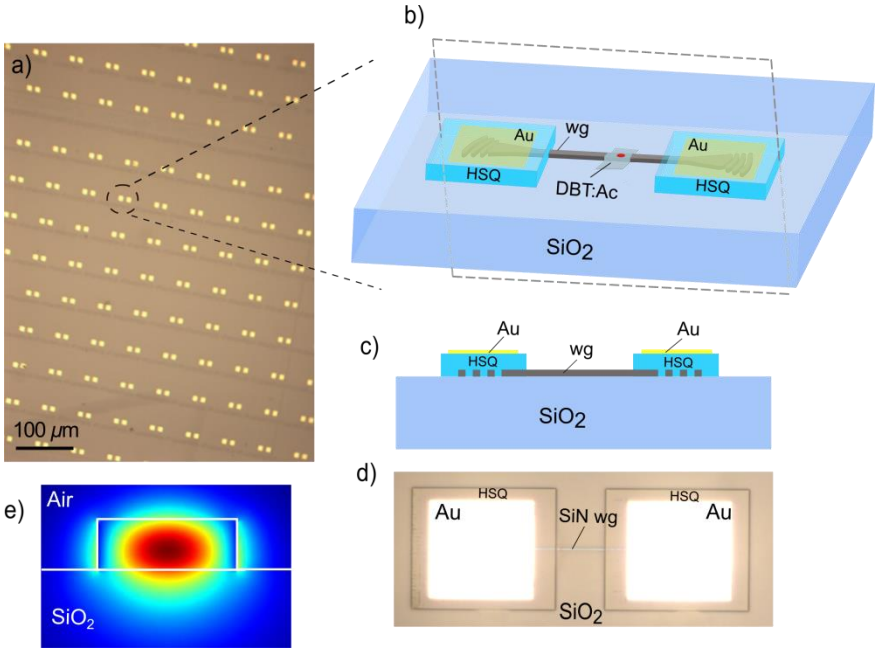

Figure 6.6. a) Optical image of part of the chip with array of nanophotonic devices. **b)** Model of hybrid nanophotonic device with integrated DBT:Ac, where dashed grey contour represents section **(c)**. **d)** Optical micrograph of fully-etched nanophotonic device. **e)** Cross-section of the waveguide with carried fundamental TE0 mode at $\lambda = 785\ nm$.

6.2.2 Mirror enhanced grating couplers to read out single photons

To couple light into and out to the photonic device it was utilized grating couplers. Models of grating coupler buried in SiO_2 and mirror-enhanced grating coupler are depicted in Fig. 6.7 a), b), respectively, with cross-sections shown in Fig. 6.7 c), d). Optical power is coupled in or out due to diffraction of light from every teeth of coupler during propagation. Theoretically in case of infinite grating this results in an exponentially decaying diffracted planewave profile (Fig. 6.7 e)), therefore one of the aims during designing of coupler was to match the output diffracted mode with a gaussian-like free-space mode, which can be achieved by optimization tapering length and filling fraction recipe. Filling factor ff is defined as the ratio of the remaining grating width *b* to the grating period *a*.

Another important characteristic is period of teeth *a*: by tuning period diffracted central wavelength is shifted, this the relation is linear as was experimentally shown in Fig. 2.4 in Paragraph 2.1.2, therefore by properly choosing grating period for desired λ=785 nm (ZPL of DBT), taking into account $n_{Si_3N_4}(785\text{nm}) = 2.02$ and refractive index top cladding (HSQ) $n_{clad}(785\text{nm}) = 1.45$ it was realized grating coupler which diffracts light in only one - first order ($m = 1$) with input coupling angle θ=8° through the glass substrate, so $\theta_{in} = 11.6°$ in air ((6) in Paragraph 2.1.2).

Coupling efficiency in considered case on Fig. 6.7 e) can be calculated as a power diffracted from the grating coupler versus the total power emitted by the light source:

$$\eta_{coup\_eff} = {P_{down}}/{P_{wg}} = \eta_{direct} * \eta_{mode\_overlap}. \quad (36)$$

Thus, coupling efficiency is determined mainly on these two factors [115]:
1. directionality η_{direct} – ratio of the optical power diffracted down in our case, which further collected with objective, and total power which diffracted out.
2. The mode matching $\eta_{mode\_overlap}$ limited by the maximum overlap integral value between an exponentially decaying field profile and the outcoupled free-space gaussian profile.

In order to enhance directionality namely to redirect downward light, which was diffracted toward air, it was deposited a gold layer-mirror on top of the grating. In between grating and mirror there is 760-nm-thick HSQ buffer layer, which is by optical characteristics identical to SiO_2 layer (Fig. 6.8).

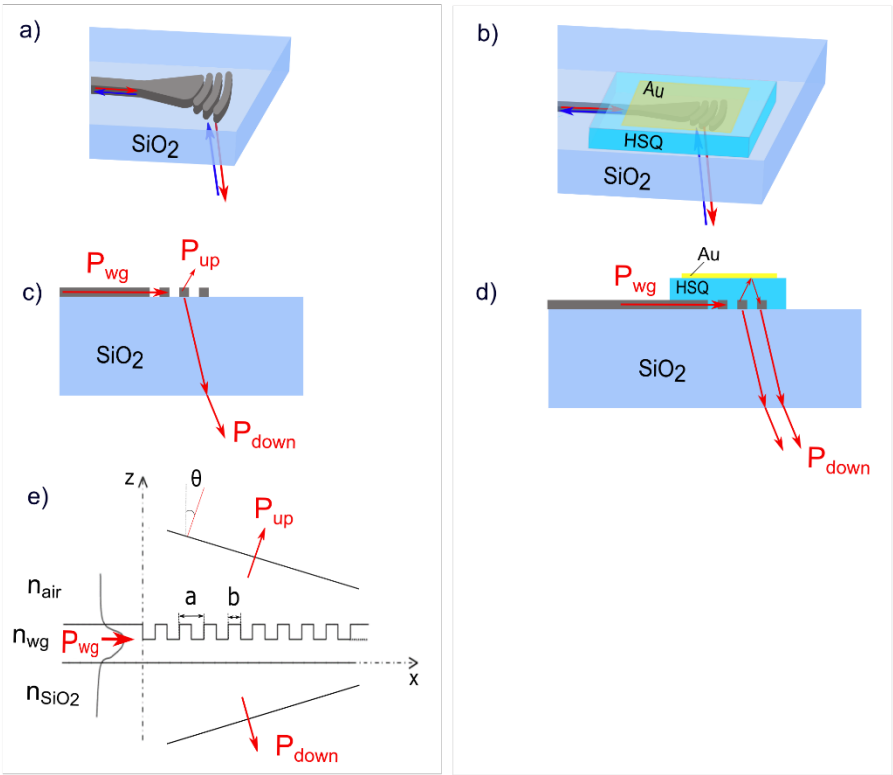

Figure 6.7. **a)** Schematic design of Si_3N_4 grating coupler buried in SiO_2 with top cladding – air. **b)** Schematic design of mirror-enhanced grating coupler. 2D lateral view of the grating coupler along the propagation axis without HSQ **(c)** and with HSQ buffer layer and gold mirror **(d)**. **e)** Sketch of the operation principle of one-dimensional grating coupler.

It was important to optimize the distance between mirror and the grating, *i.e.* thickness of HSQ, to ensure constructive interference toward the glass, namely between fields reflected from the edge Si_3N_4-HSQ, HSQ-gold and Si_3N_4-SiO_2 (diffracted directly downward). This was performed through finite element simulations [10]. Indeed, HSQ cladding also prevents foundation of Ac crystal in the grating coupler areas.

Apodization recipe of grating coupler was produced to match the free space output mode with the laser quasi-Gaussian profile, which also improves symmetry of the longitudinal profile; after it tapering length was optimized yielding in 4.5 µm, so that the transverse size of the mode equals to the longitudinal.

Optimization the distance between mirror and the grating, and creation of Apodization recipe of grating coupler *was performed by Dr. P. Lombardi (LENS, Florence) during our collaboration on this project.*

Optimized grating coupler configuration yields to the computed (simulated) output coupling efficiency η_{coup_eff} of up to 90%, which reduces to around 60% adapted to our fabrication

constraints related with slight deviation of thickness of HSQ layer from simulated once and also influence of extra 10nm chromium adhesion layer [10].

In order to characterize devices on the chip, in particular coupling efficiency, transmission measurements were performed. CW light on 785 nm, which corresponds to ZPL of DBT:Ac, was coupled through left coupler, light propagates through the waveguide and coupled out through right coupler (Fig. 6.8 a)) was collected by the imaging system shown in Fig. 6.1.

The signal was integrated over the coupler area and normalized to the reflection from a silver mirror (after background subtraction on both images). Transmission spectrum through several photonic devices depicted in Fig. 6.8 d).

It should be noted that coupling angle of the input beam was also varied to determine grating coupler with the highest transmission on ZPL of DBT – 785 nm, therefore changing the period of grating coupler was compensated by tuning the input angle, so that central outcoupled wavelength was not shifted (fixed on 785 nm). Bandwidth of the couplers transmission is ≈ 50 nm.

The single coupler efficiency was calculated as the square root of the transmission. The averaged measured coupling efficiency yields to $\eta_{coup\_eff} = 35 \pm 5\%$.

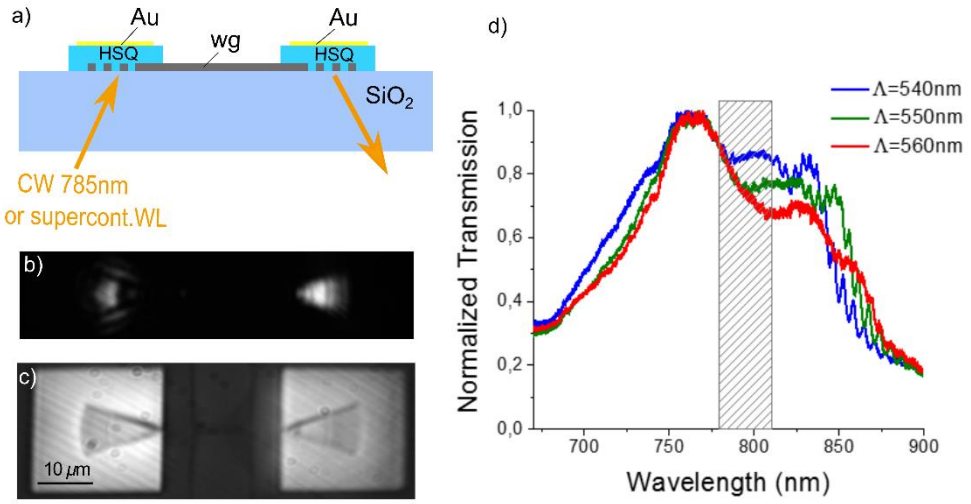

Figure 6.8. **a)** Schematic design of Transmission measurement of Si_3N_4 photonic device buried in SiO_2. **b)** CCD image of transmitted signal. **c)** Micrograph of fabricated nanophotonic device. **d)** Normalized transmission spectrum of the nanophotonic devices equipped with grating couplers with different periods labeled in the legend. Shaded region corresponds to fluorescence spectrum of DBT at room temperature.

As were mentioned before this mismatch between measured value and simulated can be related with non-optimal HSQ thickness as well as 10 nm adhesion layer of Chromium underneath gold mirror on the chip. This value is almost 3 times higher compare with coupling efficiency of apodized grating coupler without gold mirror, which proved the fact that such configuration improves outcoupling strength.
Moreover, measured spot-intensity profile of retro-reflected of laser spot from silver mirror placed in the position of the chip (purple curve on Fig. 6.9), which corresponds to free-space Gaussian-like mode, and diffracted signal from coupler (blue curve on Fig. 6.9) match each other in terms of size and envelope in both longitudinal and transverse directions.

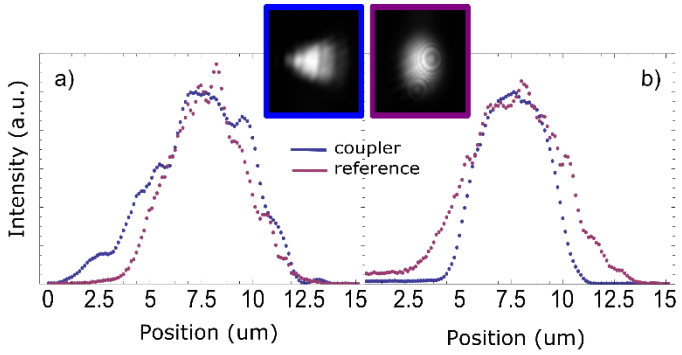

Figure 6.9. Longitudinal **(a)** and transverse **(b)** intensity profile of diffracted light measured for the grating coupler output with FWHM≃4 μm (blue dots) and for the retro-reflection of the laser spot (purple dots). Insets show CCD image of transmitted signal by grating coupler (in blue frame) and retro-reflected signal (in purple frame).

Based on the measured profiles of the two modes, overlap integral was evaluated higher than 0.9, which proves that the parameters of fabricated grating coupler were optimized correctly during the computation step. It should be also noted, that reproducibility of transmission through devices on the chip is high. Propagation loss of waveguide is 4.9 dB/mm at λ=766nm.

6.2.3 Hybrid system: molecule-on-photonic device

Hybrid molecule-on-photonic device system, where single photon emission from DBT:Ac molecule was coupled into Si_3N_4 waveguide at room temperature, is demonstrated in this Thesis.
Molecule solution, which was investigated in beforehand experiment described in Paragraph 6.1, was spin-coated on the photonic chip, forming thin layer of DBT:Ac. In the single-photon experiment molecules existed in the vicinity of the waveguides were excited under CW pump light (767 nm), where emitted fluorescence tail was coupled into guided mode, as illustrated on Fig. 6.10.

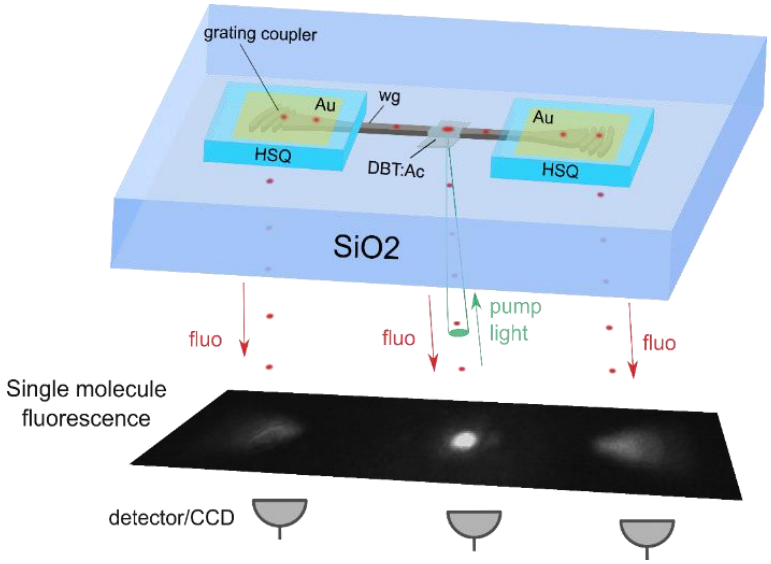

Figure 6.10. Hybrid single-molecule photonic device operation principle. On the panel below: EMCCD image of emitted fluorescence from entire device under direct confocal excitation of single molecule coupled to Si_3N_4 waveguide.

First Experiment

In the first experiments CW pump light on 767 nm from diode laser was coupled to the waveguide through the left grating coupler as sketched on Fig. 6.11 a). Molecules can be efficiently excited in the close proximity of the Si_3N_4 waveguide by the evanescent tail of the guided pump light. The emitted fluorescence partly couples into the waveguide mode and propagates in the direction of both grating couplers.

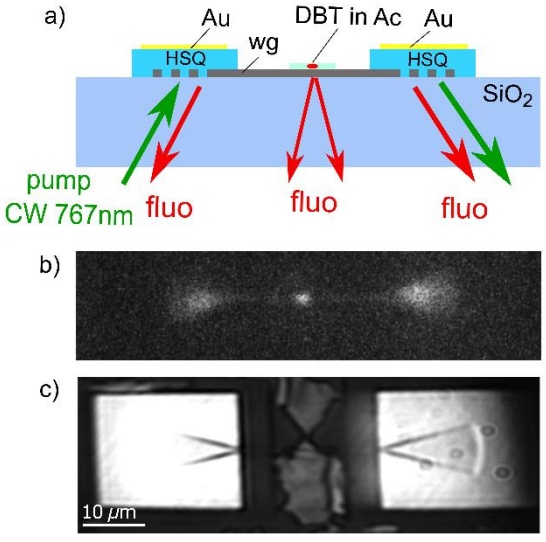

Figure 6.11. a) Excitation scheme of DBT:Ac coupled to waveguide mode. **b)** EMCCD image of fluorescence emitted from nanophotonic device. **c)** White light image of investigated nanophotonic device.

Outcoupled light from the device in free-space was directed to EMCCD after filtration excitation light by long-pass filters. Outcoupled fluorescence light from grating couplers shown in Fig. 6.11 b) was the first demonstration of coupling emission light from DBT into waveguide mode.

Second Experiment

In the second round of experiments to ensure better isolation DBT's fluorescence and excitation light beams were spatially separated by direct confocal excitation the molecule through SiO_2 substrate, where collection of coupled guided mode fluorescence light was performed via both grating couplers.

As a first step in this experiment the area around waveguide was scanned confocally to study spatial distribution of molecules, where fluorescence signal from the same spot was detected by SPAD.

The next goal was to prove that detected outcoupled signal is exactly emitted fluorescence. This was verified by constructing fluorescence map, which was recorded during confocal scan with excitation of the area around waveguide, and at the same time by tracking fluorescence spatial distribution at the grating coupler area. Fluorescence map of one of the investigated devices is shown in Fig. 6.12 b). White-shaded rectangle labels the underlying Si_3N_4 waveguide. Bright regions on and around waveguide corresponding to fluorescence emitted from molecules can be distinguished.

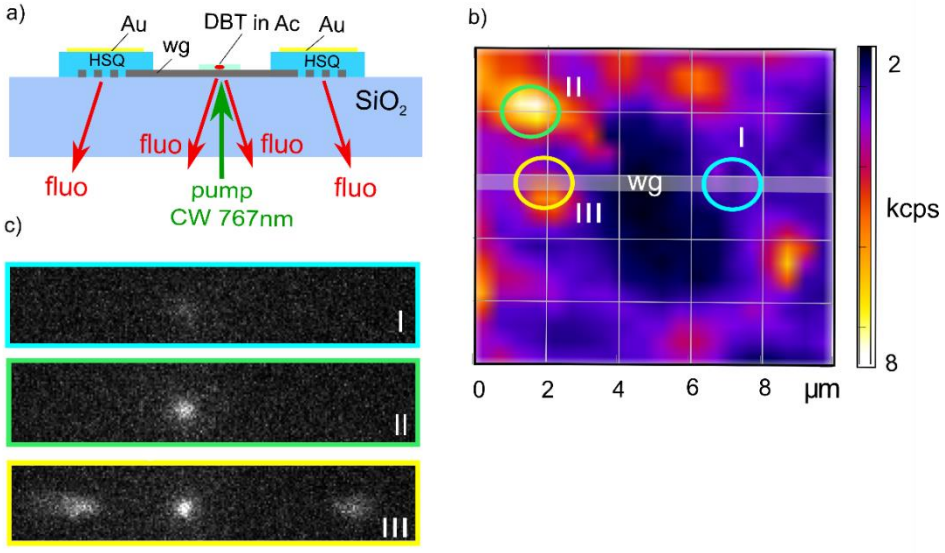

Figure 6.12. DBT:Ac-waveguide coupled fluorescence. **a)** Sketch of the excitation and collection measurement of nanophotonic device. **b)** Confocal fluorescence map acquired around Si_3N_4 waveguide (white underlying rectangular). **c)** EMCCD images of emitted fluorescence from nanophotonic device while direct confocal excitation point I on the waveguide shown on panel (I), molecule II shown on panel II, molecule III coupled to waveguide mode shown on panel III, respectively.

In the three panels in Fig. 6.12 c) the fluorescence spatial distribution from the entire photonic device is compared for two positions of excited molecules: II – molecule sitting far from waveguide, III – molecule is in near-field of waveguide. It is obvious, that the output couplers light up if and only if DBT in the vicinity of the waveguide is excited, and fluorescence light coupled to the waveguide mode, as can be seen in fluorescence image panel III in Fig. 6.12 c). This indicates that direct scattering between illuminated confocal spot and grating coupler is negligible, as can be seen on panel II in Fig. 6.12 c). Panel I represents the background signal collected by illuminating an empty crystal without DBT on the waveguide. A small amount of residual light exists on the illumination point (panel I) might be related to some remaining fluorescence from the anthracene crystal, it is around five times smaller than the signal from a single DBT molecule.

It should be noted that fluorescence signal from confocal point for molecule II is stronger than for molecule III, as can be seen on fluorescence map Fig. 6.12 b) in comparison with EMCCD images. In order to excite molecule III more effectively, which with higher probability can couple into the waveguide mode, since it is positioned in the near-filed, it was adjusted the polarization of pump light to be aligned with the polarization of molecule III, resulting in maximum possible emitted fluorescence light, and then again re-optimized to match the polarization of outcoupled light from grating couplers during the next scan to effectively collect fluorescence light, as shown on panel III and EMCCD images in Fig. 6.12. Since the difference between polarization angle was less than 20°, confocal fluorescence signal from the molecule on panel III is brighter than on the panel II in Fig. 6.12 c). *DBT-waveguide coupling efficiency* was estimated from EMCCD image on panel III, yielding in 24%, which will be discussed in Paragraph 6.2.5 taking into account previously determined via transmission measurements coupling efficiency of one grating coupler $25\% \pm 2\%$ in this device.

6.2.4 Analyzation of Quantum Nature of DBT-WG-coupled light

The next goal was to prove quantum nature of the WG-coupled light by measuring photon statistics arranged in Hanbury Brown and Twiss setup (Fig. 6.1). Measured second-order autcorrelation functions $g^{(2)}(\tau)$ are plotted in Fig. 6.13 c), d) for fluorescence photons collected both directly from the position of the molecule and also for photons diffracted at grating coupler, respectively, as indicated with the circled area on CCD image (Fig. 6.13 b)).

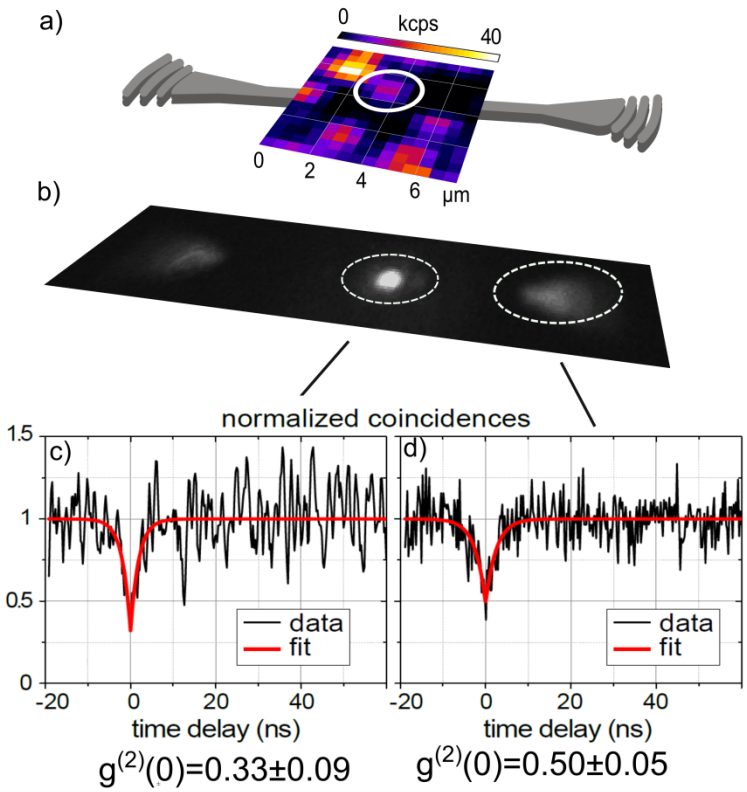

Figure 6.13. Single DBT:Ac integrated in nanophotonic device. **a)** Nanophotonic Si_3N_4 device with superimposed fluorescence confocal map, white circle shows molecule coupled into the waveguide mode. **b)** EMCCD image of fluorescence signal outcoupled from confocal point and grating coupler (dashed circles). **c)** Measured second-order correlation function from confocal point and from **(d)** grating coupler. Antibunching dip is the first evidence of coupling nonclassical light into the waveguide mode.

Measurement of correlation function at the coupler region was performed by increasing the size and shifting spatial filter (pinhole) with respect to the confocal point as well as both detectors. The fluorescence map shown in Fig. 6.13 a) of considered device was described in Paragraph 6.2.3.

Measured histograms $g^{(2)}(\tau)$ (black dots in Fig. 6.13 c), d)) are presented without background

subtraction and were fitted with the function $g^{(2)}(\tau) = 1 - a * exp\left(-\frac{|\tau|}{\tau_{DBT}}\right)$ (red solid line). Clear evidence of single-photon emission was obtained directly from the molecule $g^{(2)}(0) = 0.33 \pm 0.09$, while second order correlation function for light collected from one grating coupler shows $g^{(2)}(0) = 0.50 \pm 0.05$, which is an evident of non-classical nature of outcoupled fluorescence light. The somewhat higher value of $g^{(2)}(0)$ measured at the coupler is related to the lower signal/background ratio due to bigger size of the collection region, *i.e.* large diameter of spatial filter, in the detection path of the setup.

Lifetime measurement

To gain information concerning relaxation dynamics of the wg-coupled molecule – measurement of lifetime of the excited state was performed. It is important to note that lifetime is statistical average, *i.e.* probability to find molecule in the excited state [23]. Molecule was excited by pulsed confocal excitation from Ti:Sa laser with repletion rate 80 MHz (pulses were spaced 12ns apart from each other) with pulse duration 200fs. Reference electrical signal from the Laser was sent to PicoHarp as a start signal, whereas emitted fluorescence single photons outcoupled from one of grating couplers were directed on SPAD connected as well with PicoHarp, thus generated signal on SPAD, when fluorescence photon hits the surface of detector, works as a stop signal. The time difference between start-stop signals, *i.e.* excitation –emission, was detected for many cycles, and histogram was built and fitted by exponential curve, thus average measured lifetime of DBT:Ac coupled to waveguide mode valued as $\tau = 4.2 \pm 0.4\, ns$ [10], which is comparable with lifetime for uncoupled DBT [27].

6.2.5 Experimental β-*factor* determination

Important figure of merit of hybrid molecule-on-waveguide system is probability of coupling of emitted photon into waveguide mode, so called *β-factor*, it can be determined as [76]:

$$\beta = \frac{\Gamma_{wg}}{\Gamma_{wg} + \Gamma_{free} + \Gamma_{nr}}, \qquad (37)$$

where Γ_{wg} and Γ_{free} are radiative decay rate into waveguide mode and in all other optical modes, respectively, Γ_{nr} – non-radiative decay channels.

β-factor is a ratio between flux of power coupled to the waveguide mode to the overall radiated power from the molecule:

$$\beta = \frac{P_{wg}}{P_{wg} + P_{free}} \qquad (38)$$

In the experiment to find the power of fluorescence coupled into waveguide mode P_{wg}, *i.e.* sum of oucoupled flux from both couplers which was read out on the EMCCD camera (Fig. 6.12 c)), fluorescence intensity in the both coupler areas S_{coup} were divided by measured coupling efficiency of grating coupler $\eta_{coup} = 25\% \pm 2\%$, which was determined previously during Transmission measurement of current device. It should be noted that scattered light from grating coupler entirely fits within objective Numerical aperture (NA).

Overall radiated power was found as sum of power coupled into waveguide mode P_{wg} and fluorescence light emitted by molecule into free space $S_{DBT\_free\_space}$, taking into account collection efficiency η_{free_space}. Radiation pattern of the emitter and Numerical aperture of objective impact to the collection efficiency yielding to $\eta_{free\_space} = 5\% \pm 1.5\%$ [10].

Thus, *β-factor* was determined as:

$$\beta_{meas} = \frac{\frac{S_{coup}}{\eta_{coup}}}{\frac{S_{coup}}{\eta_{coup}} + \frac{S_{DBT\_free\_space}}{\eta_{free\_space}}} = 20 \pm 5\% \qquad (39)$$

It was defined *β-factor* for several devices on the chip, where the peak obtained value is $\beta_{meas} = 42\% \pm 2\%$. Spatial distribution of the coupled fluorescence signal into waveguide mode for this device is shown in Fig. 6.14, which was recorded as a movie of fluorescence images as a function of the excitation-spot position on the chip.

Outcoupled detected counts from confocal point and both grating couplers were integrated over areas indicated with white dashed line on Fig. 6.14 c), respectively after subtraction background signal, which was evaluated from the same size rectangular areas nearby the region with the signal, resulting in fluorescence-coupling spatial map shown in Fig. 6.14 b), d), e).

Axes define the position of the confocal pump light beam, while background-subtracted integrated fluorescence signal is color-coded. Spatial map of the integrated fluorescence collected from the region around confocal excitation point (Fig. 6.14a b)) shows Ac crystal containing several molecules, where only one atop of waveguide is coupled to the waveguide mode, which is confirmed by detected strong localized fluorescence signal diffracted from both grating couplers, shown in Fig. 6.14 d), e). Measured spectrum depicted in Fig. 6.14 a) corresponding to the position of excited molecule. Fluorescence signal at waveguide left edge in Fig. 6.14 b) corresponds to molecules lying on top of HSQ layer which are far away from evanescent field of the waveguide to couple in.

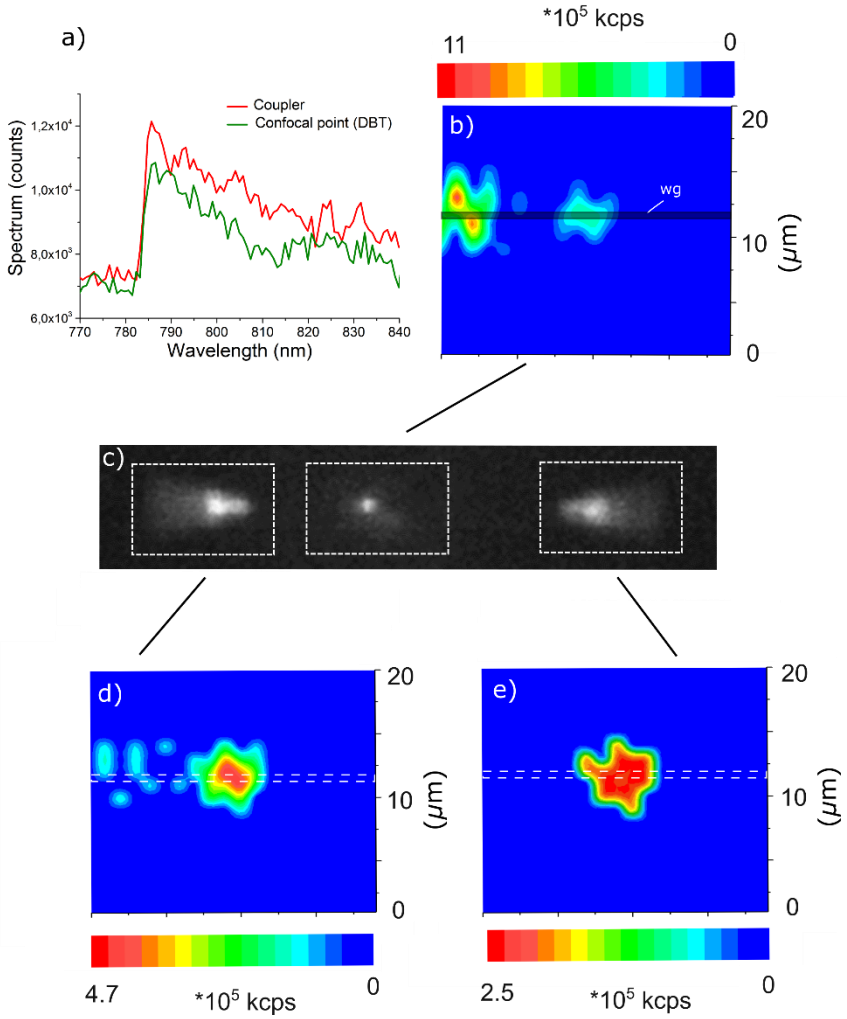

Figure 6.14. **a)** Spectrum of outcoupled fluorescence from grating coupler (red curve) and directly from the molecule (green curve). **b)** Intensity of fluorescence light which scatters from confocal point and outcoupled from both grating couplers **(d,e)** as a function of position of pump light spot during the confocal scan of the area around waveguide (coordinates); black transparent rectangular on b) and white dashed lines on d) and e) show spatial position of the waveguide during the scan. **c)** EMCCD image of outcoupled fluorescence pattern shows $\beta_{meas} = 40\% \pm 3\%$.

6.2.6 β-factor determination via simulations

DBT coupling into bare waveguide

Firstly, DBT:Ac-WG coupling efficiency was estimated through 3D finite element method (FEM) simulations using COMSOL software. It was determined as a ratio between poynting vector flux in the waveguide to the overall radiated flux from the molecule as shown in*; this particular simulation was performed in LENS during our collaboration on this project*. DBT was modelled as a linear harmonic current (length=1nm) embedded in the center of Ac crystal positioned on top of the waveguide. Polarization of dipole was aligned along the major field in the waveguide. With increasing thickness of Ac crystal β-factor decreases from β*=49%* (Ac thickness 10nm) to β*=12% (*Ac. thickness 90nm*)*, this result follows expectation [10]. It should be noted that obtaining Ac thickness 10nm is challenging from fabrication point of view. Interestingly, keeping the dipole embedded in Ac crystal on constant distance from the surface of the waveguide – 10nm, β-factor increases with increasing thickness of Ac crystal obtaining peak value 49% for the thickness of the crystal –180 nm. Lateral displacement of the molecule on 200 nm decreases β-factor from 38% to 14% while keeping Ac crystal thickness 100 nm.

DBT coupling into the waveguide with hole

The next round of simulations were performed by me in the Center for Nanotechnology (Münster). The goal was to determine geometry of the waveguide to boost coupling efficiency. In this case computation was performed using FDTD simulation method using free MEEP [92] software to find the β-factor spectrum. It is especially useful to analyze in case of coupling emitter in PhC cavity as was investigated in Chapter 5, where in one run of computation it can be found coupling efficiency spectrum into all resonance modes. The outlook of this part of work is integrating DBT into PhC cavity localized modes to enhance coupling efficiency. To improve coupling efficiency (without utilization of PhC cavity) the molecule should be positioned in the maximum electric field intensity, thereby ideally in the middle of the waveguide. Therefore, it was chosen the geometry with drilled hole in the middle of the waveguide, where DBT:Ac can be positioned inside the hole covered with protective layer Poly(vinyl alcohol) (PVA) with $n_{eff} = 1.477$, which will prevent photobleaching (Fig. 6.15).

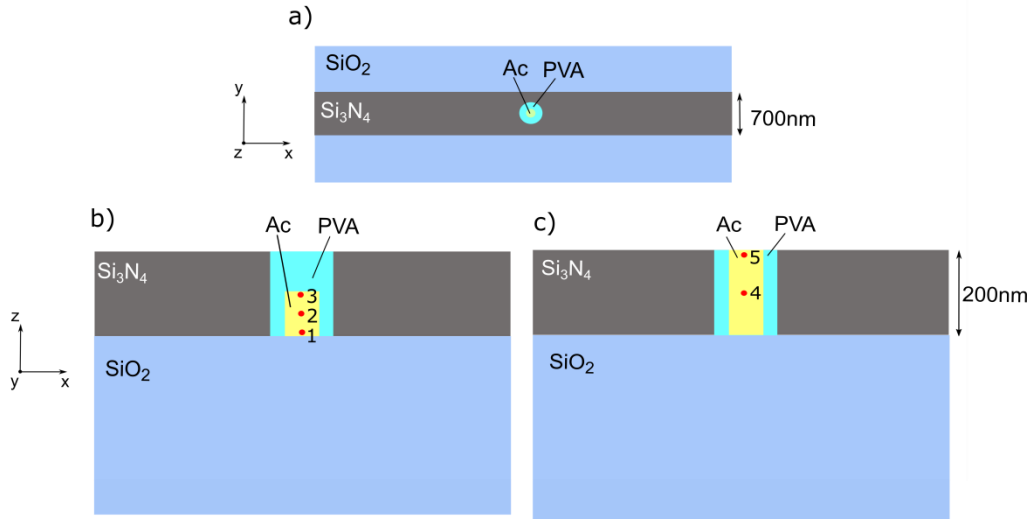

Figure 6.15. Sketch of DBT:Ac positioned inside hole filled with PVA drilled in the Si_3N_4 waveguide on SiO_2 substrate, shown in *xy*-plane on **a)** and *xz*-plane on **b)** and **c)**. Red points correspond to the varied positions of the dipole. Height of Ac crystal 100 nm (a), 200 nm (b); width 200 nm, PVA hole diameter 400 nm.

Thus, coupling efficiency of emitted photon into waveguide mode was determined for different spatial positions of the dipole inside the hole drilled in the waveguide and filled with PVA, whereas dipole was embedded in Ac crystal and positioned at a variable vertical distance from top surface of the waveguide as depicted in Fig. 6.15 b), c). DBT was modeled as a point dipole Gaussian-pulse source (red point on panels b) and c)) with polarization parallel to major field E_y to excite TE-like mode in the waveguide.

β-factor was defined as:

$$\beta = \frac{P_{wg}}{P_{wg} + P_{DBT}}. \qquad (40)$$

Overall radiated power P_{DBT} was determined as Poynting's vector flux over a closed surface around dipole. For this reason it was positioned six detector planes around PVA layer and accumulated Fourier transforms E_y and H_z field for every spot in every detector plane via integration over all simulation run time, thus Poynting flux spectrum was computed utilizing obtained fluxes of these Fourier-transformed fields. Therefore, P_{DBT} is the sum of six normalized Poynting flux spectra over the six detector planes. Fraction of the light coupled into waveguide mode P_{wg} corresponds to the sum of Poynting's vector fluxes registered by two detector planes positioned at the left and right ends of computational cell, which crosses the waveguide. The simulation runs until the mode decayed out from the waveguide.

Computed *β-factor spectrum* is presented on Fig. 6.16.

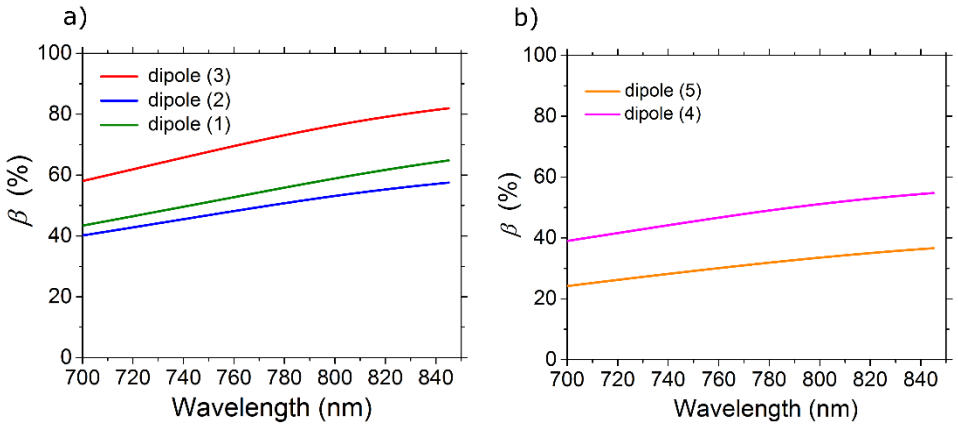

Figure 6.16. **a), b)** Simulated β-factor spectrum for considered positions of the dipole in (b) and (c) in Fig. 6.15, respectively.

For the dipole embedded in the top edge of Ac crystal in position (3) (Fig. 6.15 b)), where height of Ac equals half of the waveguide thickness (100nm), it is achieved maximum value of $\beta = 74\%$ on $\lambda = 785nm$ (red curve on Fig. 6.16 a)). Shift of the dipole closer to the surface of the substrate decreases beta. Interestingly position (1) of the dipole in the vicinity of SiO_2 (Fig. 6.15 b)) corresponds to $\beta = 56\%$ (green curve on Fig. 6.16 a)) and it is higher in comparison with the position (2) in the center of Ac crystal leading to $\beta = 51\%$ (blue curve on Fig. 6.16 a)), which can be explained by interference effects on the edge Si_3N_4-SiO_2.

In case of the Ac crystal height equal to the thickness of the waveguide as depicted in Fig. 6.15 b) coupling efficiency reaches maximum value $\beta = 49\%$ on $\lambda = 785nm$ (pink curve on Fig. 6.16 b)) when the dipole is positioned in the middle of the waveguide – position (4) on Fig. 6.15 c) as expected, while β value at the top edge corresponds to 32%.

In order to make all integrated circuit excitation light should be also coupled to the structure via waveguide on-chip, therefore it was proposed *cross-bar* geometry of the photonic device with perforated hole in the middle, where crossed waveguide is employed as an excitation path and another waveguide – as fluorescence collection path (Fig. 6.17). Besides all integration functionality such structure allows to cut excitation light on 20 dB (crosstalk -20 dB) as was determined in the experimental measurements.

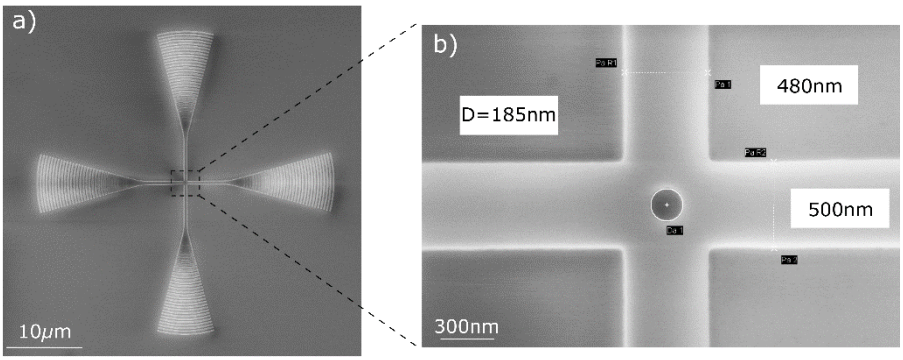

Figure 6.17. SEM image of cross-bar nanophotonic device with drilled air hole in the middle.

Computed β-factor of cross-bar device with the hole in the center decreases on only ≈ 4% in comparison with the case considered in Fig. 6.16, which is allocated to the introduction crossed excitation waveguide.A

Although simulations showed that with increasing the hole size on 100nm β-factor decreases on only ≈ 4%, for the next step integration DBT into PhC cavity smaller fillable holes are required to achieve higher Quality factors, therefore stronger local density of state enhancement, so stronger Purcell enhancement, thus to boost coupling efficiency.

6.3 Concluding remarks

It was simulated, designed and fabricated *hybrid system: molecule-on-Si3N4 photonic device* with grating couplers which enable contact free to read out signal from optical waveguides by imaging through the silica substrate.

Grating couplers efficiency was enhanced in 3 times by placing gold mirrors on top of HSQ buffer layer yielding in maximum averaged measured out-coupling efficiency at 785nm (ZPL of DBT) 35% ± 5% with bandwidth of 50nm.

It was successfully employed such grating ports to read out single photon fluorescence signal emitted by individual DBT molecule coupled evanescently to the waveguide, which was excited upon optical pumping.

Using a Hanbury Brown and Twiss setup it was measured pronounced antibunching dip with $g^{(2)}(0)= 0.50 \pm 0.05$ from the grating couplers and $g^{(2)}(0)= 0.33 \pm 0.09$ directly from the excited single DBT molecule, which confirms the quantum nature of the outcoupled fluorescent light.

7. Conclusion and Outlook

Essential elements base of integrated photonic circuit, such as Cascaded MZI tunable filters [3], Bragg grating filters and Photonic crystal cavities, was engineered and investigated; as well as one of the first realization of *hybrid molecule-on-photonic device on chip* [10] was demonstrated in this Thesis. The work was motivated by creating a scalable and easy integrated photonic devices to make fully integrated hybrid scheme on chip, where besides the placing active source main two components should be employed, namely to enhance spontaneous emission rate and to filter excitation light. It was achieved via design, simulation, fabrication and experimental characterization of corresponding photonic devices on-chip. High-quality photon circuits were built on silicon nitride-on-insulator platform, which ensures low loss light propagation in visible region, as well as sufficient index contrast with SiO_2 to tightly confine the mode.

The engineered *novel* 1D freestanding cross-bar Photonic crystal (PhC) cavity is scalable in terms of resonance wavelength, and will be utilized to enhance spontaneous emission rate via Purcell effect of evanescently coupled NDs in the cavity region.
Novel cross-bar structure, which allows simultaneous collection of enhanced fluorescence through the waveguide (which consists of PhC) and excitation via crossed waveguide, was developed. Such structure spatially separates emitted and pump light. Measured crosstalk amounts -20dB, which means 20 dB filtration out of excitation light.
Part of work under this project was dedicated with programming codes for performing 3D simulations of resonant modes distribution in 1D freestanding cross-bar PhC cavity. According to performed simulations geometry parameters of the cavity were optimized, which was verified during measurements. Thus, optimized cross-bar PhC cavity shows the highest Quality factor $Q = 47 * 10^3$, while simulated one was $Q = 51 * 10^3$ for the same device. Via the next rounds of simulations, it was determined a suitable position of the dipole on the cavity region in order to obtain maximum enhancement of emission coupled into certain resonance mode (LDOS enhancement spatial map was built), thus increased transmission coupling efficiency into cavity (β-factor) was computed and achieved. LDOS enhancement map showed that single photon source should be shifted on around half of the period from the centre of the symmetry plane along longitudinal direction of PhC to achieve maximum enhancement of coupling into odd resonance modes of investigated cross-bar PhC cavities.
Thus, optimized 1D freestanding cross-bar PhC cavity on-chip with fundamental resonance mode, centered at 738 nm corresponding to ZPL of SiV, was engineered and fabricated. For identical PhC cavity with less number of segments, namely with 10 mirror segments from each side of the cavity LDOS enhancement of the emitted light coupled into fundamental mode equals 41 leading to β=*60%* according to the performed simulations. At the same time, higher order odd resonance modes with antinodes of electric field in the cavity region can be as well employed to couple in vibronic bands of NV^- centers in diamond. In particular, for coupling

into third order resonance mode LDOS enhancement factor equaled 3 was simulated, yielding in higher $\beta=73\%$.

It is important to highlight, that experimentally obtained LDOS enhancement of any position of the dipole on the cavity region on fabricated PhC cavity device with higher number of mirror segment can be also evaluated analytically knowing measured Q-factor, simulated mode volume of fabricated PhC cavity and simulated LDOS enhancements maps along each axis for identical PhC cavity with lower number of mirror segments. It should be noted that in such manner obtained analytical results were in agreement with experimental measurements.

Created cascaded thermo-optic MZI filters, based on thermo-optic effect which was provided by placed microheaters on both arms of MZIs, enable to transmit desired wavelength at interference maximum; and at the same time, block excitation light at interference minimum, where in particular transmitted wavelength is wavelength of SiV fluorescence (λ=740 nm) and suppressed wavelength is corresponding excitation light for SiV (λ=532 nm). Architecture of filters, in terms of shape and geometry parameters of microheater and waveguide, was optimized via thermo-optic measurements. It was demonstrated that spiral-type microheaters ensures the lowest switching power - 12.2 mW in comparison with meander shape, which compares favourably with previous reported results for Si_3N_4 platform. Designed tunable filters are multifunctional, allowing transmitting and blocking desired wavelengths in the wide wavelength range, thus making possible to utilize such circuit for future applications at room temperature in hybrid nanophotonic circuits.
The *novel* design, with double microheaters on top of both arms of single and cascaded MZIs, allows to double the range of the shifting amplitude of the interference fringes. Furthermore, it was demonstrated that the cascading two stages of MZI improves filtration depth, which allows to achieve ER=34.7-36.5 dB in terms of difference between simultaneous maximum transmission at 738 nm and minim transmission at 532 nm. Minimal measured insertion loss including propagation loss in the waveguides and loss in both branches amounts 4.2 dB for thermo-optic MZI equipped with spiral shaped microheater.

Another engineered filter – Bragg grating filter on silicon nitride-on-insulator platform on chip was demonstrated. In contrast with Cascaded MZI filters Bragg gratings produce non-repetitive response and were fabricated within single electron-beam lithography step. Single- and double-apodized profile of gratings as well as other dimension parameters of gratings was investigated via transmission measurements. Single Bragg grating filter with double apodization allows to obtain up to 21 dB filtration depth with 3-dB bandwidth 5.5-7 nm, which consists far fewer periods in comparison with single-apodized Bragg filter. Averaged insertion loss in reflected light including optical loss in the splitter is 4.1dB.

One of the first *hybrid system: molecule-on-Si_3N_4 photonic device* was demonstrated in this thesis. Engineered mirror-enhanced grating couplers (with measured peak coupling efficiency

35% ± 5%) were employed to contact free read out single photon signal emitted from individual photostable DBT molecule (embedded in host matrix) and coupled into waveguide mode. Using a Hanbury Brown and Twiss setup it was measured pronounced antibunching dip in the fluorescence light outcoupled directly from molecule $g^{(2)}(0)= 0.33 \pm 0.09$ and from grating coupler $g^{(2)}(0)= 0.50 \pm 0.05$, which confirms the quantum nature of the outcoupled fluorescent light.

Outlook

Engineered photonic elements investigated and optimized in this Thesis will be further employed for the realization of *hybrid* photonic circuits with integrated single photon sources. Investigated *novel* cross-bar PhC cavities will be employed to enhance emission rate of the source. In particular, SiV will be placed on the cavity region, where emitted light into ZPL can be coupled to the fundamental resonance mode, which is matched by the wavelength (738nm) and polarization, at cryogenic temperature. Also vibronic sidebands of NV^- cluster placed on PhC cavity can be coupled to higher order odd resonance modes.

Another promising single photon emitter investigated in this Thesis is DBT molecule, which will be further coupled to engineered optical circuits. Coupling efficiency of single molecule into waveguide mode will be firstly improved by placing it into the single hole drilled in the middle of the waveguide, as was evaluated via simulations in this Thesis. Correct procedure of precise positioning single molecules will be established in such experiment. The next step will be placing molecules into the hole drilled in the cavity region of cross-bar PhC cavities, to further boost transmission coupling efficiency into cavity. New rounds of simulations for optimization geometry parameters of PhC cavity will be performed.

The next promising optically and electrically driven single photon emitter is semiconducting single-walled carbon nanotube (SCNT). SCNT will be utilized to develop *hybrid* CNT-integrated carbon – Si_3N_4 circuits on chip, where CNT will be as well coupled in cross-bar PhC cavity.

To further increase outcoupling efficiency of single photon emission coupled into photonic circuits on chip it will be employed 3D polymer couplers, which manage out-of plane coupling with insertion loss 2-3 dB. This method will increase signal/noise ratio for the efficient second-order correlation function measurement, where detection pronounced antibunching dip is the manifestation of quantum nature of outcoupled light.

Further optimization of investigated optical filters with the aim of cascading several stages and insuring negligible insertion loss will be performed. This will allow to integrate them into the abovementioned hybrid circuits with coupled single photon emitter to filter excitation light to make *all integrated hybrid circuit* on chip.

Supplementary Information

S.1 Fabrication Procedure for 1D freestanding PhC cavity

To experimentally realize freestanding PhC cavity device on chip it was employed silicon nitride-on-insulator wafer consisting of 200 nm stoichiometric Si_3N_4 on top of SiO_2 layer on Si.

Fabrication of the nanophotonic circuits was carried out using several steps of electron-beam lithography:

1. in the first electron-beam step the nanophotonic circuits were defined on top of Si_3N_4 layer using ma-N 2403 negative photoresist, which evenly covers the chip by means of spincoating. After lithography step chip was subsequently developed 1 min in MF-319, where water used as a stopper, following reflow process – heating the chip 2 min on hot plate at 100°. After devices were 3/4 dry-etched into the silicon nitride layer using a CHF_3/O_2 plasma.
2. To suspend the structure in the air underneath SiO_2 should be removed, therefore window around PhC region was opened during the second step of electron-beam lithography. Namely, the chip was covered with positive PMMA photoresist, and required window region was exposed. During development of PMMA in the solution of one part Isopropanol and three parts MIBK (Methyl isobutyl ketone) exposed PMMA in the window region was removed.
3. In the following step remaining ¼ of silicon nitride in the window area was etched, while the waveguide inside of the window was protected with ma-N 2403 resist; the waveguides outside the windows were protected by unexposed PMMA photoresist. After that both photoresists were removed by placing the chip in oxygen plasma.
4. In the last step SiO_2 layer in the windows was removed by wet etching, namely by immersing the chip in Hydrofluoric acid (HF).

Before the second electron-beam step alignment procedure on the global markers written in the first step was performed. Thus, by employing this fabrication technique it is possible to produce hundreds of nanophotonic devices on the chip.

S.2 Optimization of EBL parameters for fabrication freestanding PhC cavity

The main optimization aim was to choose photoresist and corresponding electron beam dose for writing photonic crystal while keeping fabrication parameters of other steps constant. Dose of the exposure is determined by the electron beam current multiplied by the exposure time divided by the beam spot area size. It was employed positive photoresist ZEP-520a and negative photoresist maN-2403.

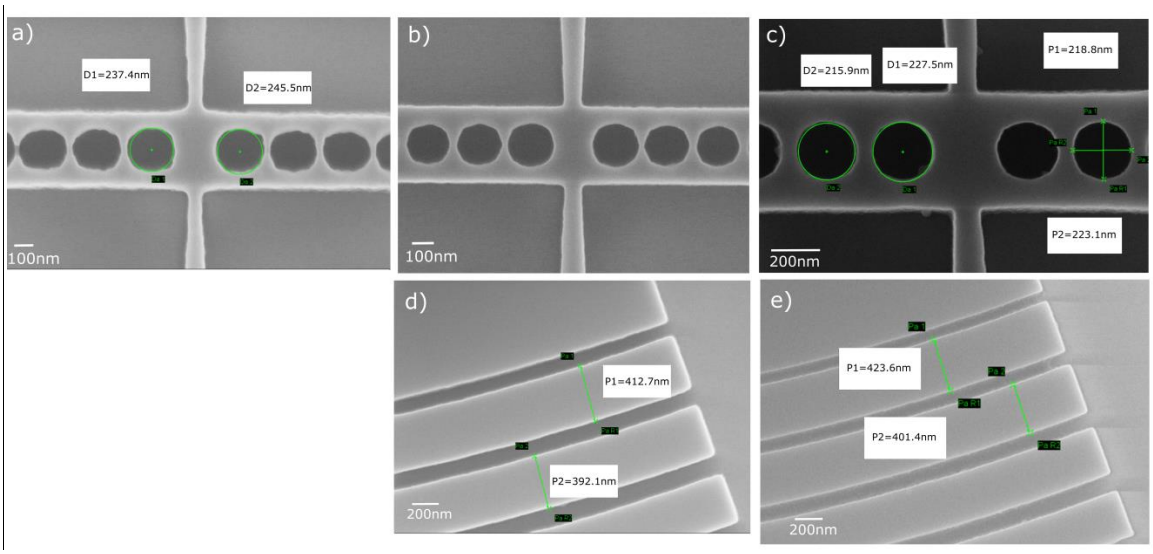

Figure. S.1. SEM images of PhC cavity devices exposed with dose **a)** 130 μC/cm^2, **b,d)** 210 μC/cm^2, **c,e)** 270 μC/cm^2 in maN-2403 after development and reflow process. In the first row it is shown PhC cavity region, in the second row – top part of apodized grating coupler.

PhC devices fabricated using positive photoresist showed elliptical shape of the holes, therefore it was decided to continue optimization of parameters only for negative photoresist maN-2403, namely the dose was changed in the range 130μC/cm^2–310μC/cm^2 with the step 10μC/cm^2. SEM pictures of PhC devices exposed in maN 2403 resist with different doses are shown in Fig. S.1.

It is obvious that higher doses (optimal 270μC/cm^2) are preferable to obtain designed dimensions and round shape of holes in PhC cavity and to prevent roughness. However, for the rest part of nanophotonic device, in particular apodized grating coupler the dose 200 μC/cm^2 is optimal, whereas dose 270 μC/cm^2 corresponds to overexposed case, where resist still remains in between first grooves of grating couplers, resulting in connected Si_3N_4 grooves after etching step.

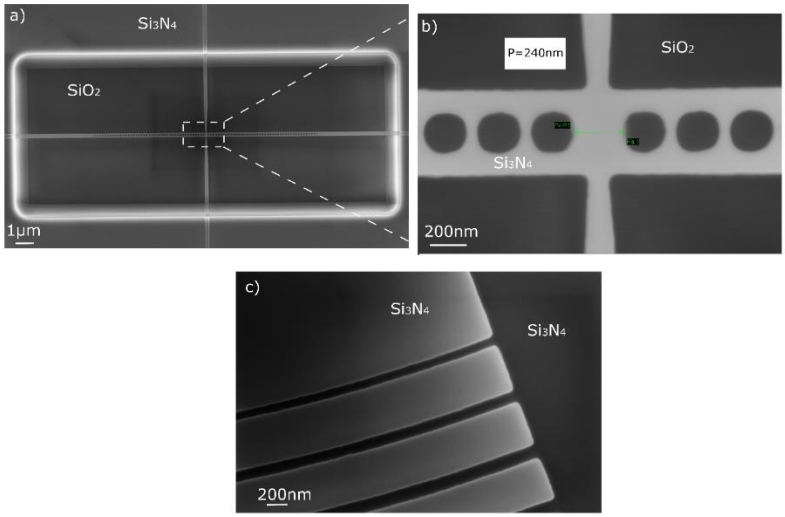

Figure. S.2. a) Freestanding PhC cavity with zoom-in in **b)**. **c)** Apodized grating coupler.

Therefore, it was decided to write nanophotonic devices with optimal dose 200 μC/cm^2 , while thin ring around each hole with higher dose, which is optimal for PhC – 270 μC/cm^2. SEM figure of fabricated freestanding PhC cavity is shown on Fig. S.2.

Acknowledgments

First, I would like to thank my direct supervisor Prof. Dr. Wolfram Pernice for giving me an opportunity to work in his scientific group. I am very grateful to Wolfram for presenting me with a chance to work on interesting and inspiring projects, for expert advice, guidance and absolute encouragement during the work. Thank you for finding always time to discuss my scientific questions and being attentive to ideas, which naturally questions me up during my work on the particular scientific task, and for providing me with freedom to try and accomplish them!

I would like to thank to my official supervisor Prof. Dr. rer. nat. Uli Lemmer (Karlsruhe Institute of Technology (KIT)) for helping in organizational processes in Karlsruhe Institute of Technology from the very beginning of my PhD work.

I would like to thank my co-supervisor Prof. Francesco Cataliotti for the possibility to gain new scientific experience while working in European Laboratory for Non-linear Spectroscopy (University of Florence, Italy) according to Erasmus Mundus Europhotonics PhD Program.

I would like to express my gratitude to Erasmus Mundus Europhotonics PhD Program for giving me an opportunity to work in Karlsruhe Institute of Technology in collaboration with European Laboratory for Non-linear Spectroscopy (LENS, University of Florence, Italy) under scientific projects to defend PhD. I am very thankful to organizer of the Program, Ms. Sophie Brasselet for supporting me in organizational processes during my tenure in Europhotonics PhD Program; and for being very quick in replying to my questions. Also, thank you to Dr. Jurana Hetterich as an official, responsible for Erasmus Program in KIT; and Mr. Hartmut Speck from International Office in KIT for help with organizational questions.

I would like to thank my fellow colleague and close friend Dr. Svetlana Khasminskaya for introduction in measurement setup in our Laboratory, valuable scientific advice and helping me with arranging my living accommodations from my very first day in Karlsruhe.

I would like to thank my colleague Nico Gruhler for introduction in Fabrication technique, for valuable scientific discussions, for participation in the project in collaboration with LENS under the realization of hybrid nanophotonic device with integrated single molecule, and for participation in fabrication of freestanding photonic crystal cavities on chip.

I am thankful to my colleague Simone Ferrari for introduction and support in laboratory equipment and writing scripts to control and manage equipment which was in particular used to automate thermo-optic measurements of tunable cascaded MZI filters on chip. Simone made great work to organize Clean Room in Münster Nanofabrication Facility.

I would like to mention my former colleague Valentin Fütterling for introduction in computation of photonic crystal cavities at the beginning of my work on this topic. I also want to express my gratitude to all my formers colleagues: Dr. Patrik Rath, Dr. Oliver Kahl and Dr. Matthias Stegmaier for valuable scientific discussions and friendly atmosphere.

I would like to thank Dr. Silvia Diewald (KIT) for performing electron beam lithography for projects during my work in KIT.

It was a pleasure to work with my collaborators and colleagues from LENS where I worked more than half-a-year under the project of *Coupling single DBT molecule into hybrid nanophotonic circuit* according to Erasmus Mundus Europhotonics PhD Program. The work together with Dr. Costanza Toninelli and with my direct colleague Dr. Pietro Lombardi was very interesting and effective work in a friendly environment, eventually resulting in join successful realization experiments, outcomes of which were published. I would like to emphasize that we continue our collaboration under new project which consolidates several another scientific groups.

I would like to highlight my collaborator Prof. Dr. Alexander Kubanek (University of Ulm) for joint active work under the project *Coupling NDs in PhC cavity*.

A special thank you to my current collaborator Dr. Felix Pyatkov for intensive joint work under the realization of *Hybrid CNT integrated circuit on chip* project. Moreover, Felix with his wife Elena; and Svetlana with her husband Christian are my close friends, who support and help me with my living accommodations and give always help-hand from my very first day in Karlsruhe till now.

I am happy to work in the scientific group where all my current colleagues continue to support friendly and positive atmosphere, where mutual help prevails, and which is the environment Wolfram created and supported all these years!

I would like to highlight my colleagues Wladislaw Hartmann, Johannes Feldmann, Nicolai Walter and Fabian Beutel, who currently manage Clean Room facilities in Münster Nanofabrication Facility. Fabian and me performed the first *dose test* experiments on our new Electron-beam lithography machine, and optimized parameters of writing chips. Johannes and I manage Chemistry Lab. With Wladislaw, Johannes and Nicolai we had many scientific and just life related discussions.

I am grateful to Wladick and Fabian for help-hand always when it was needed in any aspect!

I would like to thank Johannes Feldmann and Nico Gruhler for help with translation Abstract into German of this Thesis.

I would like to thank my colleague Dr. Francesco Lenzini for suggestions on grammatical corrections in the Abstract.

It was possible to automate routine measurements and to run our simulations, owing to scripts for automation measurements and setting up servers, respectively, which were performed by Helge Gehring and Maik Stappers.
Also, I would like to note our collaborator Dr. Vadim Kovalyuk (Moscow State Pedagogical University), with whom we had valuable scientific discussions during his stay in our group.

I would like to thank out team assistants Nicole Altmann and Johanna Köster for help with formalization of documents.

I would like to also note that out friendly scientific atmosphere in the group is shared with the group of Jun.-Prof. Carsten Schuck, resulting in joint seminars, discussions as well as our cultural and fun events.

I would like to thank my best school friends and friends from my *alma mater* – Bauman Moscow State Technical University for always being interested in my achievements.

I would like to express my tremendous gratitude to my Family!

I would like to thank my all relatives: brother, aunts, uncles, cousins for endless support. A special thank you to my cousin Hayk, for advices and for being my helping hand any time I need it, and in any questions in any topics.

I will never be able to thank enough my father, Peter for gold advices and for creating scientific atmosphere around me. I heard the words “laser”, “optical fiber”, “optics”, etc. from my early childhood, those were the foundation of my dad’s scientific work. Thus, I naturally chose *engineering-scientific way*. He also cultivated my love to sport, which he also always has direct relation up to now.

It is impossible to express in words what my mom, Anush does for me. I will never be able to thank enough for tremendous support, first help and gold advices in every aspect of my life, and also for the very first introduction to programming.

Bibliography

[1] E. Purcell, H. Torrey, and R. Pound. Resonance absorption by nuclear magnetic moments in a solid. *Phys. Rev*., 69(1-2):37–38. (1946). doi: 10.1103/physrev.69.37.

[2] BT Labs delivers ultra-efficient terabit 'superchannel'. *BT. 2017-06-19. Retrieved 2018-08-03.*

[3] A.P. Ovvyan, N. Gruhler, S. Ferrari and W.H.P. Pernice. Cascaded Mach–Zehnder interferometer tunable filters. *Journal of Optics*, vol. 18, N. 6. (2016).

[4] F. Horst, W.M.J. Green, S. Assefa, S. M. Shank, Y.A. Vlasov, B.J. Offrein. Cascaded Mach-Zehnder wavelength filters in silicon photonics for low loss and flat pass-band WDM demultiplexing. *Opt. Express*, vol. 21, 11652-11658, (2013).

[5] W. Shi, M. Greenberg, X. Wang, Y. Wang, C. Lin, N.A. F. Jaeger, L. Chrostowski. Single-band add-drop filters using anti-reflection, contra-directional couplers. *IEEE Xplore*: (2012). doi: 10.1109/GROUP4.2012.6324073.

[6] G.T. Reed, G. Mashanovich , F. Y. Gardes, D. J. Thomson. Silicon optical modulators. *Nature Photonics* , vol. 4, 518–526 (2010).

[7] W.H.P. Pernice, C. Schuck, O. Minaeva, M. Li, G.N. Goltsman, A.V. Sergienko, H.X. Tang. High-speed and high-efficiency travelling wave single-photon detectors embedded in nanophotonic circuits. *Nat. Commun.*, vol. 3, 1325, (2012). https://doi.org/10.1038/ncomms2307.

[8] S. Ferrari , C. Schuck , W.H.P. Pernice. Waveguide-integrated superconducting nanowire single-photon detectors. *Nanophotonics*, vol. 7, 11 (2018). doi: 10.1515/nanoph-2018-0059.

[9] S. Khasminskaya, F. Pyatkov, K. Słowik, S. Ferrari, O. Kahl, V. Kovalyuk, P. Rath, A. Vetter, F. Hennrich, M. Kappes, G. Goltsman, A. Korneev, C. Rockstuhl, R. Krupke, W.H.P. Pernice. Fully integrated quantum photonic circuit with an electrically driven light source. *Nat. Photon.*, vol. 10, 727–732 (2016). doi:10.1038/nphoton.2016.178.

[10] P. Lombardi, A. P. Ovvyan, S. Pazzagli, G. Mazzamuto, G. Kewes, O. Neitzke, N. Gruhler, O. Benson, W. H. P. Pernice, F. S. Cataliotti, and C. Toninelli. Photostable Molecules on Chip: Integrated Sources of Nonclassical Light. *ACS Photonics*, vol. 5, 126−132 (2018). doi: 10.1021/acsphotonics.7b00521.

[11] F. Pyatkov, V. Fütterling, S. Khasminskaya, B. Flavel, F. Hennrich, M. Kappes, R. Krupke, W. H. P. Pernice. Cavity enhanced light emission from electrically driven carbon nanotubes. *Nat. Photon.* vol. 10, 420-427 (2016). doi:10.1038/nphoton.2016.70.

[12] S. Khasminskaya, F. Pyatkov, B. Flavel, W. Pernice, R. Krupke. Waveguide-integrated light-emitting carbon nanotubes. *Advanced Materials* vol. 26, 3465 (2014). doi:10.1002/adma.201305634.

[13] L. Luozhou, T. Schröder, E. H. Chen, M. Walsh, I. Bayn, J. Goldstein, O. Gaathon, M. E. Trusheim, M. Lu, J. Mower, M. Cotlet, M. L. Markham, D. J. Twitchen , D. Englund. Coherent spin control of a nanocavity-enhanced qubit in diamond. *Nat. Commun.* vol. 6, 6173 (2015). doi:10.1038/ncomms7173.

[14] P. Tonndorf, O. Del Pozo-Zamudio, N. Gruhler, J. Kern, R. Schmidt, A. I. Dmitriev, A. P.Bakhtinov, A. I. Tartakovskii, W.H. P. Pernice, S. Michaelis de Vasconcellos, R. Bratschitsch. On-Chip Waveguide Coupling of a Layered Semiconductor Single-Photon Source. *Nano Lett.* vol.17 (9), 5446-
5451 (2017). doi:http://dx.doi.org/10.1021/acs.nanolett.7b02092.

[15] R. Brouri, A. Beveratos, J.-P. Poizat, P. Grangier. Photon antibunching in the fluorescence of individual color centers in diamond. *Opt. Lett.* vol. 25 (17), 1294–1296 (2000). doi http: //dx.doi.org/10.1364/OL.25.001294.

[16] J. Wrachtrup and F. Jelezko. Processing quantum information in diamond. *J.Phys. Condens. Matter* vol.18, S807 (2006).

[17] M.W. Dohertya, N. Manson, P. Delaney, F. Jelezko, J. Wrachtrupe, L. C.L. Hollenberga. The nitrogen-vacancy colour centre in diamond. *Physics Reports,* vol. 528, 1, 1-45. (2013). doi: https://doi.org/10.1016/j.physrep.2013.02.001.

[18] T. Schröder1, F. Gädeke, M. J. Banholzer, O. Benson. Ultrabright and efficient single-photon generation based on nitrogen-vacancy centres in nanodiamonds on a solid immersion lens. *New Journal of Physics*, vol. 13, (2011).

[19] C. Santori, P.E. Barclay, K-M C. Fu, R.G. Beausoleil, S. Spillane, M. Fisch. Nanophotonics for quantum optics using nitrogen-vacancy centers in diamond *Nanotechnology*, vol. 21, (2010). doi: 10.1088/0957-4484/21/27/274008.

[20] T. Feng, B.D. Schwartz. Characteristics and origin of the 1.681 eV luminescence centre in chemical-vapor-deposited diamond films. *Journal of Applied Physics. 73* (3): 1415, (1993). doi*:*10.1063/1.353239.

[21] L.J. Rogers, K.D. Jahnke, T. Teraji, L. Marseglia, C. Müller, B. Naydenov, H. Schauffert, C. Kranz, J. Isoya, L.P. McGuinness, F. Jelezko. Multiple intrinsically identical single-photon emitters in the solid state. *Nature Communications,* vol. 5, 4739 (2014). doi: https://doi.org/10.1038/ncomms5739.

[22] A. Sipahigil, K. D. Jahnke, L. J. Rogers, T. Teraji, J. Isoya, A. S. Zibrov, F. Jelezko, and M. D. Lukin. Indistinguishable Photons from Separated Silicon-Vacancy Centers in Diamond. Phys. *Phys. Rev. Lett*. 113, 113602 (2014).

[23] B. Lounis, W.E. Moerner. Single photons on demand from a single molecule at room temperature. *Nature.* 407, 6803 (2000). doi:10.1038/35035032.

[24] C. Brunel, B. Lounis, P. Tamarat, and M. Orrit. Triggered Source of Single Photons based on Controlled Single Molecule Fluorescence. *Phys. Rev. Lett*. 83, 2722 (1999).

[25] A.A. Nicolet, C. Hofmann, M.A. Kol'chenko, B. Kozankiewicz, M. Orrit. Single dibenzoterrylene molecules in an anthracene crystal: spectroscopy and photophysics. *Chemphyschem*., 8(8):1215-20 (2007).

[26] A.A. Nicolet, B.P. Hofmann, M.A. Kol'chenko, B. Kozankiewicz, R. Brown, M. Orrit Single dibenzoterrylene molecules in an anthracene crystal: main insertion sites. *Chemphyschem*., 8(13):1929-36 (2007).

[27] C. Toninelli, K. Early, J. Bremi, A. Renn, S. Götzinger, and V. Sandoghdar. Near-infrared single-photons from aligned molecules in ultrathin crystalline films at room temperature. Opt. Express vol. 18, 6577-6582 (2010).

[28] Iijima S. Helical microtubules of graphitic carbon. Nature. 354(6348):56–8 (1991).

[29] R. Miura, S. Imamura, R. Ohta, A. Ishii, X. Liu, T. Shimada, S. Iwamoto, Y. Arakawa & Y. K. Kato. Ultralow mode-volume photonic crystal nanobeam cavities for high-efficiency coupling to individual carbon nanotube emitters. *Nature Communications,* vol. 5, 5580 (2014).

[30] J.C. Charlier, X. Blase, S. Roche. Electronic and transport properties of nanotubes. *Rev Mod Phys.* 79(2):677–732, (2007).

[31] J. Lefebvre, J. Fraser, P. Finnie, and Y. Homma. Photoluminescence from an individual single-walled carbon nanotube. *Phys. Rev.* B 69, 1 (2004).

[32] J. Lefebvre, D. G. Austing, J. Bond, and P. Finnie. Photoluminescence imaging of suspended single-walled carbon nanotubes. *Nano Lett*. vol. 6, 1603 (2006).

[33] M. Freitag, M. Steiner, A. Naumov, J. P. Small, A. A. Bol, V. Perebeinos, and P. Avouris. Carbon Nanotube Photo- and Electroluminescence in Longitudinal Electric Fields. *ACS Nano* vol. 3, 3744 (2009).

[34] P. Avouris, M. Freitag, and V. Perebeinos. Carbon-nanotube photonics and optoelectronics. *Nat. Photonics* vol. 2, 341 (2008).

[35] J.A. Misewich, R. Martel, P. Avouris, J.C. Tsang, S. Heinze, J. Tersoff. Electrically induced optical emission from a carbon nanotube FET. Science. 2;300(5620):783-6 (2003). DOI:10.1126/science.1081294.

[36] A. Jorio; G. Dresselhaus; M.S. Dresselhaus. Carbon Nanotubes, vol. 111 of Topics in Applied Physics, (Springer Berlin Heidelberg, Berlin, Heidelberg) (2008).

[37] P. Kapusta, M. Wahl, and R. Erdmann. Advanced Photon Counting, vol. 15 of Springer Series on Fluorescence, (Springer International Publishing, Cham) (2015).

[38] D.Mann, Y.K. Kato, A. Kinkhabwala, E. Pop, J. Cao, X. Wang, L. Zhang, Q. Wang, J. Guo & H. Dai. Electrically driven thermal light emission from individual single-walled carbon nanotubes. *Nature Nanotechnology,* vol. 2, pages 33–38 (2007).

[39] F. Jakubka, S.B. Grimm, Y. Zakharko, F. Gannott, J. Zaumseil. Trion electroluminescence from semiconducting carbon nanotubes. *ACS Nano*. 8(8), 8477–86 (2014).

[40] M.S. Hofmann, J.T. Glückert, J. Noé, C. Bourjau, R. Dehmel, A. Högele. Bright, long-lived and coherent excitons in carbon nanotube quantum dots. *Nat Nanotechnol*. ,8(7), 502–5 (2013).

[41] X. Ma, N.F. Hartmann, J.K.S. Baldwin, S.K. Doorn, H. Htoon. Room-temperature single-photon generation from solitary dopants of carbon nanotubes. *Nat Nanotechnol*. 10(8), 671–5, (2015).

[42] A. Vijayaraghavan, M. Oron-Carl, S. Blatt, A. Vijayaraghavan, S. Blatt, D.Weissenberger, D. Weissenberger, M. Oron-Carl, F. Hennrich, F. Hennrich, D. Gerthsen, H. Hahn, D. Gerthsen, H. Hahn, R. Krupke, and R. Krupke. Ultra-largescale directed assembly of single-walled carbon nanotube devices. Supporting Information. *Nano Lett.* vol. 7, 1556 (2007).

[43] J.-M. Liu, Photonic Devices, Cambridge University Press, Cambridge, 1052 (2005).

[44] COMSOL Multiphysics®. www.comsol.com. COMSOL AB, Stockholm, Sweden.

[45] W.H. Bragg, W.L. Bragg. The Reflection of X-rays by Crystals. Proceedings of the Royal Society of London. Series A, Containing Papers of a Mathematical and Physical Character, vol. 88, 605, 428-438 (1913).

[46] A. Bozzola, L. Carroll, D. Gerace, I. Cristiani, and L. C. Andreani. Optimising apodized grating couplers in a pure SOI platform to −0.5 dB coupling efficiency. *Opt. Express* 23, 16289-16304 (2015).

[47] S. Romero-García, F. Merget, F. Zhong, H. Finkelstein, and J. Witzens. Silicon nitride CMOS-compatible platform for integrated photonics applications at visible wavelengths. *Opt. Express* 21, 14036-14046 (2013).

[48] X. Chen, C. Li, C. K. Y. Fung, S. M. G. Lo and H. K. Tsang. Apodized Waveguide Grating Couplers for Efficient Coupling to Optical Fibers. *IEEE Photonics Technology Letters*, vol. 22, no. 15, pp. 1156-1158 (2010). doi: 10.1109/LPT.2010.2051220.

[49] D. J. Thomson, F. Y. Gardes, J-M Fedeli, S. Zlatanovic, Y. Hu, B.P.P. Kuo, E. Myslivets, S. Radic, G. Z. Mashanovich, and G. T. Reed. 50-Gb/s Silicon Optical Modulator. *IEEE Photonics Technology Letters*, vol. 24, 4 (2014).

[50] D. J. Thomson , F. Y. Gardes, S. Liu , H. Porte, L. Zimmermann, J-M Fedeli , Y. Hu , M. Nedeljkovic , X. Yang , P. Petropoulos , G. Z. Mashanovich. High Performance Mach–Zehnder-Based Silicon Optical Modulators. *IEEE Journal of Selected Topics in Quantum Electronics*, vol 19, 85-94 (2013).

[51] X.Tu, J. Song, T-Y Liow, M. K. Park, J. Q.Yiying, J. S. Kee, M. Yu, and G-Q Lo. Thermal independent Silicon-Nitride slot waveguide biosensor with high sensitivity. *Opt. Express* 20, 2640-2648 (2012).

[52] Lord Rayleigh Sec. R. S.. XVII. On the maintenance of vibrations by forces of double frequency, and on the propagation of waves through a medium endowed with a periodic structure. *Philosophical Magazine and Journal of Science*, 145-159 (1887).

[53] J. D Joannopoulos, S. G. Johnson, J. N. Winn, and R. D. Meade. Photonic Crystals: Molding the Flow of Light, 2nd ed., Princeton University Press (2008).

[54] Y. Akahane, T. Asano, B.-S. Song, and S. Noda. High-Q photonic nanocavity in a two-dimensional photonic crystal. *Nature* 425, 944–947 (2003).

[55] Q. Quan and M. Loncar. Deterministic design of wavelength scale, ultra-high Q photonic crystal nanobeam cavities. *Opt. Express* vol. 19, 18529-18542 (2011), https://doi.org/10.1364/OE.19.018529.

[56] M. Grande, G. Calo, V. Petruzzelli, and A. D'Orazio. High-Q Photonic Crystal Nanobeam Cavity based on a Silicone Nitride Membrane Incorporating fabrication imperfections and a low-index layer. *Progress in Electromagnetics Research B,* vol. 37, 191-204 (2012).

[57] J. Zhou, H. Tian, D. Yang, Q. Liu, L. Huang, and Y.g Ji. Refractive index sensing utilizing parallel tapered nano-slotted photonic crystal nano-beam cavities. *J. Opt. Soc. Am. B,* vol. 31, 8 (2014).

[58] Zhang, Murray W. McCutcheon, Ian B. Burgess, and Marko Loncar. Ultra-high-Q TE/TM dual-polarized photonic crystal nanocavities. *Opt. Lett*. 34, 2694-2696 (2009).

[59] D. Yang, H. Tian, and Y. Ji. High-*Q* and high-sensitivity width-modulated photonic crystal single nanobeam air-mode cavity for refractive index sensing. *Applied Optics*, vol. 54, 1, 1-5(2015). https://doi.org/10.1364/AO.54.000001.

[60] Murray W. McCutcheon and Marko Lončar. Design of a silicon nitride photonic crystal nanocavity with a Quality factor of one million for coupling to a diamond nanocrystal. *Opt. Express* vol. 16, 19136-19145 (2008).

[61] I. Mukherjee, G.Hajisalem, and R. Gordon. One-step integration of metal nanoparticle in photonic crystal nanobeam cavity. *Opt. Express* vol. 19, 22462-22469 (2011).

[62] Y. Gong, B. Ellis, G. Shambat, T. Sarmiento, J. S. Harris, and J. Vučković. Nanobeam photonic crystal cavity quantum dot laser. *Opt. Express* vol. 18, 8781-8789 (2010).

[63] R. G. Hulet, E. S. Hilfer, and D. Kleppner. Inhibited Spontaneous Emission by a Rydberg Atom. *Phys. Rev. Lett*. vol. 55, 2137 (1985).

[64] P. A. M. Dirac. The quantum theory of the emission and absorption of radiation. Proceedings of the Royal Society A: Mathematical, Physical and Engineering Sciences, 114(767):243–265. (1927). http://dx.doi.org/10.1098/rspa.1927.0039.

[65] E. N. Economou. Green's Functions in Quantum Physics, 3rd ed., Berlin, Germany: Springer, (2010).

[66] A.Lagendijk , and B.A. van Tiggelen. Resonant multiple scattering of light. *Physics Reports*, vol. 270, 143–215 (1996).

[67] A. Taflove, A. Oskooi, S. G. Johnson. Advances in FDTD Computational Electrodynamics: Photonics and Nanotechnology. *Artech House Publishers* (2013).

[68] A. J. Ward, and J. B. Pendry. Calculating photonic Green's functions using a nonorthogonal finitedifference time-domain method. *Physical Review B*, vol. 58, 7252–7259 (1998).

[69] R. Coccioli, M. Boroditsky, K.W. Kim, Y. Rahmat-Samii, and E. Yoblonovitch. Smallest possible electromagnetic mode volume in a dielectric cavity. *IEEE Proceedings Optoelectronic*s 145, 391 (1998).

[70] J.D. Witmer, J.T. Hill, and A. H. Safavi-Naeini. Design of nanobeam photonic crystal resonators for a silicon-on-lithium-niobate platform. *Opt. Express* vol. 24, 5876-5885 (2016).

[71] E. Kuramochi, H. Taniyama, T. Tanabe, K. Kawasaki, Y-G Roh, and M. Notomi. Ultrahigh-Q one-dimensional photonic crystal nanocavities with modulated mode-gap barriers on SiO_2 claddings and on air claddings. *Opt. Express* vol. 18, 15859-15869 (2010).

[72] M. Khan, T. Babinec, M. W. McCutcheon, P. Deotare, and M.o Lončar. Fabrication and characterization of high-quality-factor silicon nitride nanobeam cavities. *Opt. Lett*. vol. 36, 421-423 (2011)

[73] Jia-Ming Liu. Principles of Photonics, Cambridge University Press (2016).

[74] R. Hanbury Brown and R. Twiss. Correlation between photons in two coherent beams of light. *Nature* 177, 27 (1956).

[75] R. Hanbury Brown; R. Q. Twiss. A Test of a New Type of Stellar Interferometer on Sirius. *Nature*. 178 (4541): 1046–1048. (1956). doi:10.1038/1781046a0.

[76] B. Lounis and M. Orrit. Single-photon sources. *Rep. Prog. Phys*. 68 1129–1179 (2005). doi:10.1088/0034-4885/68/5/R04.

[77] G Mazzamuto, A. Tabani, S. Pazzagli, S. Rizvi, A. Reserbat-Plantey, K. Schädler, G. Navickaite, L. Gaudreau, F. S. Cataliotti, F. Koppens and C. Toninelli. Single-molecule study for a graphene-based nano-position sensor. *New Journal of Physics*, vol. 16 (2014).

[78] R. Verberk, A. M. van Oijen, and M. Orrit. Simple model for the power-law blinking of single semiconductor nanocrystals. *Phys. Rev.* B 66, 233202 (2002).

[79] J.C. Lee, I. Aharonovich, A.P. Magyar, F. Rol , and E.L. Hu. Coupling of silicon-vacancy centers to a single crystal diamond cavity. *Opt. Express* vol. 20 8891–7 (2012).

[80] A. Densmore, S. Janz, R. Ma, J.H. Schmid, Xu D-X, A. Delage, J. Lapointe, M. Vachon, and P. Cheben . Compact and low power thermo-optic switch using folded silicon waveguides. *Opt. Express* vol. 17 10457–65 (2009).

[81] M. Nedeljkovic, S. Stankovic, C.J. Mitchell, A.Z. Khokhar, S.A. Reynolds, D.J. Thomson, F.Y. Gardes, C.G. Littlejohns, G.T. Reed and G.Z. Mashanovich. Mid-infrared thermooptic modulators in SOI. *IEEE* vol. 26 1352–5 (2014).

[82] T. Chu, H. Yamada, S. Ishida and Y. Arakawa. Compact 1 × N thermo-optic switches based on silicon photonic wire waveguides. Opt. Express vol. 13 10109–14, (2005).

[83] R.L. Espinola, M.C. Tsai, J.T. Yardley and R.M. Osgood. Fast and low-power thermooptic switch on thin silicon-oninsulator. IEEE vol. 15 1366–8, (2003).

[84] N.C. Harris, Y. Ma, J. Mower, T. Baehr-Jones, D. Englund, M. Hochberg and C. Galland. Efficient, compact and low loss thermo-optic phase shifter in silicon. Opt. Express vol. 22 10487–93, (2014).

[85] X. Wang, J. Liu, Q. Yan, S. Chen and J. Yu . SOI Thermooptic modulator with fast response. *Opt. Lett*. vol. 1 527–8 (2003).

[86] Q. Fang, J.F. Song, T.Y. Liow, H. Cai, M.B. Yu, G.Q. Lo and D-L Kwong. Ultralow power silicon photonics thermo-optic switch with suspended phase arms. *IEEE* vol. 23 525–7, (2011).

[87] D. J. Moss, R. Morandotti, A. L. Gaeta, and M. Lipson. New CMOS-compatible platforms based on silicon nitride and Hydex for nonlinear optics. *Nature Photonics* 7 (8), 597–607 (2013) doi http://dx.doi.org/10.1038/nphoton.2013.183.

[88] X. Tu, J. Song, T-Y Liow, M.K. Park, J.Q. Yiying, J.S. Kee, M. Yu and G-Q Lo. Thermal independent Silicon-Nitride slot waveguide biosensor with high sensitivity. Opt.Express 20 2640–8, (2012).

[89] Ed.: M. Stepanova, S. Dew, Nanofabrication - Techniques and Principles, (Ed.: M. Stepanova, S. Dew), Springer-Verlag, Wien, 2012, 344.

[90] H-C Liou, J. Pretzer. Effect of curing temperature on the mechanical properties of hydrogen silsesquioxane thin films.*Thin Solid Films* 335 186-191 (1998).

[91] Choi, M. J. Word, V. Kumar, and I. Adesida, J. Vac. Comparative study of thermally cured and electron-beam-exposed hydrogen silsesquioxane resists. *SSci. Technol*. B 26, 1654 (2008). doi: 10.1116/1.2960565.

[92] A.F. Oskooi, D. Roundy, M. Ibanescu, P. Bermel, J.D. Joannopoulos, and S.G. Johnson. MEEP: A flexible free-software package for electromagnetic simulations by the FDTD method. *Computer Physics Communications*. vol. 181, 687-702. (2010).

[93] S. G. Johnson and J. D. Joannopoulos. Block-iterative frequency-domain methods for Maxwell's equations in a planewave basis. *Optics Express* vol. 8, no. 3, 173-190 (2001).

[94] Y. Akahane, T. Asano, B.-S. Song, and S. Noda. High-@Q photonic nanocavity in a two-dimensional photonic crystal. *Nature* 425 , 944–947 (2003).

[95] M. Ibanescu, E. J. Reed, and J. D. Joannopoulos. Enhanced Photonic Band-Gap Confinement via Van Hove Saddle Point Singularities. PRL 96, 033904 (2006).

[96] A. W. Schell, G. Kewes, T. Schröder, J. Wolters, T. Aichele, and O. Benson. A scanning probe-based pick-and-place procedure for assembly of integrated quantum optical hybrid devices. Review of Scientific Instruments 82(7), 073709 (2011).

[97] A. Yariv, P. Yeh. Photonics: Optical Electronics in Modern Communications. *Oxford University Pres*s. 6 edition (2006).

[98] D. T. H. Tan, K. Ikeda, R. E. Saperstein, B. Slutsky, and Y. Fainman. Chip-scale dispersion engineering using chirped vertical gratings. *Opt. Lett*. 33, 3013-3015 (2008).

[99] D. T. H. Tan, K. Ikeda, and Y. Fainman. Cladding-modulated Bragg gratings in silicon waveguides. *Opt. Lett*. 34, 1357-1359 (2009).

[100] X. Wang, W. Shi, H. Yun, S. Grist, N. A. F. Jaeger, and L. Chrostowski. Narrow-band waveguide Bragg gratings on SOI wafers with CMOS-compatible fabrication process. *Opt. Express* 20, 15547-15558 (2012).

[101] H. Yun, Z. Chen, Y. Wang, J. Fluekiger, M. Caverley, L. Chrostowski, and N. A. F. Jaeger. Polarization-rotating, Bragg-grating filters on silicon-on-insulator strip waveguides using asymmetric periodic corner corrugations. *Opt. Lett*. 40, 5578-5581 (2015).

[102] S. Schmidt, J. Flueckiger; W.X. Wu, S. M. Grist, S, T. Fard; V. Donzella, P. Khumwan, E. R. Thompson, Q. Wang, P. Kulik, X. Wang; A. Sherwali, J. Kirk, K. C. Cheung, L. Chrostowski, Daniel Ratner. Improving the performance of silicon photonic rings, disks, and Bragg gratings for use in label-free biosensing. *SPIE 9166, Biosensing and Nanomedicine VII*, 91660M (2014); doi: 10.1117/12.2062389.

[103] L. Chrostowski, M. Hochberg. Silicon Photonics Design: From Devices to Systems 1st Edition, Cambridge University Press; 1 edition (2015).

[104] W. Shi, X. Wang, C. Lin, H. Yun, Y. Liu, T. Baehr-Jones, M. Hochberg, N. A. F. Jaeger, and L. Chrostowski. Silicon photonic grating-assisted, contra-directional couplers. *Opt. Express* 21, 3633-3650 (2013).

[105] W. Shi *et al.*, "Single-band add-drop filters using anti-reflection, contra-directional couplers," *The 9th International Conference on Group IV Photonics (GFP)*, San Diego, CA,. 21-23 (2012). doi: 10.1109/GROUP4.2012.6324073.

[106] X. Zhao, Y. Wang, Q. Huang, and J. Xia. Two-mode contra-directional coupler based on superposed grating. *Opt. Express* 25, 2654-2665 (2017).

[107] D. T. H. Tan, K. Ikeda, and Y. Fainman. Coupled chirped vertical gratings for on-chip group velocity dispersion engineering. *Appl. Phys. Lett*. 95, 141109 (2009). https://doi.org/10.1063/1.3242028.

[108] K. Ikedaa, M. Nezhad, and Y. Fainman. Wavelength selective coupler with vertical gratings on silicon chip. *Appl. Phys. Lett*. 92, 201111 (2008). https://doi.org/10.1063/1.2936862.

[109] D. T. H. Tan, K. Ikeda, S. Zamek, A. Mizrahi, M. P. Nezhad, A. V. Krishnamoorthy, K. Raj, J. E. Cunningham, X. Zheng, I. Shubin, Y. Luo, and Y. Fainman. Wide bandwidth, low loss 1 by 4 wavelength division multiplexer on silicon for optical interconnects. *Opt. Expr*ess 19, 2401-2409 (2011).

[110] W. Shi, H. Yun, C. Lin, M. Greenberg, X. Wang, Y. Wang, S. T. Fard, J. Flueckiger, Nicolas A. F. Jaeger, and L. Chrostowski. Ultra-compact, flat-top demultiplexer using anti-reflection contra-directional couplers for CWDM networks on silicon. *Opt. Expre*ss 21, 6733-6738 (2013).

[111] B. Naghdi and L. R. Chen. Silicon photonic contradirectional couplers using subwavelength grating waveguides. *Opt. Express* 24, 23429-23438 (2016).

[112] Lodahl, P.; Mahmoodian, S.; Stobbe, S. Interfacing single photons and single quantum dots with photonic nanostructures. *Rev. Mod. Phys*. 87, 347−400. (2015).

[113] Hausmann, B. J. M. Shields, B. Quan, Q. Maletinsky, P.McCutcheon, M. Choy, J. T. Babinec, T. M. Kubanek, A. Yacoby, A. Lukin, M. D. Lončar. Integrated Diamond Networks for Quantum Nanophotonics. *Nano Lett.* 12, 1578−1582. (2012).

[114] H. Qiu, G. Jiang, T. Hu, H. Shao, P. Yu, J. Yang, and X. Jiang. FSR-free add–drop filter based on silicon grating-assisted contradirectional couplers. *Opt. Lett*. vol. 38, 1-3 (2013).

[115] W. S. Zaoui, A. Kunze, W. Vogel, M. Berroth, J. Butschke, F. Letzkus, and J. Burghartz. Bridging the gap between optical fibers and silicon photonic integrated circuits. *Opt. Express* vol.22, 1277-1286 (2014).